Experimental Investigations on the Influence of Curvature and Materials on Near-field Thermal Radiation

by

Poetro Lebdo Sambegoro

Submitted to the Department of Mechanical Engineering in partial
fulfillment of the requirements for the degree of

Doctor of Philosophy

at the

MASSACHUSETTS INSTITUTE OF TECHNOLOGY

February 2016

Signature redacted

Author...
Department of Mechanical Engineering
January 15, 2016

Signature redacted

Certified by..................... ....
Gang Chen
Carl Richard Soderberg Professor of Power Engineering
Thesis Supervisor

Signature redacted

Accepted by...................................
Rohan Abeyaratne
Chairman, Department Committee on Graduate Students

Experimental Investigations on the Influence of Curvature and Materials on Near-field Thermal Radiation

by

Poetro Lebdo Sambegoro

Submitted to the Department of Mechanical Engineering
on January 15, 2016, in partial fulfillment of the
requirements for the degree of
Doctor of Philosophy in Mechanical Engineering

Abstract

The bimaterial cantilever based near-field thermal radiation measurement setup was an experimental breakthrough in the field of near-field thermal radiation. The setup distinguishes itself from other experimental configurations at that time by allowing a direct measurement of the near-field thermal radiation without the need of fitting parameters. Part of this thesis was devoted to improve the measurement setup. The improved measurement setup is then further modified to experimentally investigate near-field thermal radiation between different geometries and materials.

To date, the challenges of alignment of two heat-exchanging bodies have limited the existing experimental investigation on near-field thermal radiation to plate-plate, sphere-plate, and tip-plate measurement. However, theoretical calculations predict more interesting phenomenon beyond these three configurations. This thesis presents a method to measure near-field thermal radiation between two microspheres. The procedure to align two microspheres presented in this thesis extends the existing experimental capability, which is limited to sphere-plate configuration. This method can be further used to investigate the effect of different curvatures of the surface, such as two spheres with different radii, and sphere-cylinder.

Recent progress on nanoscale radiative heat transfer has generated strong interest in controlling near-field thermal radiation. The ability to control near-field thermal radiation plays a significant role for applying this technology into applications such as radiative thermal diode, transistor, amplifier, and memory devices. Near-field thermal radiation can be tuned by changing carrier concentration. Using a doped silicon sphere, we demonstrate the tuning effect of near-field thermal radiation between doped silicon surfaces. This demonstration shows the potential application of near-field thermal radiation on controlling radiative transfer by modulating carrier concentration.

Thesis Supervisor: Gang Chen
Title: Carl Richard Soderberg Professor of Power Engineering

Dedication

To my family.

Acknowledgements

This thesis owes its completion to the support of numerous individuals. I would like to thank my advisor Professor Gang Chen for the opportunity to work with him, his guidance and supports. I also want to thank my committee members, Professor Nicholas Fang and Professor Marin Soljacic for providing helpful advice and a different prospective on the work.

Numerous individuals help me on this simple yet hard experiment. Professor Sheng Shen taught me to measure near-field thermal radiation for the first time. Professor Anastassios Mavrokefalos trained and worked with me during my early years. Jonathan Tong and Wei Chun-Hsu always gave helpful advice on the experimental setup. Photon subgroup (Professor Anastassios Mavrokefalos, Jonathan Tong, Dr. Matthew Branham, Dr. Brian Burg, Dr. Selcuk Yerci, Wei Chun-Hsu, Dr. Svetlana Boriskina and Yi Huang) always gave helpful advice through fruitful discussion every Tuesday. Dr. Alexander Gumennik and Prof. Yoel Fink provided the doped silicon spheres. Discussions over coffee or dinner with Daniel Kraemer were both helpful and enjoyable. I cannot thank him enough for giving me an example and being my role model of how a careful experimentalist should be. Nanoengineering Group have also been a great resource on helping me doing my research.

I want to thank Vazrik Chiloyan, Samuel Huberman, and Dr. James Loomis, who proof read this thesis. Mr. Edwars Jacobson, Mrs. Mai Hoang Ha, Mrs. Mary Ellen Sinkus, Mrs. Keke Xu, and Mrs Juliette Pickering helped me a lot on administrative matters. I also want to thank Leslie Regan in the Graduate office of the Department of Mechanical Engineering for her assistance in navigating the degree process.

I also would like to thank a number of people that made my time here great. Kenneth McEnaney, Kimberlee Collins, Daniel Kraemer, Maria Luckyanova, Matthew Branham and Jonathan Tong are great friends. I also want to thank the Indonesian community in greater Boston area for being my support system. I also want to thank my undergraduate advisor, Prof. Filino Harahap for being my friend, hero and role model.

I am grateful to the Fulbright Foundation and Roberto Rocca Foundation for support accorded to me via its fellowship program.

Finally, I want to thank my family, my mother, father, brothers, and sister in law for their constant support for the past seven years.

Contents

List of Figures

List of Tables

Chapter 1

Introduction

Thermal radiation describes heat transfer process caused by the electromagnetic waves. Common examples of thermal radiation include the heating effect when we stand under the sun or put our palm above the stove or stand facing the fire. Thermal radiation carries heat through the propagation of electromagnetic waves, which do not need any medium to propagate.

Thermal radiation originates from chaotic thermal oscillations of charges inside media. Thermal oscillations of electrons in metals or ions in crystals give rise to fluctuating current densities, which in turn generate electromagnetic waves or photons. Thus, every material experiences thermal radiation by continuously emitting and absorbing electromagnetic waves.

The amount of thermal radiation emitted by a blackbody can be calculated using Stefan-Boltzmann law [5],

$$E_b = \sigma T^4 \tag{1.1}$$

where E_b is the blackbody emissive power [W/m^2], T is absolute temperature [K], and σ is the Stefan-Boltzmann constant (5.67 x 10^{-8} W/m^{2}K^4). This is commonly referred to as blackbody limit. A blackbody is defined as a surface that absorbs all incident radiation, irrespective of wavelength or angle of incidence and nothing is reflected [6]. This law was first proposed by Joseph Stefan in 1879 after noticing that the radiated power of a medium is proportional to the fourth power of the absolute temperature. In 1884, Ludwig Boltzmann came up with the same expression after analyzing a Carnot cycle in which the pressure of the liquid is replaced by radiation pressure.

Although it was proposed earlier, Stefan-Boltzmann law can actually be derived by integrating Planck's law of thermal radiation over the whole electromagnetic waves spectrum. Planck's law of thermal radiation can be expressed as [7]–[9]

$$E_{b\lambda} = \frac{2hc^2}{\lambda^5\left[e^{\frac{hc}{k_B\lambda T}}-1\right]} \tag{1.2}$$

where h is the Planck constant (6.626 x 10^{-34} J s), c is the speed of light (2.997 x 10^8 m/s), l is the wavelength of the electromagnetic wave, k_B is the Boltzmann constant (1.38 x 10^{-23} J/K). Planck's law of thermal radiation describes the spectral energy density of electromagnetic waves, which is thermally excited and then emitted from a blackbody.

1.1 The origin of near-field thermal radiation

Although it is commonly understood and widely taught especially in undergraduate level heat transfer classes that blackbody radiation is the maximum limit of thermal radiation emitted by a surface, actually Planck himself warned the assumption that needs to be satisfied to derive the law that later bears his name. He wrote, "Throughout the following ... the linear dimensions of all parts of space considered, as well as radii of curvature of all surfaces ... are large compared with the wavelengths of the rays considered"[9]. So, blackbody limit is the maximum limit of thermal radiation emitted by a surface when all the characteristic dimension of the surface is large relative to the wavelength of the thermal radiation. In thermal radiation the characteristic wavelength corresponds to the dominant emission wavelength given by Wien's displacement law [5].

According to the relative length between the wavelength of the electromagnetic wave and the characteristic dimension, the electromagnetic regime can be divided into far or near-field regime. Far-field refers to the condition when the characteristic wavelength is much smaller than the separation distance between objects. In the far-field regime evanescent waves do not contribute to the energy transfer because the evancescent field decays rapidly and become negligible when it reaches another object. Near-field effects are considered only at a distance comparable or smaller than the characteristic wavelength. In this regime, evanescent waves are the reason why thermal radiation is larger than that in the large gap.

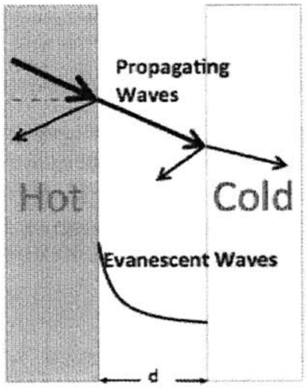

Figure 1.1 Two types of thermally excited electromagnetic waves: propagating waves and evanescent waves. Propagating wave is transmitted through the interface and propagates freely into free space from the surface of a medium. Evanescent wave is bound to the surface of the medium and its field decays exponentially from the surface.

When the distance between two bodies is far relative to the thermal wavelength, the heat is carried through the propagation of electromagnetic waves in free space. When the distance between two surfaces is small another channel to transfer heat exists via evanescent waves. The evanescent field decays exponentially normal to the surface, as depicted in figure 1.1. The evanescent waves do not contribute to the heat transfer when the distance between two bodies is relatively far because the fields decay rapidly and become negligible by the time it reach the other body.

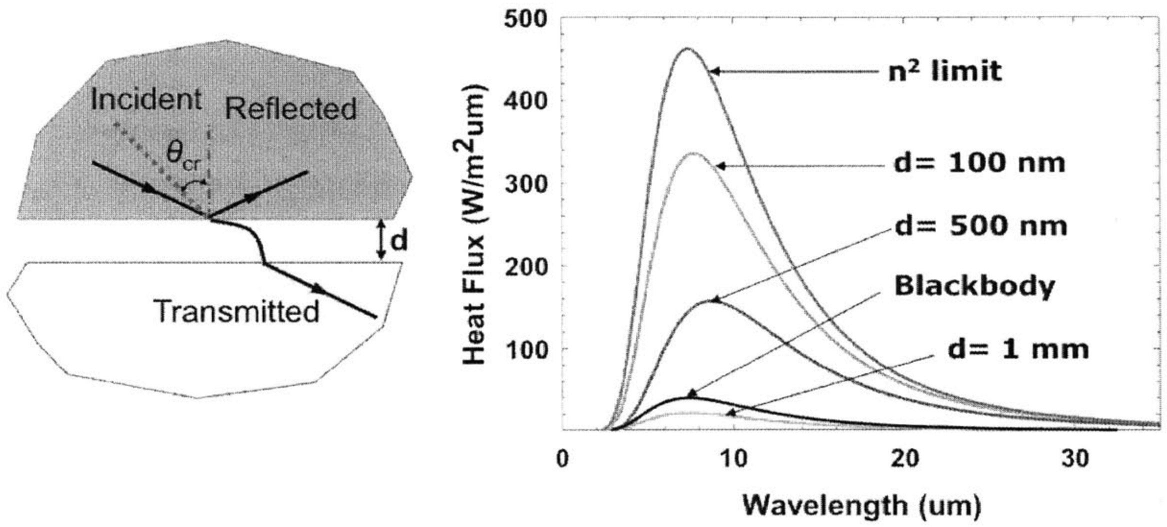

(a) (b)

Figure 1.2 a. Propagating wave inside the optically denser medium hits the interface with an angle larger than the critical angle causing total internal reflection. b. The spectral radiative heat flux between two parallel plates for different gaps *d*. The evanescent waves contribution becomes dominant to the heat transfer as the gap becomes smaller. The heat flux asymptotically approach n^2 limit as the gap disappears. The theoretical background is presented in Chapter 2.

The origin of the evanescent waves can be differentiated into two physical phenomena: total internal reflection of the propagating wave inside a medium or the existence of surface polariton waves. Total internal reflection is a physical condition where the propagating wave inside the optically denser medium hits the interface with an angle larger than the critical angle as depicted in figure 1.2a. Although there is no transmitted wave propagates into vacuum, the evanescent wave exists on the interface. Figure 1.2b presents the spectral radiative heat flux between two parallel plates for different gaps *d*. The evanescent waves contribution due to total internal reflection overwhelms the propagating waves contribution as the separation gap becomes smaller and asymptotically approaches n^2 limit as the gap disappears, where n is the index of refraction.

Surface polariton is a coupled mode between carriers, such as electrons, phonons or magnons, and the electromagnetic waves which propagates along the interface of two mediums [10]. Surface polariton is confined on the interface while its field decays exponentially to both mediums normal to the interface as depicted in figure 1.3a. Surface polaritons are resonant modes with high density of states. Orders of magnitude thermal energy transfer enhancement is achieved when the frequency of surface polaritons coincides with the peak of the Planck's oscillator. Figure 1.3b presents the spectral radiative heat flux between two parallel plates of a polar dielectric material (glass) for different gaps *d*. Surface phonon polaritons peaks are observed at 8.5 μm and 20.3 μm and show 4 orders of magnitude enhancement relative to the blackbody.

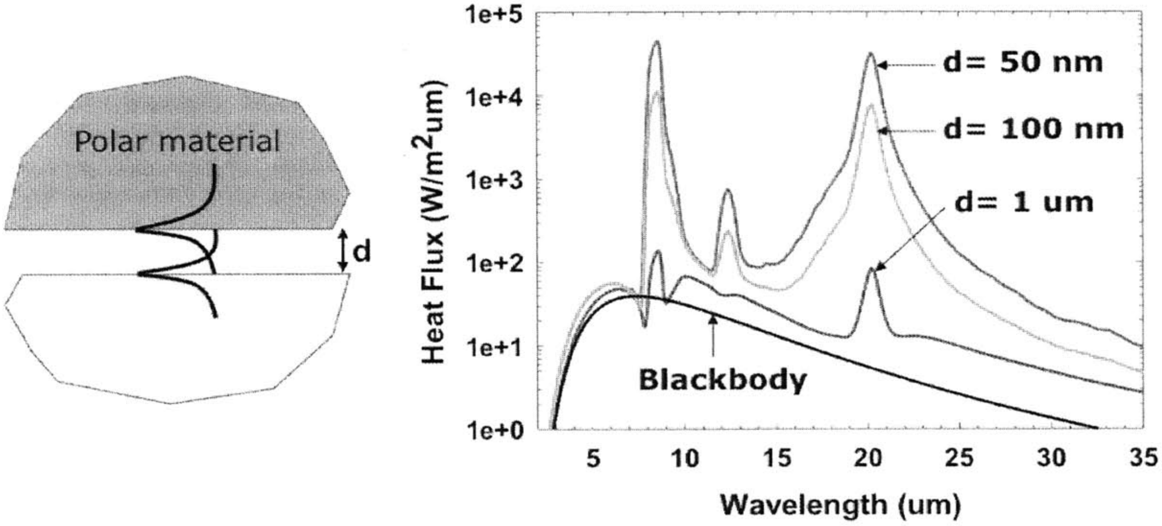

(a) (b)

Figure 1.3 a. The evanescent field of surface polaritons decays to both directions normal to the interface between a polar dielectric material (glass) and vacuum. b. The spectral radiative heat flux between two glass plates at room temperature for different gaps *d*. Surface phonon polaritons peaks are observed at 8.5 μm and 20.3 μm.

Figure 1.4 compares the total radiative heat transfer contribution between the propagating waves and the evanescent waves as function of separation between two parallel glass substrates.

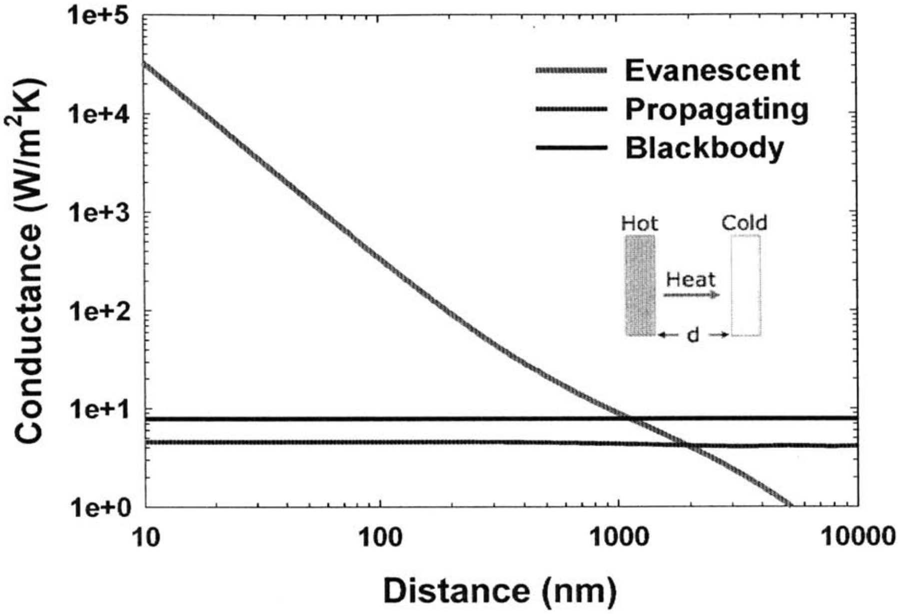

Figure 1.4 The evanescent waves contribution (red) is orders of magnitude larger than the blackbody limit (black) when the distance between two bodies is smaller than the characteristic thermal wavelength.

1.2 Research progress on near-field thermal radiation

1.2.1 Theoretical investigations

In 1967, Cravalho *et al.* [11] were the first to analyze the role of the wave interference and tunneling effect of the evanescent wave on the thermal radiation. They analyzed the role of the wave interference and tunneling of the evanescent wave between two parallel dielectric plates. Their calculation result predicted an order of magnitude enhancement of radiative transfer when the gap reduced to sub wavelength gap. A year later, Olivei [12] published a similar work on the effect of the wave interference and tunneling of the evanescent wave on thermal radiation between two parallel dielectric plates at cryogenic temperature. In 1970, Boehm and Tien [13] analyzed the same effect between two parallel metal plates. Their results predicted orders of magnitude enhancement of radiative transfer. Although these first theoretical works started the studies of near-field thermal radiation, it was Polder and van Hove [14] who developed a general formalism to calculate near-field thermal radiation in 1971. Their work, based on Rytov's fluctuational electrodynamics [15], [16] to calculate radiative heat transfer, is considered as the corner stone of the theoretical analysis of the field of near-field thermal radiation. Polder and van Hove's work was followed by Loomis and Maris [17] who worked on the same problem but focusing on the evanescent wave contribution to heat transfer. More theoretical works were published between 1970-1990 [18]–[21]. As previous works, these works only considered the influence of evanescent waves resulting from total internal reflection.

Although it is understood now that the contribution of the evanescent waves from surface waves is orders of magnitude larger, it was Shchegrov *et al.* [22] who pointed out the monochromatic nature of thermal emission of surface waves in the near-field regime. Surface waves have large density of energy resulting on orders of magnitude enhancement of radiative transfer. Further, Carminati and Greffet [23] showed that the surface waves significantly change the spatial correlation of the emitted field. Later, they also demonstrated that surface waves can be converted into highly directional propagating waves using a grating [24].

The effect of the optical properties of the materials on near-field thermal radiation has been investigated theoretically and experimentally. Metallic surface shows enhanced near-field radiative transfer due to the surface plasmon polaritons [10]. However, surface plamon polaritons on metallic surfaces can only be excited at extremely high temperature since plasma frequency of metals typically lies in the UV-visible spectrum, impractical for technological use. On the contrary, plasma frequency of semiconductors lies in the infrared spectrum hence surface plasmon polaritons on semiconductor surface can be thermally excited at room temperature. Further, since the plasma frequency can be control by changing the carrier concentration, surface plasmon polaritons on semiconductor surface can be tuned, hence controlling near-field thermal radiation[25], [26]. Surface phonon polaritons on polar dielectric surfaces have also been shown to dramatically increase near-field radiative transfer [16]. The near-field thermal radiative transfer in advanced materials such as graphene [27], [28], and hyperbolic metamaterials [29] have also been investigated. Ilic et al. and Svetovoy et al. independently showed that near-field thermal radiation in graphene could be tuned by changing the chemical potential and the relaxation time. This can be practically done by doping or gating. This opens a possibility of an externally controllable thermal radiative switch. Hyperbolic metamaterials have also been found to broaden the spectrum of the near-field radiative transfer [30]. Biehs et al. [29] shows that hyperbolic structure can turn poor near-field emitter into a good one. Compared to monochromatic nature of surface waves, this opens possibilities to increase near-field heat transfer over broad spectrum for variety of applications. Phase change material Vanadium Dioxide (VO_2) has also been shown to have potential applications in thermal management. The optical property of VO_2 changes dramatically at room temperature. It opens possibility to tune the near-field thermal radiation by changing the temperature of the surface [31].

The geometries of the closely spaced objects, which in the end are dictated by the device and its application, also affect the near-field thermal radiation. Near-field thermal radiation between thin films had also been studied as an extension of the two parallel plates case [32]–[36]. The effects of different geometries beyond two parallel plates have been theoretically investigated, although with less intensity, due to the complexity of the numerical calculation. These geometries include a sphere and a semi-infinite body [37], [38], two spheres [39], and more complicated geometries [40]–[44]. Narayanaswamy and Chen [39] were the first to analyze near-field thermal radiation between two spheres. Numerical calculation was performed to solve this problem. This work is marked as the first attempt to analyze near-field thermal radiation beyond dipole approximation [45] or proximity approximation [46]. Krueger et al. [37] and Otey and Fan [38] extend the theoretical work on a sphere-plate problem, which is of direct experimental relevant. Their results confirm the validity of proximity or Derjaguin approximation to calculate near-field thermal radiation between a sphere and a plate when the gap is much smaller than the radius of the sphere. McCauley et al. [42] developed a general numerical method to calculate near-field thermal radiation between a plate and objects with arbitrary shapes. They compare three different cases: sphere-plate, cylinder-plate, and cone-plate. Their results may have important implications for near-field thermal writing and surface roughness. Rodriguez et al. [41] proposed a more sophisticated formulation based on a fluctuating-surface-current. This method is able to calculate near-field thermal radiation between complicated geometries such as two interlocked rings. Combining fluctuating surface-current and finite difference time domain formulation, Rodriguez et al. [43] analyzed near-field thermal radiation between a cylinder and a perforated surface. The near-field thermal radiation shows a nonmonotonic behavior as a function of separation. They attributed this behavior not only to geometry and temperature but also to optical property of the material. Near-field thermal radiation between photonic crystals have also been analyzed. Rodriguez et al. [40] used FDTD to analyze near-field thermal radiation between photonic crystals. They showed that frequency-selective near-field thermal radiation can be increased at particular frequencies and separations. Hirashima and Hanamura [44] analyze near-field thermal radiation between pillar array structure surfaces made of nickel. Near-field thermal radiation is enhanced through interference of surface plasmon polaritons. This effect shows that the spectral near-field thermal radiation can be tuned by designing the dimension of the pillar structure.

The ability to enhance radiative energy transfer by evanescent waves had raised the question of the radiative energy transfer limit. Pendry [47] proposed a maximum heat transfer limit to a single mode. The results, which are linked to quantum information theory, show that the maximum heat tunneling current in any single mode is determined by the temperature alone. Materials with finite conductivity are proposed to maximize the near-field radiative transfer. On the contrary, it has been calculated that conductors do not result in significant enhancement in near-field radiative transfer. Basu *et al.* [48] investigated the maximum achievable radiative heat flux between two parallel plates by assuming a frequency independent dielectric function with all frequencies supporting surface waves and introducing a cutoff value on the parallel wavevector component. This cutoff value corresponds to the lattice constant of the crystal. Wang *et al.* [49] studied the influence of all parameters in the Drude and the Lorentz models to maximize the near-field radiative heat flux. Ben-Abdallah *et al.* [50] investigated the limit of energy transfer between two arbitrarily flat media separated by a vacuum gap. They used a general variational approach to derive an upper limit for the energy transfer.

Since the calculation of near-field thermal radiation is based on the concept of a local dielectric constant, the predicted radiative heat transfer had been shown to diverge, as the separation gap becomes zero. This divergence has been criticized by Pan [51]. To solve the problem, spatial dispersion of the dielectric constant needs to be included in the calculation. Volokitin and Persson [52], [53] were the first to include the spatial dependence of the dielectric constant in the radiative heat transfer calculation. Later, Chapuis *et al.* [54] and Joulain *et al.* [55] showed that the radiative heat transfer will eventually saturate when the separation distance goes to zero by including the spatial dispersion of the dielectric constant. To investigate near-field thermal radiation at around contact regime, Chiloyan et al. [56] developed an atomistic framework based on microscopic Maxwell's equations and lattice dynamics and compared it with the fluctuating electrodynamics approach. The two approaches are found to be in excellent agreement for separation distance larger than 1 nm. At sub-nanometer gaps the two approaches differ significantly as the acoustic phonon tunneling dominates in this regime. This work showed that continuum approach based on local dielectric constant is valid down the nanometer regime.

1.2.2 Experimental investigations

The challenges of alignment of two heat exchanging bodies has limited the existing experimental setup to plate-plate [57]–[61], sphere-plate [2], [3], [62]–[66], and tip-plate measurement [67]–[69].

1.2.2.1 Plate-plate

Experimental studies on near-field radiation commenced in the late 1960's by Tien and co-workers. Domoto *et al.* [58] reported the first experimental work on near-field radiation. They measured radiative heat transfer between two parallel copper disks with separation gaps ranging from 2 mm to 10 mm at cryogenic temperatures (~10 K). The temperature of the emitter was maintained at 10 K and 15.1 K, while the receiver was maintained at approximately 4.5 K. In this temperature range, near-field effects can be observed at large separation gaps (~100 um). Large separation gaps significantly reduce the difficulty of aligning two parallel plates. In this first effort, even though the near-field mediated heat transfer measured was greater than that of the far field, the measured heat flux only made up 3% of the total energy transfer between ideal blackbodies. Kutaladze et al. [70] reported a similar measurement with copper disks. The separation between the disks was reduced from 250 um to 10 um. The results shows significant enhancement on near-field thermal radiation. Another early experimental work on near-field thermal radiation was carried out by Hargreaves [57], [71]. He measured the radiative heat transfer between two optically flat surfaces coated with 1000 Å thick Chromium. The temperatures of the plates were maintained at 323 K and 306 K for the emitter and cold side, respectively. This was first near-field thermal radiation measurement carried out at room temperature. In this temperature range near-field effect can be observed as of ~10 μm. He pushed the separation gap down to as low as 1.5 μm and was able to maintain both plates parallel at such small separation gaps by measuring the capacitance and the interference pattern on the chromium surfaces. At a 1.5 μm vacuum gap, the near-field heat transfer at room temperature was 5 times greater compared to that in the far field. However, the measured heat flux was still only 40% of that between two blackbodies.

After the early experimental investigation in 1970s, Hu *et al.* [29] revived two parallel plates setup to measure the radiative heat flux between two parallel glass substrates in 2008. The separation was maintained by using small polystyrene spheres. The separation is limited to 1 μm due to the diameter of the spheres. Other disadvantages of this experiment are the difficulties of aligning two parallel plates and ensuring that both surfaces do not make any physical contact. These results clearly showed that the radiative heat flux exceeds Plank's law of blackbody radiation and were the first to do so. The primary contribution to the heat transfer is attributed to surface phonon polaritons.

Ottens et al. [60] reported near-field thermal radiation measurement between two large sapphire plates (50 x 50 mm^2). The measurement setup controls the gap and parallelism by measuring the capacitance of a pair of copper plates on each corner of the sapphire plates. Measurements were carried out for temperature differences ranging from 6.8 to 19 K as the gap is varied from 2 to 100 um. The measurement results were found to be slightly higher than the theoretical calculation. This was attributed to the flatness of the sapphire plates. Kralik et al. [61], [72] reported near-field thermal radiation measurement between two parallel tungsten plates with a 35 mm diameter at cryogenic temperature. The emitter temperature is varied from 10 to 40 K, while the receiver temperature is maintained at 5 K. The measurement results shows two orders of magnitude enhancement of near-field thermal radiation relative to the blackbody radiation.

St-Gelais et al. [73] reported a demonstration of a microstructure platform for near-field thermal radiation application. The platform consist of two 200 um long parallel beams with 500 nm x 1.1 um cross section made of silicon nitride with silicon dioxide coating as an emitter and a receiver materials. The silicon dioxide is used since it has high near-field thermal radiation conductance due to surface phonon polaritons at room temperature. The silicon nitride is used since it has high tensile strength to support the long structure. Platinum is used both as resistive heaters and thermometers to measure the heat flux. The separation distance between the nanobeams is tuned using electrostatic force. The platform is reported to allow 500 nm gap variations with ±10 nm accuracy. The measurement results shows heat transfer enhancement as the separation gap between the beams is reduced from 750 nm to 250 nm.

1.2.2.2 Tip-Plate

Xu *et al.* [59], [74] reported a near-field thermal radiation measurement between a squeezed indium needle and a flat gold surface of a planar thermocouple. The temperature difference between the needle and the thermocouple was in the range of 40 K, while the thermocouple junction was maintained at room temperature. While the gap was made smaller than 100 nm, the results remained inconclusive, mainly due to the sensitivity of the experimental setup. Xu's work was followed by Muller-Hirsch et al. [75] who reported near-field heat transfer experiment between a tip and a plate with two different experimental setups. The first experimental setup measured near-field heat transfer between a tungsten tip and a planar Au/Ni thermocouple. The second experiment measured near-field heat transfer between a Au/Ni thermocouple tip and a 100 nm gold film on a mica substrate. Both setups was integrated in a commercial UHV-STM. The near-field heat transfer is detected as the change of the temperature measurement as the tip-plate separation gap is varied. Although they were not able to determine the absolute value of the heat transfer between the tip and the plate due to the experimental setups, strong heat transfer-distance dependence was clearly observed as the tip was retracted from contact to 10 nm. The thermocouple tip was then used to thermally scan the surface of the sample, showing a 10 nm resolution thermal micrograph.

In 2005 Kittel *et al.* [67] used similar experimental setup to measure the heat transfer between the tip of a scanning thermal microscope and a gold (Au) or gallium nitride (GaN) surface at separation gaps between 100 nm and 1 nm. The temperature of the sample was lowered down to 100 K, while the tip was maintained at room temperature, establishing a 200 K temperature difference between the tip and the sample. Their results clearly showed heat transfer enhancement at small gaps and agreed well with predicted values for separation gaps larger than 10 nm. For separation gaps less than 10 nm the measured heat transfer saturated which differed from the divergent behavior seen in the predicted results. The authors speculated that the observed saturation was due to the spatial dependence of the dielectric constant. By replacing a flat plate with a STM tip, which is assumed to behave like a point-like dipole, the problem of parallelism between two plates is eliminated. Other concerns such as the cleanliness of the surface and the surface roughness are also minimized because of the small surface area of the tip. However, several drawbacks should be noted. The geometry of the tip is difficult to model thus any comparisons between theoretical and experimental results inherently include more uncertainty. The magnitude of the near-field radiative transfer is also much smaller due to the small surface area of the tip. This makes the measurement more challenging, as the sensitivity of the experiment was not sufficient. The far-field radiative transfer between the tip holder, which has a large surface area, and the sample most likely interfered with the near-field radiation between the tip and the sample. Despite all these disadvantages, this is the only near-field thermal radiation measurement, which observed a saturation of the heat transfer when the separation gap became very small. This again is suspected to occur because of the spatial dispersion of the dielectric constant.

Guha et al. [76] reported a near-field thermal radiation measurement between a silica coated tungsten tip and a 840 nm thick silica membrane. The heat transfer is measured by measuring the temperature change of the silica membrane using Ni resistive thermometer, which also acts as a heater. A clear near-field signal was observed as the separation gap between the tip and the membrane was reduced from 3.5 um to 350 nm.

1.2.2.3 Sphere-Plate

In 2008, Narayanaswamy *et al.* [62], [77] developed a revolutionary technique to measure near-field thermal radiation between a microsphere and a flat surface using a bi-material cantilever. This technique elegantly solves the parallelism issues found in two parallel plates case, while at the same time keeping the magnitude of the heat transfer large enough to be clearly observed. Using the this experimental setup, Shen *et al.* [2] demonstrated that the near-field radiative heat transfer between polar dielectric materials exceeds Planck's blackbody radiation by orders of magnitude due to the existence of surface phonon polaritons.

Rosseau *et al.* [63] measured the radiative transfer between a glass microsphere and a glass substrate using a similar experimental setup developed by Narayanaswmay [62] with two modifications. The first modification is to heat the substrate instead of the cantilever. The other modification is to use a fiber interferometer technique to measure the cantilever deflection. These modifications actually caused more problems rather than improving the experiment. The heated substrate will transfer heat not only to the sphere, but also to the cantilever. The deflection of the cantilever is then not only due to near-field effects between the sphere and the substrate but also due to far-field radiative transfer between the substrate and the cantilever. By placing a fiber near the cantilever to measure its deflection, radiative transfer between the cantilever and the fiber is also very likely to occur. Instead of isolating the measurement between the substrate and the sphere, the placement of the fiber near the cantilever complicates the measurement by introducing a third emitting body. Another drawback is the introduction of a calibration factor, which depends on an unreliable assumption of the emissivity of the silica sphere. They also included the far-field contribution through calculation. This calculation does not seem accurate since they only include the radiative exchange between the sphere and the substrate while in reality the size of the sphere is much smaller compared to the cantilever. Despite all these disadvantages, they report the radiative transfer measurement, including far-field contribution, for separation distances between 30 nm and 2.5 mm. Their results fit the theoretical calculation based on the Proximity Force Approximation very well. However, since the experimental results depend on the proportionality factor that they introduced based on an unreliable analysis, the agreement between the experimental data and the theoretical calculation is questionable.

Shen et al. [64] measured near-field thermal radiation between gold-coated silica sphere and substrate. Near-field thermal radiation was observed despite the absence of surface polaritons resonance on the gold surface at room temperature. Zwol et al. [78] measure near-field thermal radiation between a 40 um diameter sodalime glass sphere and vanadium dioxide layer. Their bimaterial cantilever based experimental setup follows an earlier publication by Rousseau et al. [63]. They experimentally demonstrate that the near-field thermal radiation is enhanced by the change in surface phonon polaritons states during the metal-insulator transition. Zwol et al. [79] also measure near-field thermal radiation between a silica sphere and a graphene layer, which is epitaxially grown on SiC substrate. The near-field heat flux from graphene layer is observed to contribute dominantly at small gaps. Shi et al. [65] demonstrated the tunability of the near-field thermal radiation between a silica sphere and silicon substrates with different doping level. Song et al.[4] measured near-field thermal radiation between a silica sphere and thin silica films. The experimental setup consists of a suspended silicon heater onto which a 53 um diameter silica sphere was attached and suspended a SiN_x receiver onto which thin silica film with varying thickness (50 nm-3 um) was deposited on a 100 nm thick gold film. Platinum resistance heater-thermometers were integrated onto both emitter and receiver to measure the temperature change [80]–[82]. This setup completely decouples the heat transfer and force signal, which is a problem in the cantilever based experimental setup [62]. The measured near-field conductance showed strong film thickness dependence as the near-field conductance decreases as the thickness decreases. This occurred because the short wavevector surface phonon polaritons mode cannot be excited in such thin films.

1.2.2.4 Spectral investigation

Spectral information of near-field thermal radiation had also been investigated experimentally. Jones et al. [83], [84] combined scanning near-field optical microscope and FTIR to spectroscopically characterize near-field thermal radiation in the mid-infrared spectrum. Spectral near-field thermal radiation from SiC, Si02, and PTFE surfaces were measured using a heated silicon AFM tip which served as both a local heater and scattering probe. The scattered evanescent field is collected and analyzed with FTIR spectrometer. Resonance peaks due to surface phonon polaritons were observed for respective samples.

Babuty et al. [85] combined FTIR and Thermal Radiation Scanning Tunneling Microscope (TRSTM) [86] to study the local spectra of the near-field thermal radiation from silicon carbide and silica surfaces. Resonant peaks were observed at 913 cm^{-1} and 1110 cm^{-1} for silicon carbide and silica repectively. Zhang et al. [87] investigated the spectral near-field radiation of thin amorphous silica film on a silicon substrate. Strong dependence of surface phonon polaritons resonance on the thickness of the film was observed. Qazilbash et al. [88] investigated the insulator-to-metal transition (IMT) of Vanadium Dioxide (VO_2) films using a scanning near-field infrared microscope. They observed the percolative phase transition with increasing or decreasing temperature across the IMT.

1.2.3 Technological relevance

1.2.3.1 Near-field thermo photovoltaic

The ability to increase energy transfer through the tunneling of evanescent field when the distance between objects is relatively small creates possibilities of potential applications. The use of the evanescent waves tunneling to increase the performance of thermophotovoltaic has been theoretically studied [51], [89]–[91]. DiMatteo et al. [92] experimentally demonstrated the near-field thermophotovoltaic by placing a Silicon emitter on an InAs PV cell separated by silica spacers. Whale et al. [93]. Narayanaswamy et al. [94] proposed to use surface phonon polaritons to improve the power density and efficiency of low temperature TPV. Laroche et al. [91] presented a quantitative model of a near-field thermophotovoltaic. They observed an increase of power output by a factor of 20 and 35 for tungsten and quasimonochromatic emitter respectively comparing with a blackbody source in the far field. The efficiency is also increased from 21% and 10% in the far field to 27% and 35% in the near-field for tungsten and quasimonochromatic emitter respectively. Park et al. [95] theoretically study the mechanisms of a near-field TPV by calculating the absorbed energy distribution and photocurrent generation inside the PV cell. They suggest an emitter-cell distance to maximize the efficiency.

Francoeur [96] studied the thermal influence on the performance of near-field TPV. The calculation combined near-field thermal radiation, charge transport, and heat transfer model of the near-field TPV system. Messina et al. [97] proposed a graphene covered PV cell. The calculation result shows that the graphene layer modifies the optical response of the cell, resulting in new surface resonant modes which produce a significant enhancement of the power output and efficiency of the TPV system. Similar approach was followed by Svetovoy et al. [98] to use graphene-on-silicon Schottky PV cell. Near-field thermal radiation has also been used to improve the thermal emitter for near-field thermophotovoltaics application. Zhao et al. [99] proposed a 2D tungsten grating/thin film nano structure emitter to enhance its performance. Guo et al. [100] proposed high temperature plasmonic metamaterials as narrowband tunable thermal sources for TPV application.

1.2.3.2 Control of near-field thermal radiative heat transfer

Researchers have also proposed mechanisms to control near-field thermal radiation. Although, the simplest mechanism to modulate the near-field thermal radiation is by varying the separation distance, studies have shown that there are other modulation mechanisms can be done. One way to modulate near-field thermal radiation is by changing the orientation angle betweent two heat exchanging bodies. Biehs et al. [101] proposed to modulate near-field thermal radiation between Au/SiC gratings by changing the orientation angle. This mechanism is shown to modulate the near-field thermal radiation up to 90%. Rodriguez et al. [41], [102] showed that the near-field thermal radiation between 2 gold cylinders can be modulated by a factor of 3 depending on the orientation angle. Nikbakht [103] showed that the near-field thermal radiation between anisotropic particles in many body systems can be tuned by changing their relative orientation. Another way to modulate near-field thermal radiation is by using phase change materials. Zwol proposed to use Vanadium Dioxide [31] and an alloy of silver, indium, antimony, and tellurium (AIST) [104] to modulate the near-field thermal radiation. The phase of VO2 can be change by varying the temperature (MIT of VO2 happens at 340 K), while AIST's phase can be change by applying electric field. Huang et al. [105]

proposed to use ferroelectric materials to control near-field thermal radiation. Near-field thermal radiation is shown to change as much as 16.5 % by varying external electric field at cryogenic temperature.

Different mechanisms to modulate the near-field thermal radiation have opened possibilities to control thermal radiative transfer. Devices such as thermal diode, transistor, amplifier, and memory have been proposed. Otey et al. [106] proposed to use 3C-SiC and 6H-SiC to achieve near-field thermal radiation rectification. The maximum rectification (R = 0.41) was found when the hot side is 600 K and the cold side is 300 K, while the separation gap is below 100 nm. Basu et al. [107] propose a near-field thermal radiation rectifier using a film and a bulk of doped silicon. Rectification of 0.5 is achieved by varying the dopant concentration. Iizuka et al. [108] proposed to cover SiC with dielectric layer to achieve rectification. Huang et al. [109] proposed to use VO2 and LCSMO to achieve rectification. Zhu et al. [110] proposed to use two different sizes of nanospheres to achieve thermal rectification with very high contrast (>10) and large operating bandwidth.

Using three body configuration, Messina et al. [111] proposed a passive near-field thermal amplifier. The device is made of two SiC slabs of thickness 5 um. It was shown that the near-field thermal radiation increases when a metallic film is inserted between the SiC plates. Using the same configuration, Ben-Abdallah et al. [112] proposed a near-field thermal transistor using VO2 as the gate material. The near-field thermal radiation between the source and the drain, which are made of silica, can be reversibly switched, amplified, and modulated by changing the gate temperature around its critical value, hence, matching the near-field coupling between the source and the gate, and the gate and the drain.

Kubitskyi et al. [113] proposed thermal memory based on metal-insulator transition of VO2. The proposed thermal memory can be used to store heat and thermal information via an encoding temperature. The design consists if a silica and VO2 films coupled to thermal baths. Near-field thermal radiation drastically increases the heat transfer between both membranes and the speed of natural cooling or heating. Elzouka et al. [114] proposed the concept of NanoThermoMechanical memory, a memory device that uses heat to record, store, and recover data. This concept combines near-field thermal radiation and thermal expansion resulting in a bistable thermal system with two stable states at two different temperatures. Challener et al. [115] demonstrated a heat-assisted magnetic recording device which exploits near-field effect to heat magnetic recording medium to reduce its coercivity in a confined area. Laser light is coupled on to a gold near-field transducer to excite surface plasmons resonance. The evanescent field is confined to a tight area, hence increasing the resolution of the recorded data.

1.2.3.3 Near-field thermal microscope

In 1986, Williams and Wickramasinghe [116] demonstrated a 100 nm resolution near-field thermal microscope. The probe consists of a thermocouple sensor. They demonstrated a noncontact profiling of resist and metal films with a 100 nm lateral resolution and 3 nm depth resolution. Although limited to electrically conductive material, near-field thermal radiation measurement technique between a tip and a plate [75] had demonstrated the potential of nanoscale thermal microscopy especially at nanoscale gaps. Kittel et al. [117] demonstrated a near-field scanning thermal microscope (NSThM), that provides thermal images of nanoscale structure surface using the refined version of the experimental setup [67], [75], [118]. Using the same setup Worbes et al. [69] thermally scanned a single ionic monolayer island of sodium chloride (NaCl) deposited on a gold surface. They found that the monolayer increases the near-field thermal radiation by a factor of 2 at few nanometers tip-sample separation gap.

Another type of near-field thermal scanning microscope was proposed by De Wilde et al. [86], [119]. The device consists of an AFM with a hot sample holder combined with an infrared optical microscope and a HgCdTe detector. The AFM uses a tungsten tip to scatter the evanescent fields on the sample surface into the far field. The scattered waves is collected by a Cassegrain objective, and focused on a HgCdTe detector. The measurement was demonstrated using silicon carbide samples with gold patterns showing micrometer spatial resolution. Jones et al. [83] demonstrated a similar idea by combining a heated AFM tip and FTIR spectroscopy.

The measurement was demonstrated using a PTFE flake on a silicon substrate with 50 nm spatial resolutions.

1.3 Motivation

The main difficulty to measure near-field thermal radiation is to maintain and measure submicron separation gap between two surfaces. Since clean surfaces are one of the most important factors in this measurement, surface contamination results in several experimental complications:

1. Surface contamination covers the surface, changes the interface condition, and may prevent the excitation of the evanescent waves.
2. Surface contamination such as particulates may create contact between two surfaces and create heat conduction channel between two bodies.
3. Surface contamination such as particulates prevents nanoscale gap measurement, since the smallest separation gap will be determined by the size of the particulates.
4. Surface contamination such as particulates introduces uncertainty on the separation gap measurement, since the separation gap is usually measured from contact point.

To minimize surface contamination, the measurement area is minimized. This strategy also makes the measurement of separation distance between two small surfaces easier. However, minimizing the area comes with another challenge. Since heat transfer is proportional to the area, small area means small heat transfer, hence small measurement signal.

In the previous section, numbers of experimental setup utilizing extremely sensitive power and temperature sensors have been reviewed. But despite recent increase in numbers of report on the experimental investigation of near-field thermal radiation, due to the challenging nature of this measurement, critical questions should always be raised on the accuracy of the reported measurement results. A fitting factor is often used to match the measurement result with the theoretical calculation, which raise question on the accuracy of the measurement results itself [63], [73]. The geometry of the heat exchanging bodies also introduces another complication, which prevents direct comparison between the measurement results and the theoretical predictions [67], [73], [76].

The near-field thermal radiation experimental setup in the Nanoengineering Group/Rohsenow Kendall Heat Transfer Laboratory at MIT was first set up by Narayanaswamy [62]. This bimaterial cantilever based approach (detail in Chapter 2) was an experimental breakthrough in the field of near-field thermal radiation. The setup distinguishes itself from other experimental setup at that time by allowing a direct measurement of the near-field thermal radiation without the need of fitting process. Part of this thesis was devoted to improve the measurement setup. The improved measurement setup is then further used to experimentally investigate near-field thermal radiation between different geometries and materials.

As mentioned above, the challenges of alignment of two heat exchanging bodies has limited the existing experimental setup to plate-plate [57]–[61], sphere-plate [2], [3], [62]–[66], and tip-plate measurement [67]–[69]. However, to enable real applications, the design of the devices should not be limited to these three configurations. This thesis presents the measurement of near-field thermal radiation between two spheres, hence, extends the existing experimentally capability which is limited to plate-plate, sphere-plate, and a tip-plate configuration.

Almost all of the experimental investigations on the near-field thermal radiation between a sphere and a plate use a silica sphere as an emitter because silica microspheres are available commercially. Although, many interesting near-field phenomenon exist in other materials such as silicon. Plasma frequency of doped silicon lies in the infrared spectrum hence surface plasmon polaritons on semiconductor surface can be thermally excited at room temperature. Further, since the plasma frequency can be controlled by changing the carrier concentration by electrical field, temperature, or light, surface plasmon polaritons on semiconductor surface can in theory be tuned, hence controlling near-field thermal radiation[25], [26]. This thesis experimentally investigates near-field thermal radiation between doped silicon.

1.4 Thesis Outline

This thesis starts with improvement of the previous near-field thermal radiation experimental setup. The improved measurement setup is then used to experimentally investigate near-field thermal radiation between different geometries and materials. Chapter 2 introduces the theoretical background on near-field thermal radiation. In chapter 3, improvements on experimental setup are presented. In chapter 4, the experimental setup is used to measure near-field thermal radiation between two silica spheres, extending the existing experimentally capability which is limited to plate-plate, sphere-plate, and a tip-plate configuration. In chapter 5, the near-field thermal radiation measurement between doped silicon is presented. Chapter 6 summarizes the finding presented in the thesis, and suggests a path for future work on the measurement of near-field thermal radiation.

Chapter 2

Theoretical Background

This chapter presents theoretical calculation and analysis of near-field thermal radiative transfer. The theoretical foundation to calculate and analyze near-field thermal radiative heat transfer is presented. Glass is used as an example material due to its experimental relevance.

2.1 Theoretical Calculation of Near-Field Radiative Heat Transfer between Two Parallel Plates

Near-field thermal radiation between two semi-infinite plates is calculated based on fluctuational electrodynamics [15], [16]. Fluctuational electrodynamics is based on the macroscopic idea that thermal radiation originates from random thermal fluctuations of volume charge densities, not from the sum of the individual charges. These fluctuations generate electromagnetic waves which then carry the energy. Theoretical derivations to calculate thermal radiation can be divided into two parts. First, the fluctuation-dissipation theorem is used to relate the fluctuating current densities to the local temperature of the emitting media. Second, Maxwell's equations are solved to calculate the electromagnetic waves resulting from the fluctuation current densities.

Figure 2.1 shows two parallel plates separated by a vacuum gap with a distance *d*. Each plate is assumed to (1) be semi-infinite, (2) have infinite optical thickness, (3) be at thermal equilibrium, (4) be non magnetic and isotropic, and (5) be perfectly smooth and that the plates are parallel to each other.

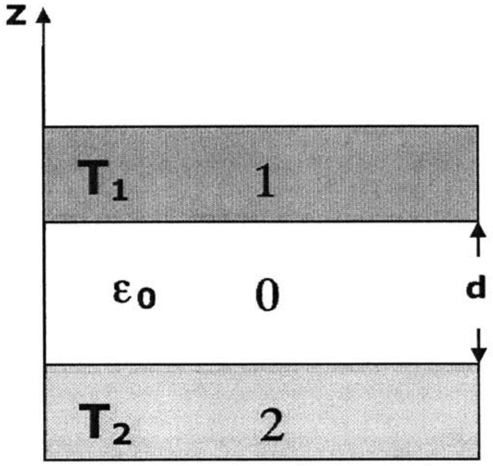

Figure 2.1 Two parallel plates are separated by a vacuum gap with distance *d*. Both plates are maintained at different temperatures.

First, Maxwell's equations need to be solved to obtain the electric and magnetic fields resulting from the fluctuation current densities.

$$\begin{aligned} &\nabla \times \boldsymbol{E} + \frac{\partial \boldsymbol{B}}{\partial t} = 0 \\ &\nabla \times \boldsymbol{H} - \frac{\partial \boldsymbol{D}}{\partial t} = \boldsymbol{J} \\ &\nabla \cdot \boldsymbol{D} = \rho \\ &\nabla \cdot \boldsymbol{B} = 0 \end{aligned} \tag{2.1}$$

D is the displacement field, ***E*** is the electric field, ***B*** is the magnetic induction, ***H*** is the magnetic field, ***J*** is the current density and ρ is the charge density. The constitutive relation between ***D*** and ***E***, and ***B*** and ***H*** are

$$\begin{aligned} \boldsymbol{D} &= \varepsilon_0 \varepsilon \boldsymbol{E} \\ \boldsymbol{B} &= \mu_0 \mu \boldsymbol{H} \end{aligned} \tag{2.2}$$

ε_0 is the vacuum electric permittivity, ε is the relative electric permittivity, μ_0 is the vacuum magnetic permeability, and μ is the relative magnetic permeability. For time harmonic fields of the form $\exp(-i\omega t)$ Eq. (2.1) reduces to

$$\begin{aligned} \nabla \times \boldsymbol{E} - i\omega\mu_0\mu\boldsymbol{H} &= 0 \\ \nabla \times \boldsymbol{H} + i\omega\varepsilon_0\varepsilon\boldsymbol{E} &= \boldsymbol{J} \\ \nabla \cdot \varepsilon_0\varepsilon\boldsymbol{E} &= \rho \\ \nabla \cdot \mu_0\mu\boldsymbol{H} &= 0 \end{aligned} \tag{2.3}$$

Taking the curl of the first equation in Eq. (2.3) and substituting the curl of ***H*** from the second equation in Eq. (2.3) yields

$$\nabla \times \nabla \times \boldsymbol{E} - k^2\boldsymbol{E} = i\omega\mu_0\boldsymbol{J} \tag{2.4}$$

The response field ***E*** to the current density ***J*** can be obtained by solving Eq. (2.4). To solve Eq. (2.4) we will use the Green's function method. The dyadic Green's function relates the vector electromagnetic field to the vector current source. The derivation in this section follows the outline by Tsang *et al.* [120]. Electric and magnetic fields are a convolution of the dyadic Green's function with the current density.

$$\boldsymbol{E}(\boldsymbol{r},\omega) = i\omega\mu_0 \int_{V'} \overline{\overline{\boldsymbol{G}}}_e(\boldsymbol{r},\boldsymbol{r}',\omega)\cdot\boldsymbol{J}(\boldsymbol{r}',\omega)\,dr' \tag{2.5}$$

$$\boldsymbol{H}(\boldsymbol{r},\omega) = \int_{V'} \overline{\overline{\boldsymbol{G}}}_h(\boldsymbol{r},\boldsymbol{r}',\omega)\cdot\boldsymbol{J}(\boldsymbol{r}',\omega)\,d\boldsymbol{r}' \tag{2.6}$$

$$\boldsymbol{J}(\boldsymbol{r},\omega) = \int_{V'} \overline{\overline{\boldsymbol{I}}}\delta(\boldsymbol{r}-\boldsymbol{r}')\cdot\boldsymbol{J}(\boldsymbol{r}',\omega)\,d\boldsymbol{r}' \tag{2.7}$$

$\overline{\overline{\boldsymbol{G}}}_e(\boldsymbol{r},\boldsymbol{r}',\omega)$ and $\overline{\overline{\boldsymbol{G}}}_h(\boldsymbol{r},\boldsymbol{r}',\omega)$ are the dyadic green's functions for the electric and magnetic field. $\boldsymbol{r}$ and $\boldsymbol{r}'$ are the location of the response field and location of the current source, respectively. Substituting Eqs. (2.5) and (2.7) into Eq. (2.4) gives

$$\nabla\times\nabla\times\overline{\overline{\boldsymbol{G}}}_e(\boldsymbol{r},\boldsymbol{r}')-k^2\overline{\overline{\boldsymbol{G}}}_e(\boldsymbol{r},\boldsymbol{r}')=\overline{\boldsymbol{I}}\delta(\boldsymbol{r},\boldsymbol{r}') \tag{2.8}$$

The Dyadic Green's function is the solution for the above differential equation. Fortunately, the dyadic Green's function for one-dimensional layered media is widely known. In the case of propagation in homogeneous, isotropic infinite medium with a delta source at $\boldsymbol{r}'$, the dyadic Green's function for the electric field is given by [120]

$$\overline{\overline{\boldsymbol{G}}}_e(\boldsymbol{r},\boldsymbol{r}')=\begin{cases}\dfrac{i}{8\pi^2}\displaystyle\int d\boldsymbol{k}_\perp\frac{1}{k_z}\left[\hat{\boldsymbol{e}}(k_z)\hat{\boldsymbol{e}}(k_z)+\hat{\boldsymbol{h}}(k_z)\hat{\boldsymbol{h}}(k_z)\right]e^{i\boldsymbol{k}(\boldsymbol{r}-\boldsymbol{r}')}\\ \dfrac{i}{8\pi^2}\displaystyle\int d\boldsymbol{k}_\perp\frac{1}{k_z}\left[\hat{\boldsymbol{e}}(-k_z)\hat{\boldsymbol{e}}(-k_z)+\hat{\boldsymbol{h}}(-k_z)\hat{\boldsymbol{h}}(-k_z)\right]e^{i\boldsymbol{K}(\boldsymbol{r}-\boldsymbol{r}')}\end{cases} \tag{2.9}$$

$\hat{\boldsymbol{e}}(\pm k_z)=(k_y\hat{\boldsymbol{x}}-k_x\hat{\boldsymbol{y}})/k_\rho$ and $\hat{\boldsymbol{h}}(\pm k_z)=\mp k_z/\boldsymbol{k}(k_x\hat{\boldsymbol{x}}+k_y\hat{\boldsymbol{y}})/k_\rho+k_\rho/k\hat{\boldsymbol{z}}$ are unit vectors perpendicular to $(k_x\hat{\boldsymbol{x}}+k_y\hat{\boldsymbol{y}}\pm k_z\hat{\boldsymbol{z}})$, $\boldsymbol{k}_\perp=k_x\hat{\boldsymbol{x}}+k_y\hat{\boldsymbol{y}}$, $\boldsymbol{k}=k_x\hat{\boldsymbol{x}}+k_y\hat{\boldsymbol{y}}+k_z\hat{\boldsymbol{z}}$, and $\boldsymbol{K}=k_x\hat{\boldsymbol{x}}+k_y\hat{\boldsymbol{y}}-k_z\hat{\boldsymbol{z}}$. k_x and k_y are the in-plane components of the wave vector, k_z is the out-of-plane component, and $k_\rho=\sqrt{k_x^2+k_y^2}$. The Green's function in layered materials that do not contain a delta source, which we shall call the homogeneous part, is given by [120]

$$\begin{aligned}\overline{\overline{\boldsymbol{G}}}_e(\boldsymbol{r},\boldsymbol{r}')=\frac{i}{8\pi^2}\int d\boldsymbol{k}_\perp\frac{1}{k_z}\Big\{&\left[A_l\hat{\boldsymbol{e}}_l(k_{lz})e^{i\boldsymbol{k}_l\cdot\boldsymbol{r}}+B_l\hat{\boldsymbol{e}}_l(-k_{lz})e^{i\boldsymbol{K}_l\cdot\boldsymbol{r}}\right]\hat{\boldsymbol{e}}(-k_z)e^{-i\boldsymbol{K}\cdot\boldsymbol{r}'}\\ &\left[C_l\hat{\boldsymbol{h}}_l(k_{lz})e^{i\boldsymbol{k}_l\cdot\boldsymbol{r}}+D_l\hat{\boldsymbol{h}}_l(-k_{lz})e^{i\boldsymbol{K}_l\cdot\boldsymbol{r}}\right]\hat{\boldsymbol{h}}(-k_z)e^{-i\boldsymbol{K}\cdot\boldsymbol{r}'}\Big\}\end{aligned} \tag{2.10}$$

For the case of two parallel plates, Eq. (2.10), the Green's function for electric field in layer 2 due to current source in layer 1 and vice versa, can be simplified to

$$\begin{aligned}\overline{\overline{\boldsymbol{G}}}_e(\boldsymbol{r},\boldsymbol{r'}) = \frac{i}{8\pi^2}\int d\boldsymbol{k}_\perp \frac{1}{k_z}\Big\{&T^{TE}\hat{\boldsymbol{e}}_t(-k_{tz})e^{i\boldsymbol{K}_t\cdot\boldsymbol{r}}\hat{\boldsymbol{e}}(-k_z)e^{-i\boldsymbol{K}\cdot\boldsymbol{r'}}\\ &+T^{TM}\hat{\boldsymbol{h}}_t(-k_{tz})e^{i\boldsymbol{K}_t\cdot\boldsymbol{r}}\hat{\boldsymbol{h}}(-k_z)e^{-i\boldsymbol{K}\cdot\boldsymbol{r'}}\Big\}\end{aligned} \tag{2.11}$$

Using Maxwell's equations it can be shown that

$$\overline{\overline{\boldsymbol{G}}}_h = \nabla\times\overline{\overline{\boldsymbol{G}}}_e \tag{2.12}$$

Now we can calculate the electric and magnetic fields in region 2 resulting from a current source in region 1 and vice versa by substituting Eq. (2.11) back into Eqs. (2.5) and (2.6). Coefficients *A*, *B*, *C*, *D* in Eq. (2.10) and the transmission coefficient T^{TE} and T^{TM} in Eq. (2.11) can be determined by satisfying boundary conditions at the interface. The transfer matrix method is generally used to calculate these coefficients [121], [122].

Radiative energy transfer is obtained by calculating the Poynting vector, which is the cross product of electric and magnetic field.

$$\langle S(r,\omega)\rangle = \frac{1}{2}\mathrm{Re}\left(E\times H^*\right) \tag{2.13}$$

The brackets denote a statistical ensemble average. The components of the cross products can then be written as [123]

$$\left\langle E_i H_j^*\right\rangle = i\omega\mu_0\int_{V'} dr'\int_{V'} dr''\,\overline{\overline{G}}_{e_{ik}}(r,r',\omega)\overline{\overline{G}}_{h_{jl}}(r,r',\omega)\left\langle J_k(r')J_l(r'')\right\rangle \tag{2.14}$$

Notice that for two parallel plates we are only interested in the Poynting vector in the z-direction.

In Eq. (2.14) the spectral density of the current density (i.e., the ensemble average of the spatial correlation function of the current density) is required to calculate the Poynting vector. The fluctuating current densities originate from random thermal charge fluctuations. The Fluctuation Dissipation Theorem (FDT) is used to relate the spectral density of the current density to the local temperature of a medium [123]–[126].

$$\begin{aligned}\left\langle \boldsymbol{J}_k(\boldsymbol{r},\omega)\boldsymbol{J}_l^*(\boldsymbol{r}',\omega)\right\rangle &= \lim_{r'\to r}\frac{1}{\Delta V'}\frac{\varepsilon_0\varepsilon''(\omega)\omega\theta(\omega,T)}{\pi}\delta_{kl}\\ &= \frac{\varepsilon_0\varepsilon''(\omega)\omega\theta(\omega,T)}{\pi}\delta_{kl}\delta(r-r')\end{aligned} \tag{2.15}$$

$\theta(\omega,T)$ is the mean energy of the Planck oscillator at frequency ω and in thermal equilibrium T.

$$\theta(\omega,T)=\frac{\hbar\omega}{2}+\frac{\hbar\omega}{\exp(\hbar\omega/k_BT)-1} \tag{2.16}$$

$\hbar = h/2\pi$ is Planck's constant over 2π and k_B is the Boltzmann constant. The term $\hbar\omega/2$ accounts for the zero-point energy and is necessary in the Casimir force calculation. This term can however be omitted in the net radiative heat flux calculation, since it does not provide a net flux. Eq. (2.15) can then be substituted into Eq. (2.14) to calculate the Poynting vector. δ_{kl} assumes that the medium is isotropic. There is no coupling between currents with orthogonal direction. $\delta(\boldsymbol{r}-\boldsymbol{r}')$ assumes that the currents at point $\boldsymbol{r}'$ and $\boldsymbol{r}$ are not correlated.

After a series of mathematical manipulations, the net radiative heat flux between two semi-infinite parallel plates separated by a vacuum gap d can be expressed as [127]

$$q_{1-2}^{net,prop} = \frac{1}{\pi^2} \int_{\omega=0}^{\infty} [\theta(\omega,T_1) - \theta(\omega,T_2)] d\omega \times$$

$$\times \int_{k_r=0}^{\omega/c_0} \underbrace{\left[\frac{\left(1-\left|r_{01}^{s,p}\right|^2\right)\left(1-\left|r_{02}^{s,p}\right|^2\right)}{4\left|1-r_{01}^{s,p} r_{02}^{s,p} exp(2ik_{z0}d)\right|^2} \right]}_{Transfer\ function} k_r dk_r \tag{2.17}$$

$$q_{1-2}^{net,eva} = \frac{1}{\pi^2} \int_{\omega=0}^{\infty} [\theta(\omega,T_1) - \theta(\omega,T_2)] d\omega \times$$

$$\times \int_{k_r=\omega/c_0}^{\infty} \underbrace{exp(-2Imag(k_{z0})d) \left[\frac{Imag(r_{01}^{s,p}) Imag(r_{02}^{s,p})}{\left|1-r_{01}^{s,p} r_{02}^{s,p} exp(-2Imag(k_{z0})d)\right|^2} \right]}_{Transfer\ function} k_r dk_r \tag{2.18}$$

where $\boldsymbol{k}_r$ is the wavevector component parallel to the interface and k_z is the wavevector component perpendicular to the interface. The wave vectors in media 1 and 2 are $\boldsymbol{k}_1 = \sqrt{\varepsilon_1}\boldsymbol{k}_0$ and $\boldsymbol{k}_2 = \sqrt{\varepsilon_2}\boldsymbol{k}_0$, where $k_0 = \omega / c_0 = 2\pi / \lambda$ is the magnitude of the wavevector in vacuum. r_{01} is the Fresnel reflection coefficient between medium 0 and medium 1. Superscripts denote s-polarization (TE), and p-polarization (TM), $r_{01}^s = (k_{z0} - k_{z1}) / (k_{z0} + k_{z1})$, $r_{01}^p = (\varepsilon_1 k_{z0} - \varepsilon_0 k_{z1}) / (\varepsilon_1 k_{z0} + \varepsilon_0 k_{z1})$, where $k_{z0} = \sqrt{k_0^2 - k_r^2}$, and $k_{z1} = \sqrt{k_1^2 - k_r^2}$. The boundary condition on the interface requires that the parallel wavevector k_r must always be the same. The parallel wavevector k_r must also be real since the amplitude of the wave may not change in the $\boldsymbol{r}$-direction. Propagating waves exist in vacuum when k_{z0} is real ($k_r \leq \omega/c_0$). Evanescent waves exist in vacuum when k_{z0} is imaginary. In this case, the field decays exponentially in the $\boldsymbol{z}$-direction. Equations (2.17) and (2.18) are the net total radiative heat flux for propagating ($k_r \leq \omega/c_0$) and evanescent modes ($k_r > \omega/c_0$), respectively.

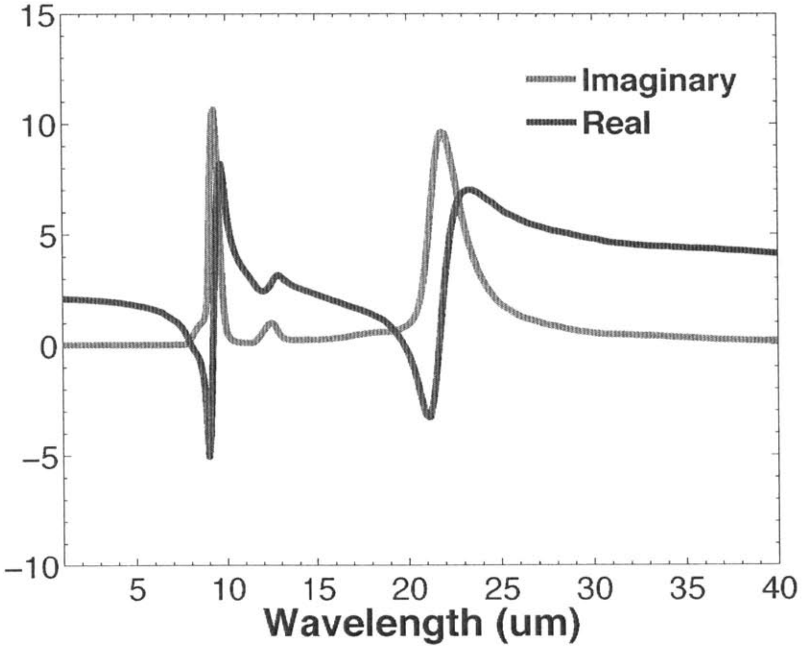

Figure 2.2 Dielectric constant of glass [1].

As an example, we calculate and analyze the near-field thermal radiation between two parallel glass plates. Glass is chosen due to its experimental relevance. Figure 2.2 presents the dielectric constant of glass [1]. Figure 2.3 presents contour plots of the imaginary part of reflection coefficient as a function of angular frequency and parallel wavevector for both TM and TE modes. The imaginary part of the reflection coefficient is proportional to the energy density of the electromagnetic waves on the surface of the emitting medium [47]. The imaginary part of the reflection coefficient can also be considered as a generalized emissivity [127]. The area on the left side of the light line is the propagating waves region where the parallel wavevector is smaller than ω/c. The area on the right is the evanescent wave region where parallel wavevector is larger than ω/c.

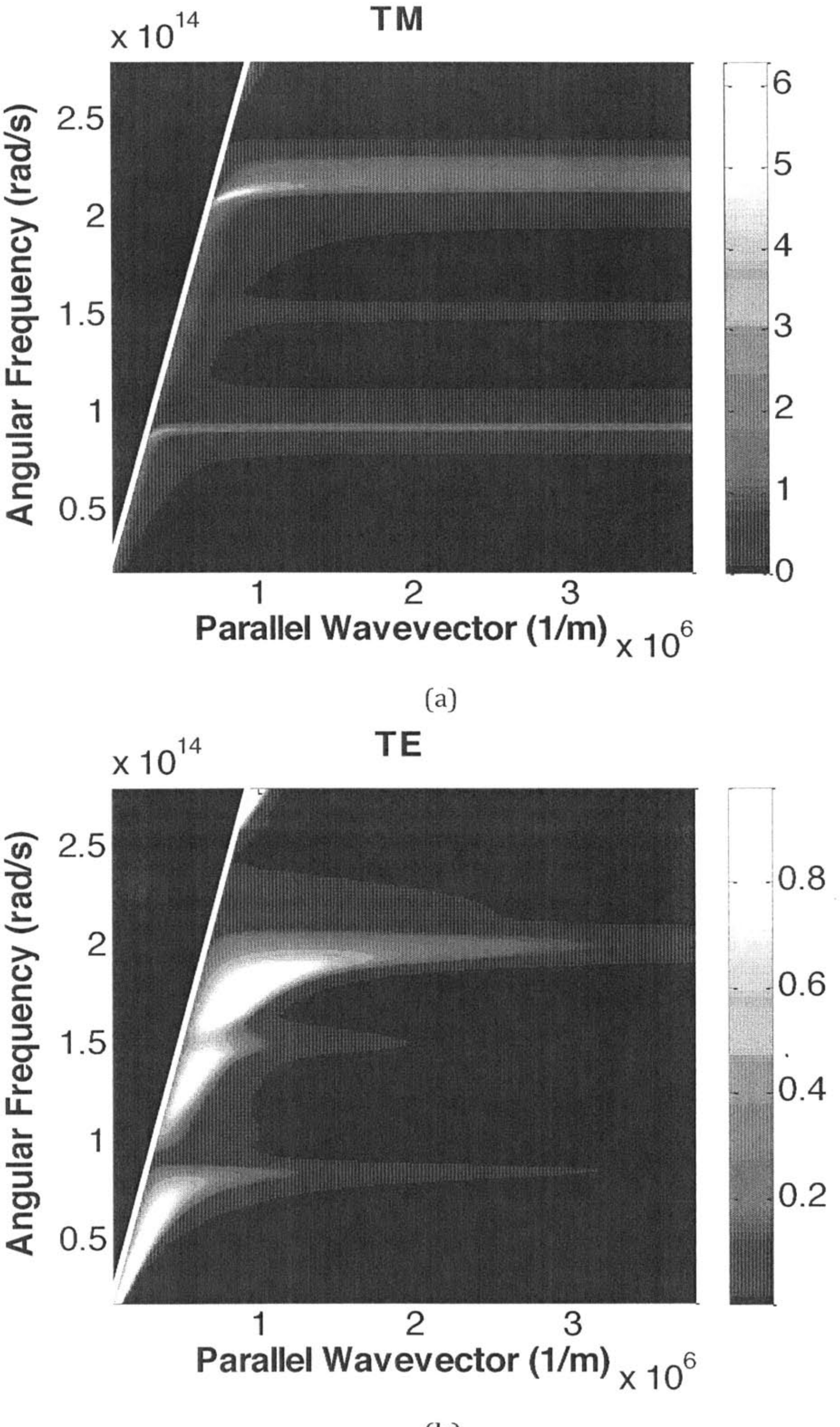

(a)

(b)

Figure 2.3 Imaginary part of reflection coefficient of (a) TM and (b) TE modes for glass. The color bar indicates the magnitude. The white diagonal line is the light line. Note that the color bar for TM modes is one order of magnitude greater than that of TE modes.

In figure 2.3a, the heat flux contribution from surface phonon polaritons can be observed at angular frequencies of ~ 2.2161 x 10^{14} rad/s (8.5 um) and ~ 9.2791 x 10^{13} (20.3 um). The heat flux due to surface phonon polaritons remains significant as parallel wavevector goes to infinity. This explains the divergence of the heat flux by surface phonon polaritons. Evanescent waves with large parallel wavevectors decay very fast. These modes do not contribute significantly to the heat transfer when the separation distance is relatively large compared to the corresponding wavelength for a particular wavevector $\lambda \sim 1/k$. As the separation distance decreases, these modes start to contribute to the heat transfer. As a consequence, the radiative heat transfer diverges when the separation distance becomes smaller since more modes with large wavevectors are able contribute to the heat transfer. This existence of TM modes with very large wavevectors is a consequence of neglecting the spatial dispersion of the dielectric constant [54], [55].

Theoretical studies on nonlocal effect of dielectric constant on near-field thermal radiation have been done for both metals and dielectrics. Chapuis et al. [54] study the effect of nonlocal dielectric constant in metal. The nonlocal dielectric constant is modeled using the Lindhard-Mermin and Boltzmann-Mermin models. The nonlocal dielectric constant does not affect the s-polarized waves, which dominate the heat transfer between metallic surfaces. The nonlocal dielectric constant affects the p-polarized waves by introducing an upper limit for the wave vector. This effect only influences near-field thermal radiation for gaps smaller than 2 nm. Joulain et al. [55] demonstrate the effect of the nonlocal dielectric constant on near-field thermal radiation by replacing delta function in Eq (2.15) with a Gaussian function. As a consequence, the thermal current are correlated to a certain distance. This correlation length sets a lower limit for the wavelength or an upper limit for the wavevector that can exist in the medium. Although this correlation length is unknown, the effect was observed as the saturation of the heat flux when the separation distance is very small. Chiloyan et al. [56] developed an atomistic framework based on microscopic Maxwell's equations and lattice dynamics and compared it with the fluctuating electrodynamics approach. Both approaches are found to be in excellent agreement for separation distance larger than 1 nm. At sub-nanometer gaps the two approaches differ significantly as the acoustic phonon tunneling dominates in this regime. Of experimental interest, this regime is still not accessible due to the limitation on the experimental setup.

Figure 2.4 shows the spectral radiative heat flux as a function of wavelength for two parallel glass plates separated by a 100 nm vacuum gap. Resonant peaks due to surface phonon polaritons are observed at wavelengths of 8.5 μm and 20.3 μm. These two peaks correspond to specific wavelengths where the real part of dielectric constant is equal to -1, as shown in figure 2.4. Surface phonon polaritons allow radiative heat transfer to be orders of magnitude greater than black body radiation [2]. Another peak is also observed at a wavelength of 12.4 μm. This is different from the other two peaks because this peak does not originate from surface waves. This peak is due to the strong absorption of bulk polaritons as can be seen in figure 2.4 by a peak in the imaginary part of dielectric constant while the real part of the dielectric constant is positive.

The contribution of TE modes to the total radiative heat flux is very small. This can be seen by looking at the spectral radiative heat flux and the dielectric constant of glass. The real part of the dielectric constant is negative for certain frequency ranges where surface phonon polaritons exist in TM modes. Electromagnetic waves do not exist inside glass for these frequency ranges. While TM modes can support surface phonon polaritons at the interface between glass and vacuum, TE modes cannot. As can be seen in figure 2.4, the spectral heat flux for TE modes at these frequency ranges is minimum, leading to a small contribution to the total heat transfer.

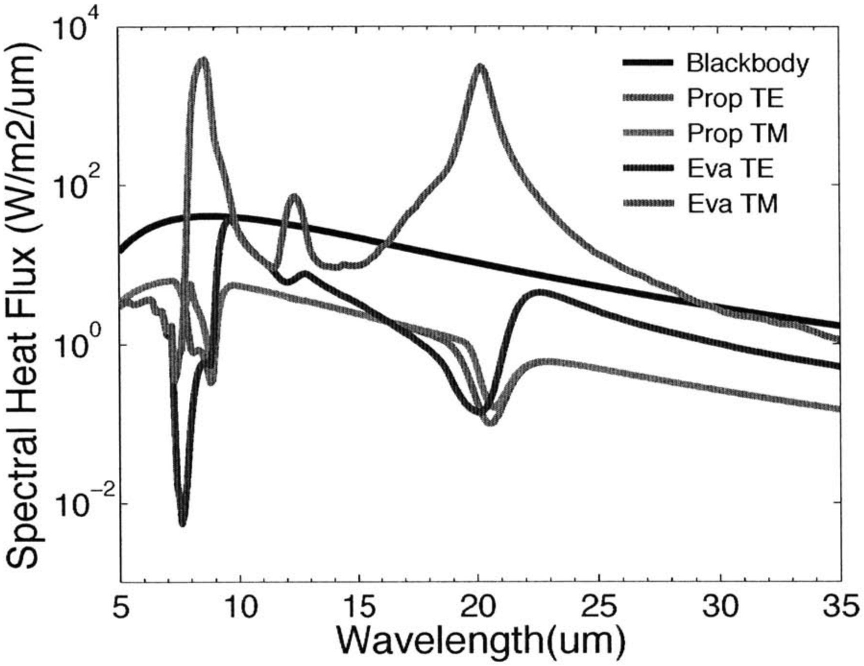

Figure 2.4 Spectral radiative heat transfer flux of each mode between two parallel glass plates separated by 100 nm vacuum gap. T_1 = 320 K and T_2 = 300 K.

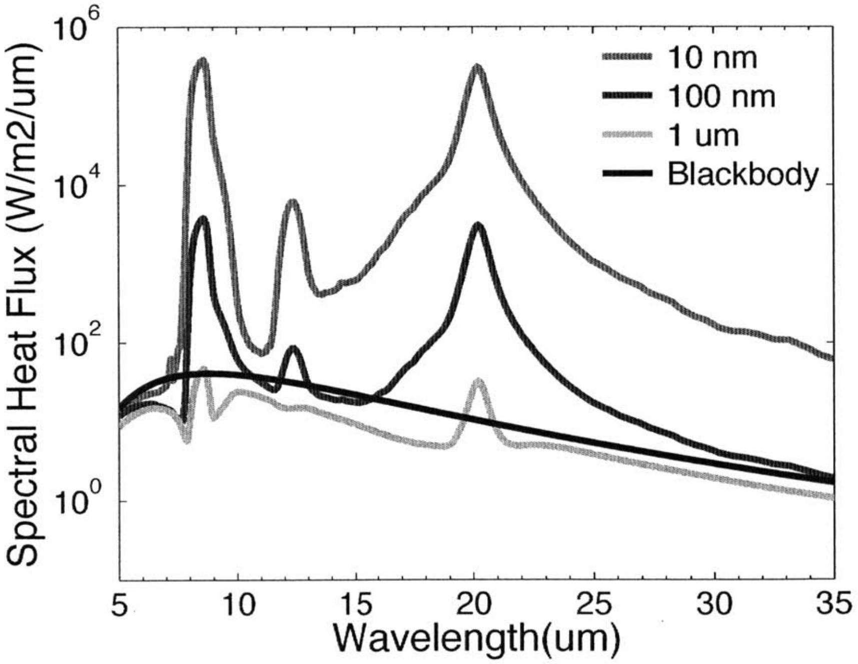

Figure 2.5 Spectral radiative heat transfer flux between two parallel glass plates separated by different vacuum gap. T_1 = 320 K and T_2 = 300 K. Heat transfer increases as the separation gap becomes smaller.

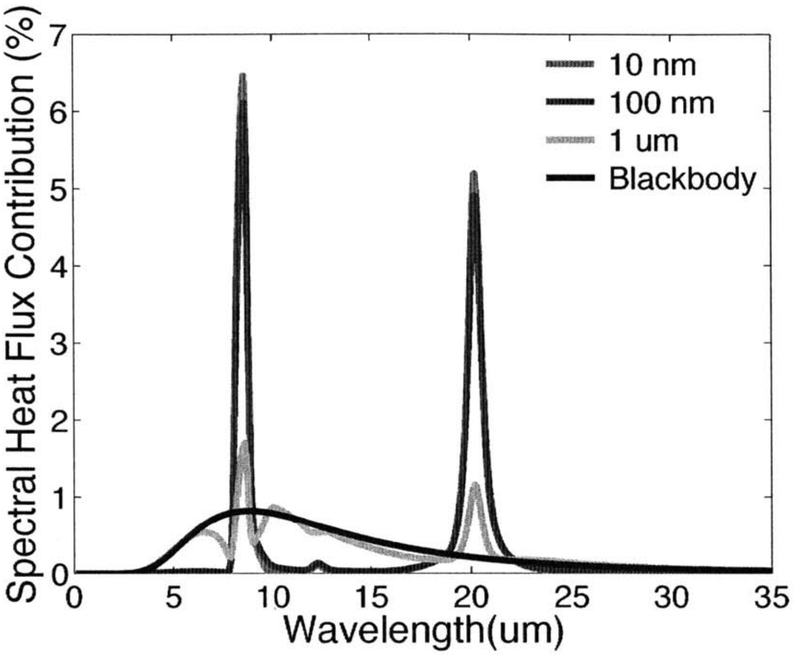

Figure 2.6 Spectral radiative heat transfer flux contribution between two parallel glass plates separated by different vacuum gap. T_1 = 320 K and T_2 = 300 K.

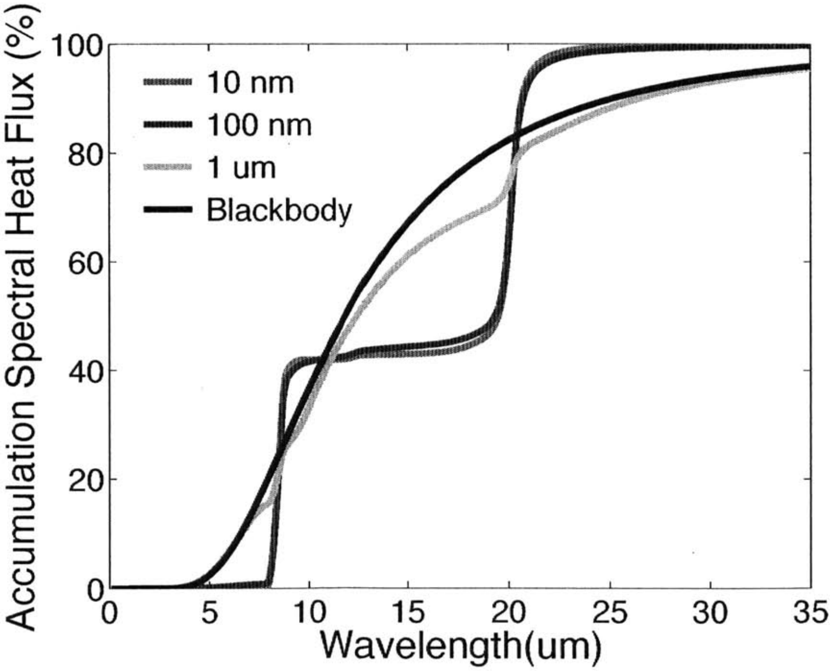

Figure 2.7 Accumulative spectral radiative heat transfer flux contribution between two parallel glass plates separated by different vacuum gap. T_1 = 320 K and T_2 = 300 K.

Figures 2.6 and 2.7 show the spectral and accumulative spectral contribution of surface phonon polaritons to the total radiative heat transfer. Those figures show that the surface phonon polaritons dominate the radiative transfer when the separation gap is smaller than 100 nm. The radiative transfer becomes monochromatic as the surface phonon polaritons becomes dominant [22].

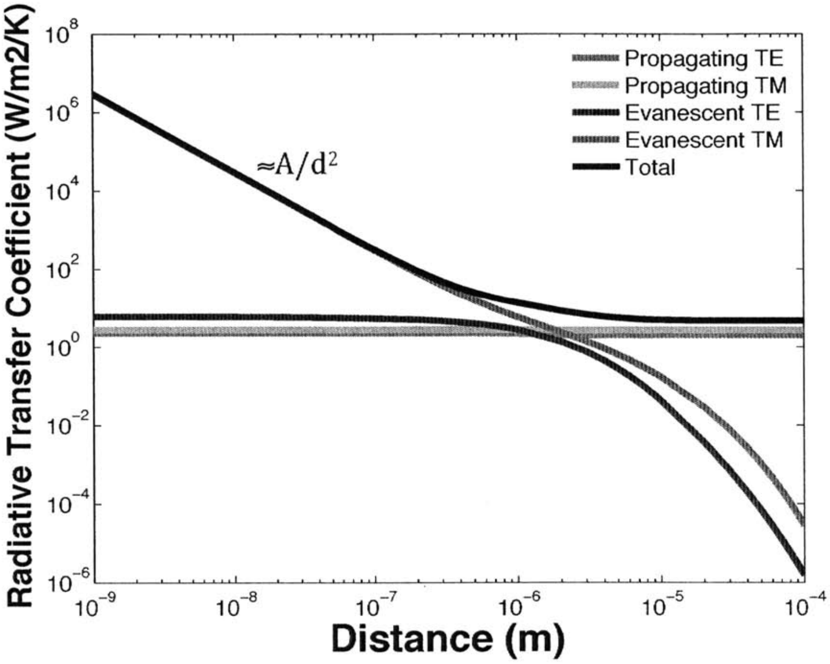

Figure 2.8 Radiative transfer coefficient between two parallel glass plates as a function of separation distance. T_1 = 320 K and T_2 = 300 K. Heat transfer increases as the separation gap becomes smaller. Evanescent wave contribution is orders of magnitude larger than the propagating contribution due to the surface phonon polaritons.

Figure 2.8 shows the radiative heat flux between two parallel glass substrates as a function of separation distance. The total radiative heat transfer increases when the separation distance decreases due to contributions from evanescent waves. When *d* is relatively large, the radiative transfer from evanescent modes is negligible, since evanescent fields decay exponentially in the ***z***-direction as suggested by the factor $e^{-2\mathrm{Im}(k_z)d}$ in Eq. (2.17). When *d* is relatively small, the evanescent waves can tunnel to the other medium. The radiative transfer from evanescent modes becomes the dominating factor at micron separation distances and below. This heat transfer mode can be considered as an additional heat transfer channel [47] and consequently the radiative heat transfer can exceed blackbody radiation, predicted by the Stefan-Boltzmann law. Asymptotic analysis shows A/d^2 dependence of the heat transfer with respect to the separation gap as can be seen in figure 2.8, where A is a constant which depends on the temperature, and d is the separation gap. This $1/d^2$ behavior is due to the domination of the surface phonon polaritons when the separation gap is very small.

Figure 2.9 plots the coefficient A as a function of temperature of the glass plate. By linearizing the plot, A can be approximated as

$$A(T) \cong 3.55 \times 10^{-12}\, T \tag{2.19}$$

Near-field heat transfer coefficient between two parallel glass plates separated with a gap smaller than 100 nm at room temperature can then be approximated as

$$h_{nf} \cong \frac{3.55 \times 10^{-12}}{d^2}\,(T_{hot} - T_{cold}) \tag{2.20}$$

This approximation is best used for $d \leq 100$nm and $280K < T < 400K$.

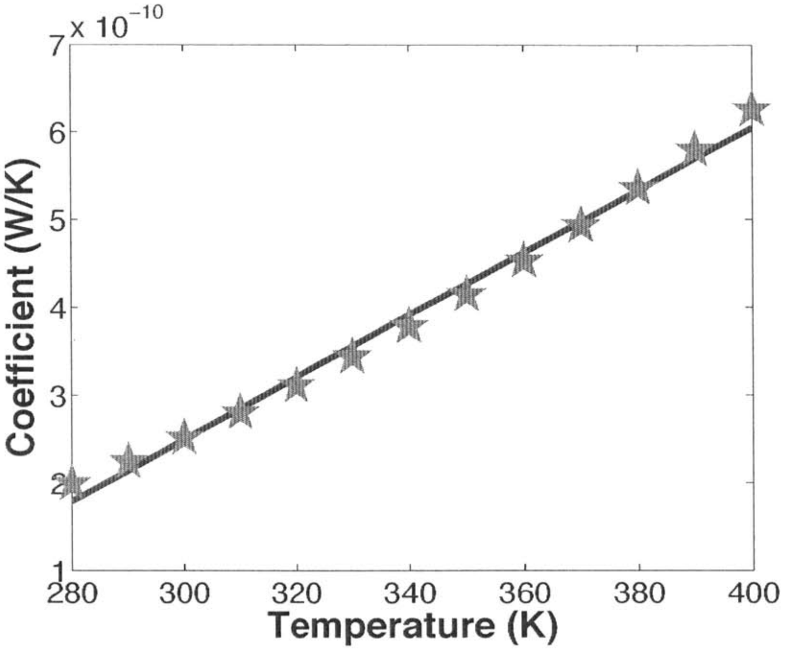

Figure 2.9 Coefficient A is plotted as a function of temperature. Coefficient A can be approximated using the slope of the linearized plot.

2.2 Proximity approximation to Calculate Near-Field Radiative Heat Transfer between a sphere and plate

The near-field radiative transfer between a sphere and a plate is of interest due to its experimental relevance. But since the calculation of the near-field radiative transfer between a sphere and a plate involve more complicated numerical simulation, we use the proximity force theorem, which is widely used to approximate the force between a sphere and a plate, to later compare the experimental result with the theoretical calculation.

The proximity approximation is a simple yet an accurate tool to estimate near-field thermal radiation between a sphere and a plate. Studies have shown that at very small gaps, gap << radius, the approximation agrees very well with the exact calculation [37], [38], [46].

In this approximation, the sphere is considered very large relative to the separation distance that the curvature of the sphere changes very slowly. The curved surface is approximated by differential flat areas, as shown in figure 2.10.

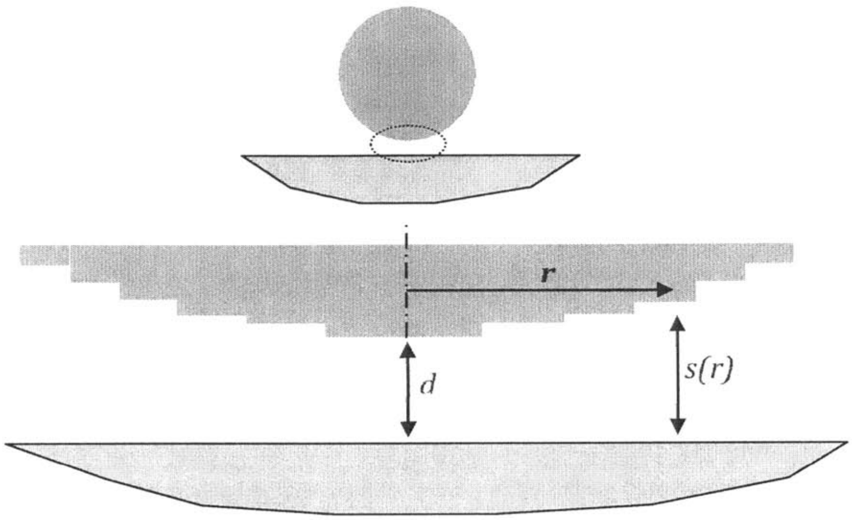

Figure 2.10 Proximity force theorem approximates the curved surface of the microsphere by differential flat surfaces.

The near-field radiative conductance between a sphere and a plate can be approximated by two parallel plates solution.

$$G_{near-field}^{sphere-plate}(d) = \int_{r=0}^{R} h_{near-field}^{plate-plate}\left(s(r)\right)2\pi r dr \qquad (2.21)$$

G is the radiative conductance, d is the separation distance between the sphere and the substrate, R is the radius of the sphere, h is the radiative heat transfer coefficient, and $s = d + R - \sqrt{R^2 - r^2}$ is the separation distance of between each differential plate and the substrate. Eq. (2.21) can also be approximated as

$$G_{near-field}^{sphere-plate}(d) \cong 2\pi R \int_{s=d}^{R+d} h_{near-field}^{plate-plate}(s)ds \qquad (2.22)$$

Using the proximity approximation, near-field heat conductance between a sphere with radius R and a semi-infinite plate which support surface phonon polaritons can be approximated as

$$G_{nfsphere-plate} \cong 2\pi R d h_{nf} \qquad (2.23)$$

while near-field heat conductance between two spheres with radius *R* which support surface phonon polaritons can be approximated as

$$G_{nf2spheres} \cong \pi R d h_{nf} \qquad (2.24)$$

By applying Eq. (2.20) to Eq. (2.22) and (2.23), one can quickly estimate the near-field thermal conductance between a glass sphere and a glass plate or 2 glass spheres.

2.3 Summary

Theoretical background to analyze near-field thermal radiation based on fluctuational electrodynamic was presented. Silicon dioxide is used as an example material due to its experimental relevance. The physical origin of near-field thermal radiation and its consequences are explained using detail analysis such as transfer function, spectral heat flux, and total heat transfer. The proximity approximation to analyze near-field thermal radiation between curved objects is also explained due to the experimental relevance. Empirical expressions to calculate near-field thermal radiation between silicon dioxide surfaces are presented for engineering purpose. Theoretical analysis presented in this chapter is used to guide the experimental investigation of near-field thermal radiation presented in the later chapters.

Chapter 3

Near-Field Thermal Radiation Measurement Setup

This chapter presents the near-field thermal radiation measurement apparatus and procedures. The basic concept of the measurement is first explained. Then, the details of the setup and procedures are presented. Finally, the problems with the setup and the improvements made are explained.

3.1 Measurement Setup

The simplest geometry in the study of near-field thermal radiation is the case of two parallel plates. But despite its simplicity, near-field thermal radiation between two parallel plates is difficult to measure, mainly due to the complications involved in aligning two parallel plates with a nanometer separation gap. Most recent experimental investigations on near-field thermal radiation between two parallel plates was reported by Ottens et al. [60] and Kralik et al. [61], [72]. Ottens et al. measure near-field thermal radiation between two large sapphire plates (50 x 50 mm^2). The gap is controlled by measuring the capacitance of a pair of copper plates on each corner of the sapphire plates. Measurements were carried out for temperature differences ranging from 6.8 to 19 K as the gap is varied from 2 to 100 um. Kralik et al. [61], [72] reported near-field thermal radiation measurement between two parallel tungsten plates with a 35 mm diameter at cryogenic temperature. The gap is varied from 1 to 300 um. The measurement results shows two orders of magnitude enhancement of near-field thermal radiation relative to the blackbody radiation. Due to the complications in maintaining a small separation distance between two parallel plates both reported that they can only measured gap as small as 1 um. Sphere-plate measurement setup was designed to solve this problem [62]. The use of a sphere eliminates the parallelism problem suffered by two plates.

Tip-plate is another configuration that is commonly used to measure near-field thermal radiation. Due to its small size, this configuration minimizes the probability of the surface of being dirty. However, the sphere-plate configuration is still preferable than tip-plate configuration because a sphere is more amenable to analysis compared to a tip. The geometry of the tip is difficult to model thus any comparisons between theoretical and experimental results inherently include more uncertainty.

To reduce the probability of the surface of being dirty and causing uncertainties in the measurement results, a very small sphere is used in the measurement. However, this strategy comes with a drawback. Because of its size (≈100 um), the measured near-field radiative heat flux is very small (≈100s nW). This results in a challenging problem on designing the measurement system. To measure such a small heat flux, Narayanaswamy et al. [62] were the first to design a near-field thermal radiation measurement setup using a bimaterial cantilever. A bimaterial cantilever utilizes different materials with different thermal expansion coefficients. Mismatch in the thermal expansion coefficient causes deflection of the bimaterial cantilever. This effect is widely used for heat flux measurement. This effect is more pronounced in a microscale cantilever due to their thickness, resulting in reduced stiffness. A bimaterial cantilever is a very sensitive heat flux sensor. A measurement setup employing a bimaterial cantilever has been demonstrated to have a resolution less than 4 pW [80].

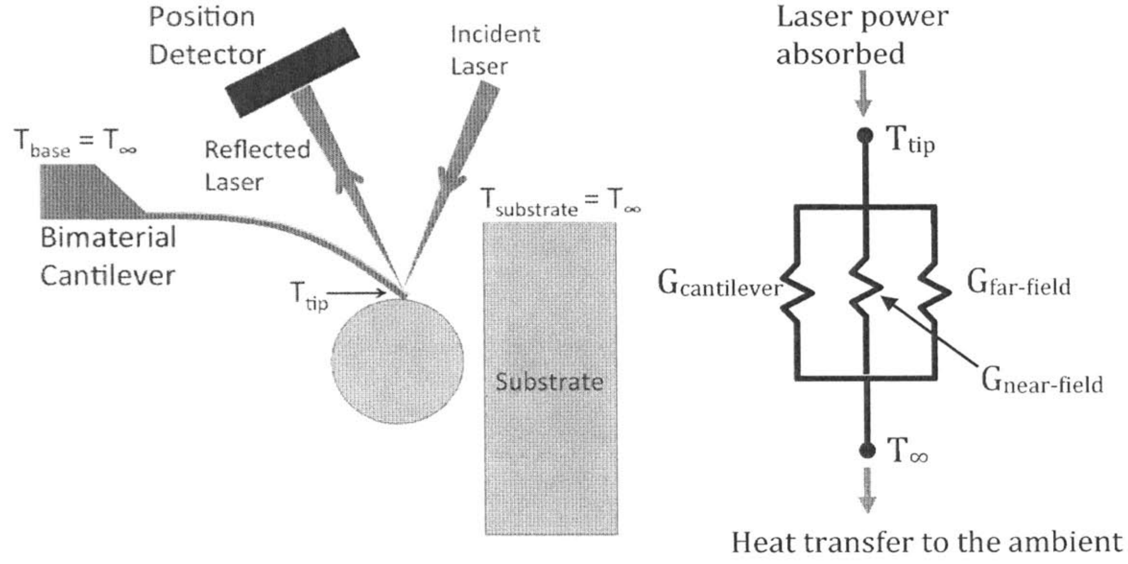

(a) (b)

Figure 3.1 (a) A schematic of the bimaterial cantilever sensor used in the measurement setup. As the separation gap between the substrate and the sphere is reduced, the heat flux increases due to the near-field effect. The temperature of the sphere and cantilever decreases due to net heat transfer from the sphere to the substrate. The change in the temperature profile results in the bending of the cantilever, which then measured as the near-field heat flux. (b) Equivalent thermal circuit of the bimaterial cantilever used to measure near-field thermal radiation.

Figure 3.1a illustrates the basic idea of our measurement setup. A microsphere is attached on the tip of a bimaterial cantilever. A flat substrate is positioned in front of the sphere. A laser source is shined on the tip of a cantilever. Some part of the laser beam is absorbed by the cantilever and acts as heating source to create a temperature difference between the sphere and the substrate, while the substrate is passively maintained at room temperature. The reflected laser is directed to a position detector to measure the bending of the cantilever.

The corresponding thermal circuit of the cantilever and the sphere system is given in figure 3.1b. The temperature of the cantilever tip can be written as

$$T_{tip} = \frac{P}{\left[G_{near-field} + G_{far-field} + G_{cantilever}\right]} + T_{\infty} \qquad (3.1)$$

P is the laser power absorbed by the cantilever, $G_{near\text{-}field}$ is the near-field radiation thermal conductance between the sphere and the substrate, $G_{far\text{-}field}$ is the far-field radiation thermal conductance between the sphere and the cantilever to the surroundings, and $G_{cantilever}$ is the thermal conductance of the cantilever. The deflection of the cantilever is very small (≈1 nm) such that the amount of the laser power absorbed by the cantilever tip, P, is assumed to be constant during the experiment. The cantilever tip is assumed to be at the same temperature as the sphere, since the near-field thermal radiative heat transfer from the microsphere to the substrate is very small (~100 nW). For comparison, the conduction through the cantilever is in the order of (~100 μW).

The experiment is done based on the following idea. $G_{near\text{-}field}$ increases due to the tunneling of the evanescent waves as the separation gap between the sphere and the substrate becomes smaller. As a result, the temperature T_{tip} will decrease to balance the heat flow following Eq. (3.1). This temperature change will cause the cantilever to bend upwards and change the position of the reflected beam on the position detector. A calibration factor is needed to convert the displacement of the position of the reflected beam into near-field conductance $G_{near\text{-}field}$. The calibration procedures are explained in Section 3.2.

Here, we emphasize that our experimental setup only measures near-field radiative transfer. Far-field radiation contributes to the initial bending of the cantilever and remained constant during measurement.

3.2 Calibration Process

The calibration process is done to convert the recorded signal during measurement into near-field conductance. In this section, the absorbed power calibration is first explained. This calibration is needed to convert the bending of the cantilever into heat flux. Next, the base temperature calibration is explained. This calibration is needed to experimentally determine the effective thermal conductance of the cantilever along with the absorbed power calibration. The effective thermal conductance of the cantilever is then used to determine the temperature difference between the sphere and the substrate.

3.2.1 Absorbed Power Calibration

The temperature profile of the cantilever under vacuum conditions with a point-like power input on its tip, as shown in Fig. 3.2, can be written as

$$T(x) - T_b = \left(1 - \frac{x}{l}\right)\frac{P}{G} \tag{3.2}$$

P is the laser power absorbed by the cantilever tip, G is the effective thermal conductance of the cantilever along its length direction, l is the effective length of the cantilever, and T_b is the base temperature. The effect of the far-field radiation is very small since the far field conductance of the cantilever $G_{far\text{-}field}$ (~60 nW/K) is very small compared to the cantilever thermal conductance $G_{cantilever}$ (~ 4.2 ± 2 μW/K).

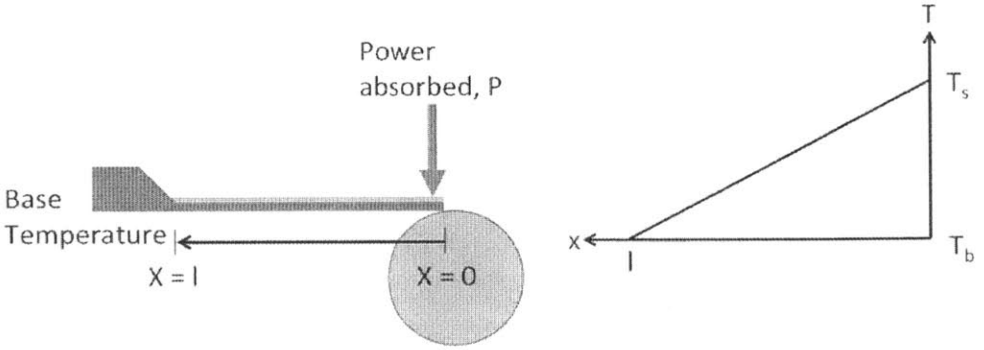

Figure 3.2 Schematic of the cantilever with power input on its tip in vacuum. Since the radiation loss (~60 nW/K) is very small compared to the cantilever thermal conductance (~ 4.2 μW/K), temperature profile along the cantilever is assumed to be linear.

Based on the beam theory [128], the deflection of a bi-material cantilever with two different thermal expansion coefficients follows

$$\frac{d^2Z}{dx^2} = 6(\gamma_2 - \gamma_1)\frac{t_1 + t_2}{t_1 t_2 K}[T(x) - T_0] \tag{3.3}$$

Z(x) is the vertical deflection at location *x*, *γ* is the thermal expansion coefficient, *t* is the thickness of the layers, *T(x)* is the temperature distribution along the cantilever, and T_0 the reference temperature at zero deflection. In this case T_0 is room temperature. *K* is a constant defined by the thickness ratio and the Young's modulus of the layers.

$$K = 4 + 6\left(\frac{t_1}{t_2}\right) + 4\left(\frac{t_1}{t_2}\right)^2 + \frac{E_1}{E_2}\left(\frac{t_1}{t_2}\right)^3 + \frac{E_2}{E_1}\left(\frac{t_2}{t_1}\right) \tag{3.4}$$

Based on the temperature profile, the slope of the cantilever tip can be determined from Eq. (3.3).

$$\frac{dZ(0)}{dx} = 6H\left\{-\frac{lP}{2G} - T_b l + T_0 l\right\} \tag{3.5}$$

Since in this case $T_b = T_0$, Eq. (3.5) reduces to

$$\frac{dZ(0)}{dx} = -\frac{3lPH}{G} \tag{3.6}$$

$H = (\gamma_2 - \gamma_1)(t_2 - t_1)/t_2 t_1 K$ is a constant obtained from Eq. (3.3). The slope of the cantilever tip is equal to half of the displacement of the reflected beam on the position detector when the angle is very small,

$$\frac{dZ(0)}{dx} = 0.5\frac{\Delta d}{s} \tag{3.7}$$

Δd is the displacement of the reflected beam on the PSD, and s is the distance between the cantilever tip and the PSD. The sensitivity of the displacement of the reflected beam on the PSD with respect to the absorbed power is given by

$$S_p = \frac{\partial(\Delta d)}{\partial P} = -\frac{6slH}{G} \tag{3.8}$$

This calibration is carried out by measuring the displacement of the reflected laser beam on the PSD in response to different laser powers absorbed at the tip of the cantilever under vacuum. The absorbed power is obtained by subtracting the reflected and transmitted from the incident laser power. The incident, transmitted, and reflected laser powers are measured using photodiodes as shown in figure 3.3. S_p is then used to convert the recorded signal during the measurement into near-field heat flux. Figure 3.3 shows an example of a power calibration.

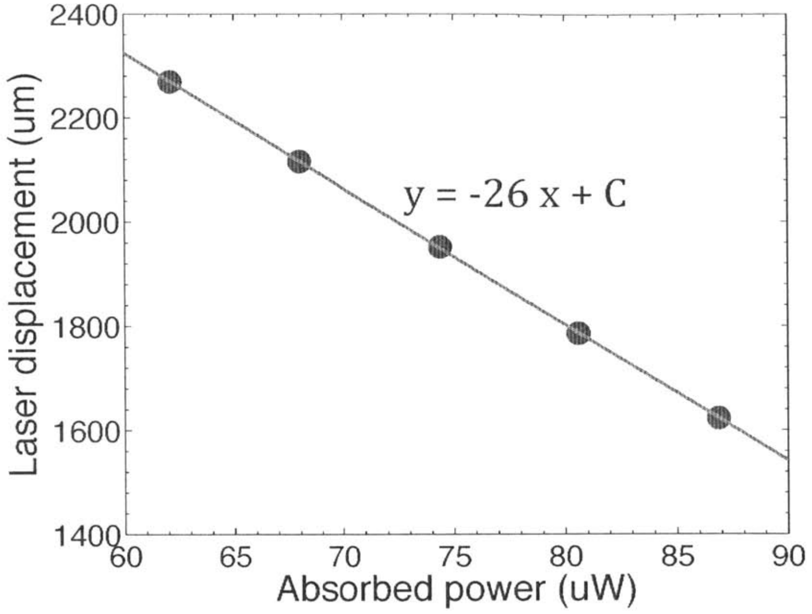

Figure 3.3 Laser displacement varies linearly as the absorbed power is varied as predicted by Eq. (3.8). This power calibration is used to convert the bending of the cantilever into near-field heat flux from the sphere to the substrate.

3.2.2 Base Temperature Calibration

Following the same mathematical procedure as previously, the sensitivity of the displacement of the reflected beam on the PSD to the base temperature is

$$S_T = \frac{\partial(\Delta d)}{\partial T_b} = -12sHl \qquad (3.9)$$

This calibration is carried out by measuring the displacement of the reflected laser beam on the position detector in response to the temperature variation of the cantilever base under vacuum. To actively vary the temperature of the base, a heater is attached below the cantilever (Figure 3.4), while a thermocouple is attached on the chip of the cantilever to measure the base temperature. Figure 3.5 shows an example of a base temperature calibration.

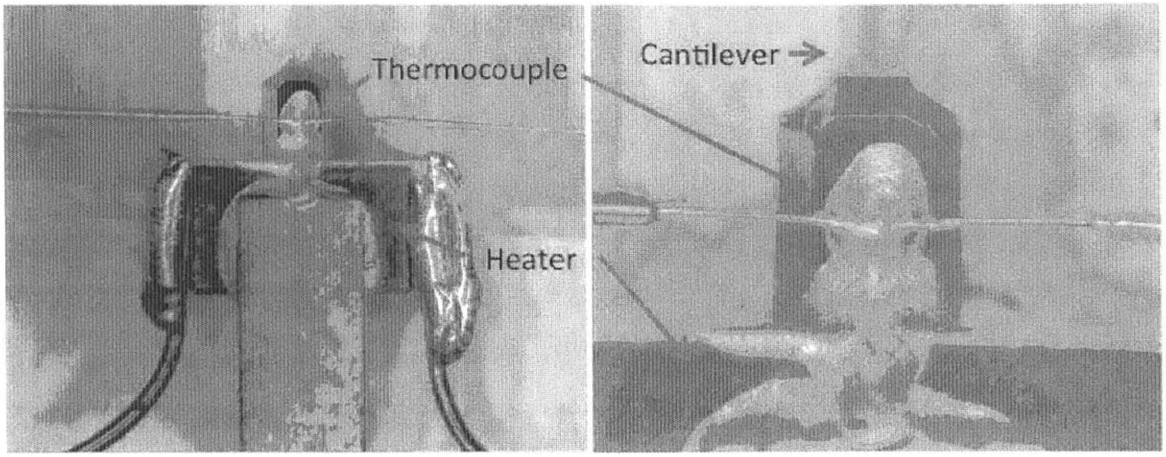

Figure 3.4 The bimaterial AFM cantilever is attached to a resistive heater using silver epoxy. The heater is used to heat up the base cantilever. A thermocouple is attached on the base of the cantilever to measure its temperature.

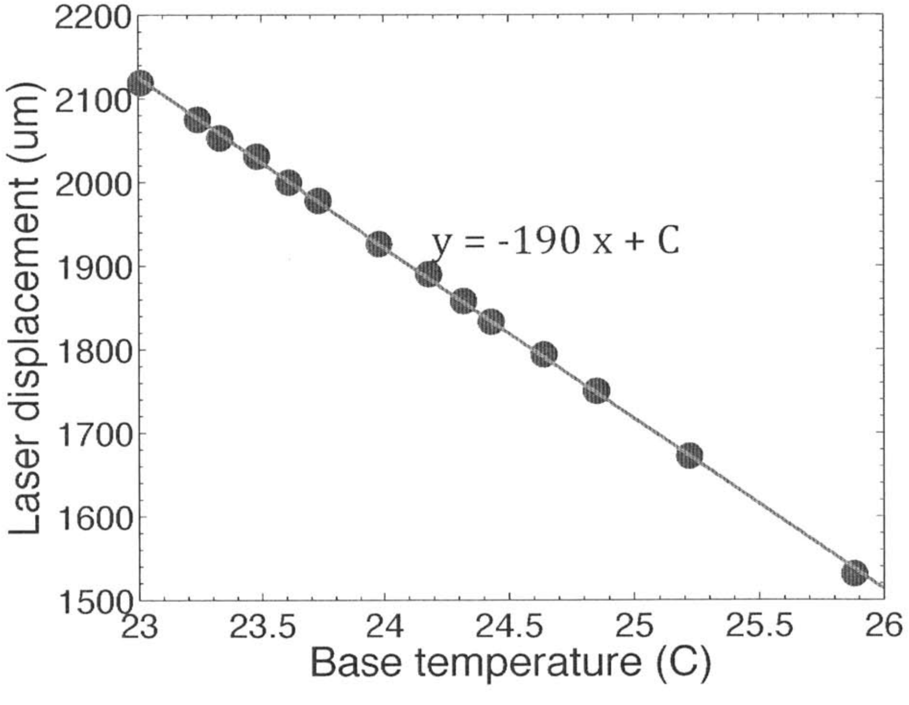

Figure 3.5 Laser displacement varies linearly as the base temperature is varied as predicted by Eq (3.9). This calibration is needed to experimentally determine the effective thermal conductance of the cantilever along with the absorbed power calibration (Eq. (3.10)). The effective thermal conductance of the cantilever is then used to determine the temperature difference between the sphere and the substrate (Eq. (3.11)).

3.2.3 Cantilever conductance

Using Eqs. (3.7) and (3.8), the effective thermal conductance of the cantilever is

$$G = \frac{S_T}{2S_P} \tag{3.10}$$

The temperature of the tip can be obtained using Eq. (3.2) with knowledge of the effective thermal conductance of the cantilever, and the laser power absorbed by the cantilever.

$$T_s = \frac{P}{G} + T_b \tag{3.11}$$

The temperature of the tip is then used to approximate the temperature of the sphere. COMSOL simulation shows that the temperature difference between the sphere and the surrounding is estimated to be 2 % lower than the temperature difference between the tip and the surrounding. Detail simulation is presented in Appendix A.

3.3 Improvements made on the experimental setup

A blue laser and a better combination of optical components are used to increase the accuracy of the absorbed power measurement, hence more accurate cantilever conductance. However, the improved setup cannot measure near-field thermal radiation with very small temperature difference, which is needed for the force measurement. The ratio of the reflectance to the absorptance of the blue laser (0.3/0.6 = 0.5) is much smaller than that of the red laser (0.9/0.1 = 9). This limits the smallest temperature difference between the sphere and the substrate that can be measured. To illustrate, lets consider the following condition. The cantilever conductance is ≈ 4 μW/K. The smallest allowable detected reflected power of the position detector is 10 μW. This means, for the blue laser, the absorbed power is 10 μW/0.5 = 20 μW, and the lowest temperature difference that we can measure is 20 μW/4 μW/K = 5 K. For the red laser the absorbed power is 10 μW/9 = 1.1 μW, and the lowest temperature difference that we can measure is 1.1 μW/4 μW/K = 0.25 K.

To solve this problem, the measurement is done in two steps. First, the near-field measurement and calibrations are done using the red laser setup (Figure 3.6). Second, the calibration is repeated with the blue laser setup (Figure 3.7). Then, the bending signal recorded with the red laser setup is then converted into near-field heat flux with the calibration factor obtained with the blue laser setup.

Figure 3.6 and 3.7 compare the red and the blue laser experimental setups. The optical components of the red laser experimental setup consist of the following. A red (λ = 635 nm) laser diode module (Lasermate LTG6354AH) is used as the laser source. The beam is reflected on a mirror to a convex lens (Thorlabs LA1608-A-ML) with 10 cm focal length to focus the laser beam on the cantilever. The size of the focused laser beam on the cantilever is 60 μm. The reflected portion of the laser power is directed onto a four-quadrant position-sensing detector (PSD), which is used to measure the displacement of the reflected beam and the reflected power.

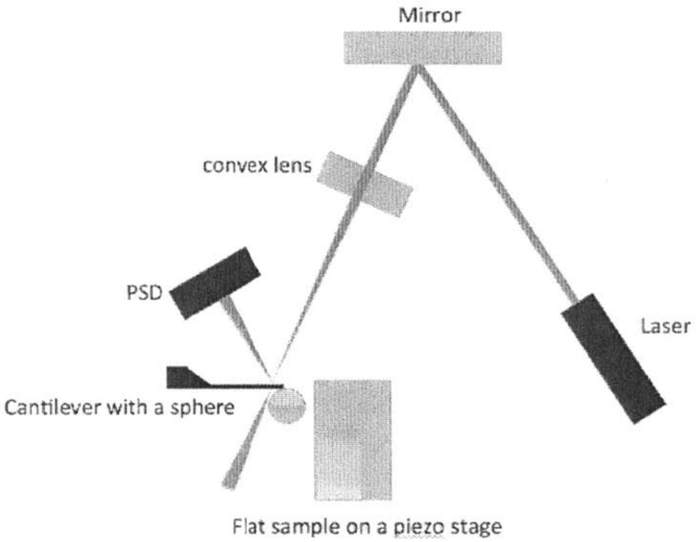

Figure 3.6 Schematic of the red laser experimental setup. The setup consists of a red (λ = 635 nm) laser diode module, a mirror to direct the laser beam onto the cantilever, a convex lens, the AFM cantilever with a microsphere attached on its tip, a substrate mounted on a piezoelectric motor and a position sensing detector (PSD). All of these components are mounted on a standard aluminum optical breadboard.

The optical components of the blue laser experimental setup consist of the following. A blue (λ = 444 nm) laser diode module (Thorlabs CPS 450) is used as the laser source. A polarizer (Thorlabs LPVISE100-A) mounted on a motorized rotational stage (Thorlabs PRM1Z8) is used to vary the laser power. A pair of concave lens (Thorlabs LC1715-A and LC4252-A) is used to diverge and collimate the beam. The collimated beam is reflected on a mirror to extend the optical path due to the space limitation of the vacuum chamber. An aspheric convex lens (Thorlabs AL2550-A) with 5 cm focal length is used to focus the laser beam. The beam splitter is used to split the beam. The reflected power from the beam splitter is measured with a photodiode (Newport 818-UV, 195 pW resolution). Since the ratio of the transmittance and reflectance of the beam splitter is measured, the transmitted beam through the beam splitter can be calculated. The transmitted beam through the beam splitter is the incident beam and hits the tip of the cantilever. The size of the focused laser beam on the cantilever is 30 μm. The reflected portion of the laser power is directed onto a four-quadrant position-sensing detector (PSD), which is used to measure the displacement of the reflected beam and the reflected power. A photodiode (Newport 818-UV) is positioned behind the cantilever to measure the transmitted laser beam.

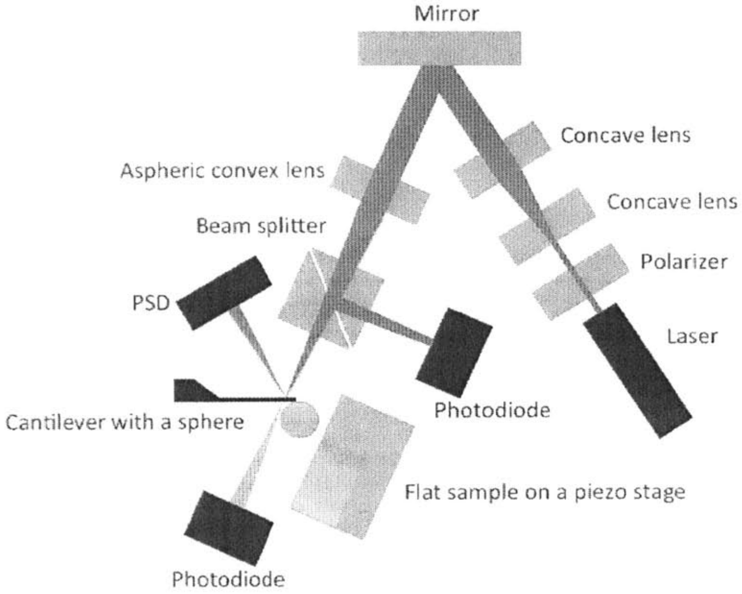

Figure 3.7 Schematic of the blue laser experimental setup. The setup consists of a blue (λ = 444 nm) laser diode module, a polarizer mounted on a rotating stage, a pair of concave lens as a beam expander and a mirror to direct the laser beam onto the cantilever, an aspheric convex lens, a beam splitter, the AFM cantilever with a microsphere attached on its tip, a substrate mounted on a piezoelectric motor, 2 photodiodes to measure the incoming and the transmitted laser beam and a position sensing detector (PSD). The optical configuration is optimized so the setup will fit into the vacuum chamber.

A commercial triangular silicon nitride AFM cantilever (Budgetsensor SiNi) is used as the bimaterial cantilever in our measurement setup. The cantilever is made of 450 ± 40 nm thick of SiN coated with 6 ± 4 nm Cr film and 65 ± 10 nm Au film. Its effective length is 200 μm. A schematic of the bi-material cantilever is presented in figure 3.8.

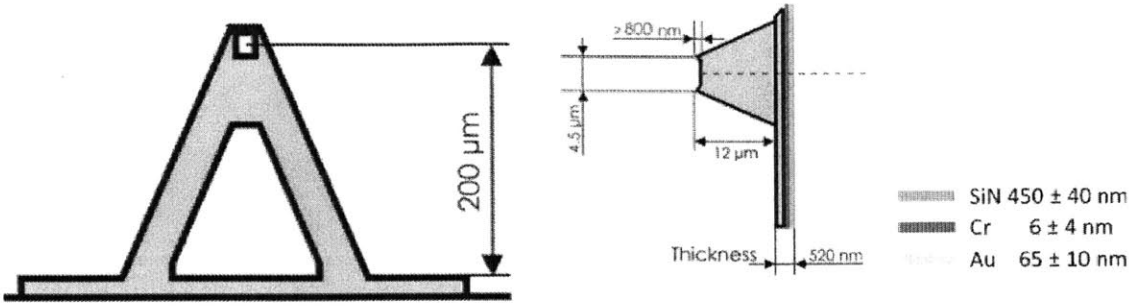

Figure 3.8 Budgetsensor SiNi cantilever is used as the bimaterial cantilever in the measurement setup. The triangular cantilever consists of multilayer structures of Au 450 ± 40 nm SiN, 6 ± 4 nm Cr, and 65 ± 10 nm [].

The measurement setup is placed inside a vacuum chamber and the measurement is done under vacuum conditions at 10^{-3} Pa to avoid any air conduction loss. The following subsections details the improvement made on the measurement setup.

3.3.1 Improved power measurement

The bimaterial based near-field thermal radiation measurement setup designed by Narayanaswamy et al. [62] utilizes a red laser. As explained previously in section 3.2.1, one of the steps in the measurement is the absorbed power measurement during the power calibration process. A key challenge in this process is the small absorption of the cantilever (9 % at 635 nm wavelength), since the absorbed power is determined by measuring the incident, transmitted, and reflected power. Narayanaswamy and Gu [129] improved the accuracy of the absorbed power measurement by minimizing the laser spot to just smaller than the width of the cantilever (40 µm). Gu et al. [3] improved the accuracy of the absorbed power measurement by orienting the incident beam perpendicular to the cantilever, hence minimizing the size of the incident beam.

In this subsection we present further improvement to increase the accuracy of the absorbed power measurement. We first present the absorbed power calibration procedure. Similar to Narayanaswamy et al. [129], a better combination of optical components is then used to focus the incident beam into a smaller spot to reduce the scattered light from the edge of the cantilever. Finally, the blue laser is used to replace the red laser to increase the absorptance. These improvements increase the accuracy of the absorbed power measurement, which is crucial to the cantilever calibration.

3.3.1.1 Absorbed power calibration procedure

The power calibration is done in two steps. The first step is to measure the absorbed power. The second step is to measure the bending of the cantilever as the absorbed power is varied. The difference between the red laser setup and the blue laser setup is in the way the absorbed power is measured.

In the red laser setup, the absorbed power is measured by the following steps. The first step is to measure the ratio between the absorptance and reflectance of the cantilever. The ratio between the absorptance and reflectance is defined as the ratio between the absorbed and the reflected power. This is obtained by measuring the incident, the transmitted and the reflected laser power using a photodiode (Newport 818-UV) and using the following equation

$$Absorbed = Incident - Transmitted - Reflected \qquad (3.12)$$

After the ratio of absorptance and reflectance is obtained, the measurement setup is placed in the vacuum chamber to avoid any convection and conduction losses. The next step is to record the bending of the cantilever in response to different laser power absorbed. The position detector (PSD) records the displacement of the reflected laser and the reflected power. By using the ratio between the absorptance and reflectance, the reflected power recorded by the PSD can be converted into absorbed power.

In the blue laser setup, power calibration process also consists of the same two steps. But, instead of using the ratio between the absorptance and the reflectance, we only use the absorptance. Using the knowledge of the beam splitter ratio, the incident power is determined by measuring the reflected power from the beam splitter. With the knowledge of the incident power and absorptance, the absorbed power can be determined.

The measurement of the absorbed power in the blue laser setup is more accurate than that of the red laser setup due to several reasons. In the red laser setup, the absorbed power is obtained by measuring the reflected power using the PSD. The PSD is actually designed to measure relative position accurately but it is not designed to measure absolute power due to separation between different active areas. Also, the position of the reflected laser spot on the PSD changes as the cantilever bends during the power calibration process. This could introduce an error due to the uniformity of the active are of the PSD. Most importantly, due to the size of the laser spot on the cantilever, and the bending of the cantilever during the calibration process, some of the reflected laser and/or the scattered light do not hit the active area of the PSD. On the other side, the absorbed power measurement in the blue laser setup does not suffer from those complications.red laserblue laser

3.3.1.2 A smaller focused laser spot and the use of a blue laser

Since it cannot be measured accurately, the scattered laser beam that is not specularly reflected from the cantilever is a source of error in determining the absorptance. Low absorptance values which results by using a red laser makes the error of the absorbed power larger. Although the scattered laser beam cannot be measured accurately, Shen et al. [77] attempted to estimate it by placing a photodiode in different places around the cantilever. Using this method, they estimated that the scattered laser beam to be around 2 %. Following their method, we measured a similar amount of scattered laser beam. However, the scattered laser beam around the direction of the specular reflection is difficult to quantify accurately.

$$Absorbed = \underbrace{Incident - Transmitted - Reflected}_{Measured} - \underbrace{Scattered}_{Estimated} \qquad (3.13)$$

The scattered light is mainly due to the reflection from the edge of the cantilever since the size of the laser beam is larger than the size of the cantilever tip (Figure 3.9).

To minimize the error coming from the inability to measure the scattered light accurately, the size of the laser spot needs to be minimized. Following the diffraction limit of a lens,

$$w = \frac{4\lambda f}{\pi d} \tag{3.14}$$

the size of the laser spot after focusing, *w*, can be minimized by reducing the wavelength, λ, of the laser, using a shorter focal length lens, *f*, and increase the input radius of the beam on the lens, *d*.

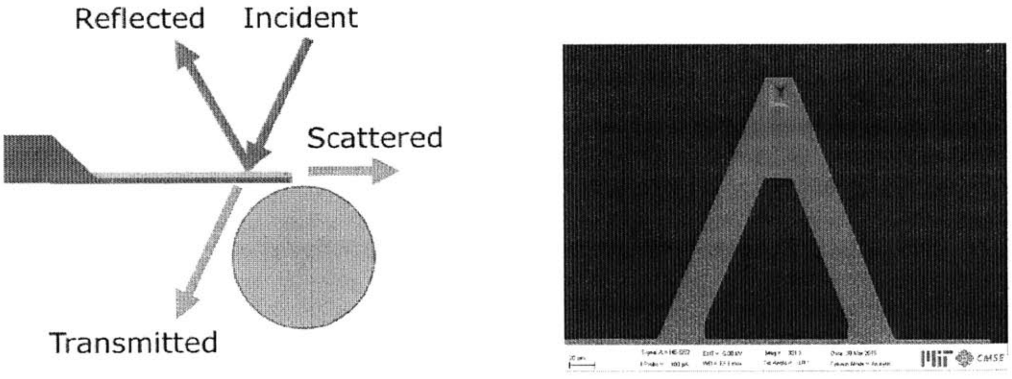

(a) (b)

Figure 3.9 (a). The absorbed power is determined by measuring the incident, transmitted, and reflected power. The scattered light is included as the absorbed power. (b). The scanning electron micrograph of the cantilever. The light is scattered from the edge of the cantilever because the laser spot is larger than the tip of the cantilever.

The improvement is realized by replacing a red laser (λ = 650 nm), which was previously used, with a blue laser (λ = 444 nm) to reduce the wavelength, replacing the previously used 10 cm focal length convex lens with a 5 cm focal length aspheric convex lens to reduce the focal length and improve the aberration, and expanding the beam before it is focused with a pair of concave lens to increase the radius of the incoming beam on the focusing lens. This improvement on the combination of the use of the optical components reduces the laser spot from 60 μm to 30 μm. This ensures that the entire laser beam is on the cantilever and minimizes the scattered light from the edge of the cantilever; hence minimizing the error measurement of the absorbed power.

The use of a blue laser also improves the setup significantly. Previously, a red laser (λ = 635 nm) was used as the laser source. However, due to low absorptance value at this wavelength, the incident and the reflected power of the cantilever measured are much larger than the absorbed power. The uncertainties of the incident and reflected power propagate to become large errors on the absorbed power. As previously explained, the sources of the error in the power measurement are mainly due to the unaccounted scattered light (Figure 3.6). Another source of uncertainty comes from the photodiode as listed in Table. 3.1.

Table 3.1 The source of the error in the power measurement.

	Uncertainty (%)
Non-uniformity of the silicon photodiode detector	±2
Power calibration of the silicon photodiode detector	±1
Linearity of the silicon photodiode detector	±0.5

To reduce the error, a blue laser (λ = 444 nm) is used to replace a red laser (λ = 635 nm). The cantilever has higher absorptance in the shorter wavelength as can be observed in figure 3.10. The measurement results of the absorptance, transmittance, and reflectance of the cantilever obtained by both blue (444 nm)and red (635 nm) lasers are also plotted.

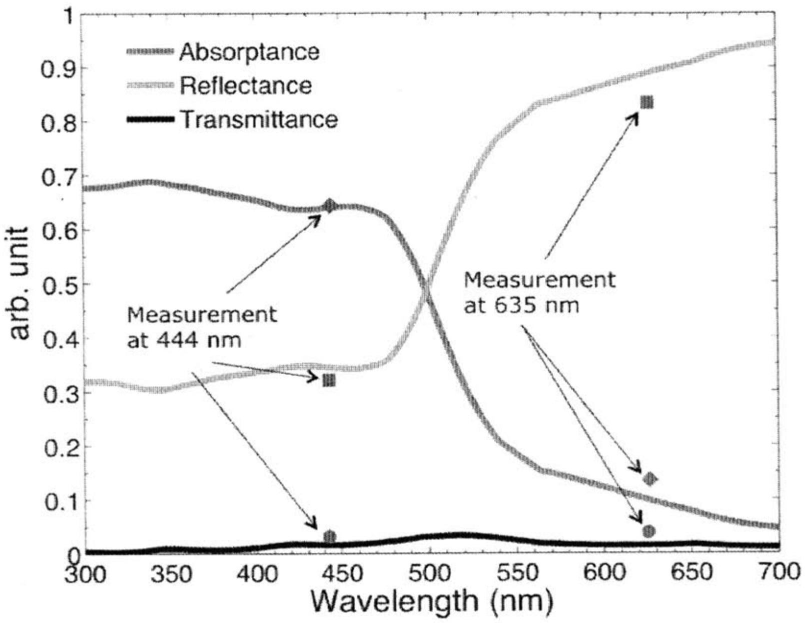

Figure 3.10 TM Spectral absorptance, reflectance, and transmittance at 30 degrees incident angle of 65nm Au 6nm Cr 450nm SiN (Budgetsensor). The measurement data of both blue (444 nm) and red (635 nm) lasers are also compared.

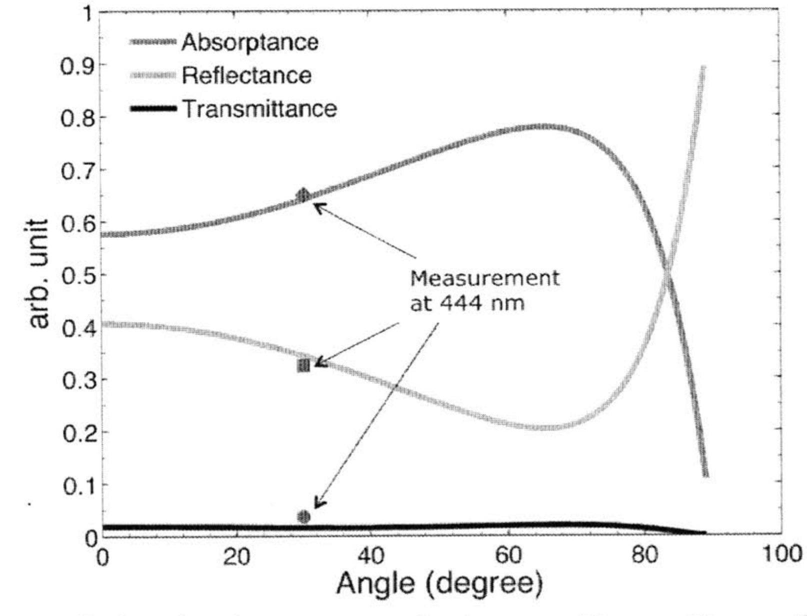

Figure 3.11 TM mode Angular absorptance, reflectance, and transmittance of 65nm Au 6nm Cr 450nm SiN (Budgetsensor) at 444nm wavelength. The measurement data of blue (444 nm) laser are also compared.

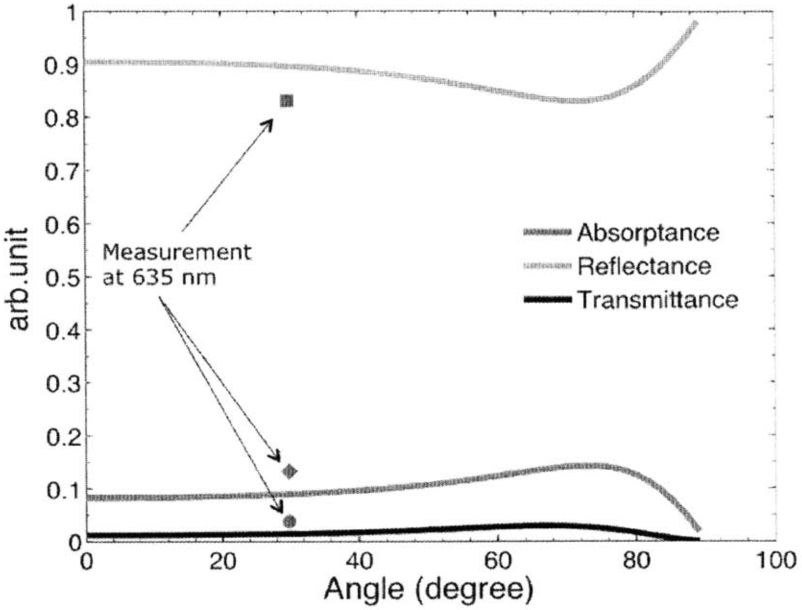

Figure 3.12 TM Angular absorptance, reflectance, and transmittance of 65nm Au 6nm Cr 450nm SiN (Budgetsensor) at 635nm wavelength. The measurement data of red (635 nm) laser are also compared.

As a comparison, Table 3.2 presents the theoretical prediction of the absorptance, transmittance, and reflectance of the cantilever for both 444 nm and 635 nm wavelengths. Significant increase in the absorptance reduces the absorbed power measurement error significantly. By increasing the absorptance, large error propagation due to subtracting two large numbers is avoided. Table 3.3 compares the measurement results of the absorptance, transmittance, and reflectance of the cantilever obtained by different lasers (444 and 635 nm).

Table 3.2 Comparison of theoretical prediction of absorptance, transmittance, and reflectance of the cantilever at 444 nm and 635 nm wavelengths.

	444nm	635 nm
Absorptance	0.64	0.09
Transmittance	0.02	0.01
Reflectance	0.34	0.9

Table 3.3 Comparison of the estimated total absorbed power measurement error.

	444 nm	635 nm
Transmittance	0.03	0.04
Reflectance	0.32	0.83
Scattered	0.03	0.02
Absorptance (without scattered beam correction)	0.65	0.13
Absorptance (without scattered beam correction)	0.62	0.11
Cantilever conductance (μW/K)	3.56	8.18

This inaccuracy on the absorptance measurement propagates into a systematic error on the power calibration factor, S_p. And in the end, this error propagates into the measured near-field heat flux, because the power calibration factor, S_p, is used to convert the bending of the cantilever into heat flux.

To see the variation of the thermal conductance of the cantilever, we calibrate 6 different cantilevers from two different boxes. The average thermal conductance is found to be 3.64 ± 0.4 μW/K. The error represents 95% confidence interval.

3.3.2 Force cancellation

The near-field thermal radiation measurement setup is different compared to traditional AFM or Casimir force measurements in the way that the cantilever is oriented relative to the substrate. In AFMs or Casimir force measurements the cantilever is oriented parallel to the substrate. Surface forces cause the cantilever to bend. In the original near-field thermal setup, the cantilever is oriented perpendicular to the substrate, minimizing these forces so that the bending of the cantilever will mostly be the result of thermal effects.

The setup is further improved to reduce the force effect so that the bending will be minimized. The cantilever is oriented with an angle relative to the substrate, such that the counter clockwise and clockwise moment cancels each other. Figure 3.12 shows the free body diagram of the cantilever-sphere-substrate system. The slope of the cantilever tip can be calculated by [130],

$$\left.\frac{dZ}{dx}\right|_{tip} = \frac{FL}{EI}(\cos\theta(Y + R\sin\theta) - \sin\theta(\frac{L}{2} + X + R\cos\theta)) \qquad (3.15)$$

F is force, *L* is length of the cantilever, *E* is elastic modulus, *I* is the moment of inertia, θ is angle between the cantilever and the substrate, *R* is radius of the microsphere, *X* and *Y* are the horizontal and vertical distance between the tip of the cantilever and the center of the sphere (Figure 3.13).

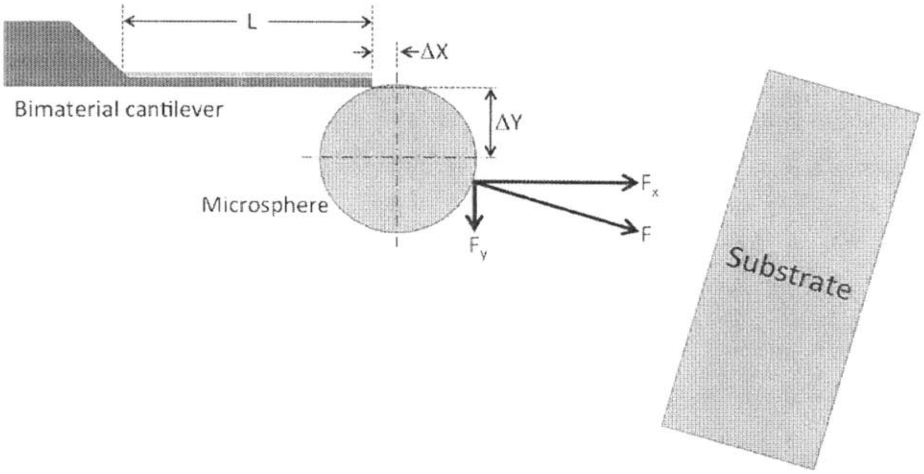

Figure 3.13 A free body diagram of the cantilever-sphere-substrate system shows the force effect can be minimized by orienting the substrate relative to the cantilever with a specific angle.

Following Eq. (3.15), the change of the slope of the cantilever tip due to force between the sphere and the substrate can be made zero by making the angle between the cantilever and the sphere such that

$$\cos\theta(Y + R\sin\theta) = \sin\theta(\frac{L}{2} + X + R\cos\theta) \tag{3.16}$$

Figure 3.14 shows a typical sphere-cantilever system. Following Eq. (3.17), the change of the slope of the cantilever tip due to force between the sphere and the substrate can be minimized by orienting the substrate relative to the cantilever with a 26^0 angle.

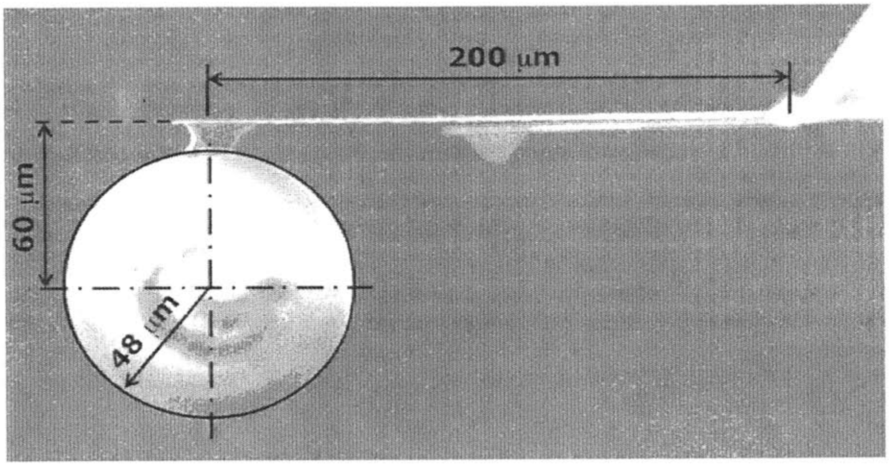

Figure 3.14 An example of a sphere-cantilever system. To minimize the force effect, the cantilever is oriented with an angle of 26^0 relative to the substrate.

In practice, charge distribution on the surface of the sphere and/or the substrate is not known. As a consequence, the location and the direction where the force is exerted might not be on the center as depicted in Fig. 3.13. An iterative process is done to minimize the force. Different angles of orientation are tried until the force effect is minimized.

After the force effect is minimized, force signal can be completely extracted from the heat transfer signal by performing measurement at very low temperature difference. The laser power absorbed by the cantilever is reduced as low as possible, such that the temperature difference between the sphere and the substrate is very small (<1K).

3.5 Summary

The red laser bimaterial based near-field thermal radiation suffers from inaccurate absorptance measurement. In this chapter, we explain the source of the error in the absorptance measurement. We improve the measurement setup by using a better method in measuring the absorbed power, a smaller laser spot, a blue laser, and an orientation angle to reduce the force effect.

Chapter 4

Measurement of near-field thermal radiation between silica surfaces

To measure near-field thermal radiation is a challenging task. For a long time researchers have tried to make two parallel plates separated by nanometer gaps. It was Narayanaswamy et al. [62] who creatively solved the problem by replacing one plate with a sphere to eliminate the parallelism problem. Using a bi-material cantilever, they measured near-field thermal radiation between a sphere and a plate. Later on, Shen et al. [2] continued the work, and showed the enhancement of the radiative transfer due to the near-field effect. Their work was a breakthrough in the field of near-field thermal radiation. However, as explained in chapter 3, power calibration suffers from large systematic error due to inaccuracy in the absorptance measurement. This power calibration is used to convert the bending of the cantilever into heat flux. Hence, the measurement results suffer from large systematic error.

This chapter repeats the measurement of near-field thermal radiation between a silica microsphere and a glass substrate. The error propagation of power calibration is shown as the comparison of the uncorrected and the corrected data. The corrected data are then analyzed to give a better understanding of the limitations of the measurement setup and procedures.

The second part of this chapter presents the measurement of near-field thermal radiation between two silica microspheres. Our bimaterial based near-field thermal radiation experimental setup is limited in a way that it can only measure near-field thermal radiation involving a spherical surface. As pointed out before, a microsphere is used to eliminate the parallelism problem. While usually this setup is only used to measure near-field thermal radiation between a sphere and a plate, here we show that it can also be used to measure near-field thermal radiation between two microspheres. This extends the experimental capability to measure a geometry and configuration other than sphere-plate.

4.1 Measurement of near-field thermal radiation between a silica sphere and a glass substrate

Figure 3.1a shows a schematic of the measurement system. A silica microsphere is attached to a bimaterial cantilever and the glass substrate is attached on a piezostage. The silica microsphere is obtained from Microsphere-Nanosphere. The plate is a microscope glass substrate from VWR soda-lime glass in accordance with ISO 8037/1 standards. These samples are chosen to follow the experiment by Shen et al [2].

4.1.1 Microspheres cleaning process

Figure 4.1 shows the SEM images of the silica microspheres obtained from Microsphere-Nanosphere. Contaminants are found on the surface of the sphere. To remove these contaminants, the spheres need to be cleaned. The cleaning process starts by cleaning all the glassware used in the process such as vials, pipettes, and microscope glass slides with piranha solution. All the glass wares are then rinsed with DI water. The spheres are then dispersed in acetone in a clean vial and followed by ultrasonication process for 1 hour. The process is followed by dispersing the spheres in methanol and another ultrasonication process for 1 hour. Finally, the spheres are dispersed in Isopropanol and followed by another ultrasonication process for 1 hour. The result of the cleaning process is shown in figure 4.2. The majority of contaminants are gone. However, the spheres still suffer from the particulates in the solutions. These particulates are left on the surface of the sphere while the Acetone/Methanol/Isopropanol evaporates. Later, we will explain how these particulates influence the measurement. In the future, a better cleaning process needs to be employed to remove these particulates.

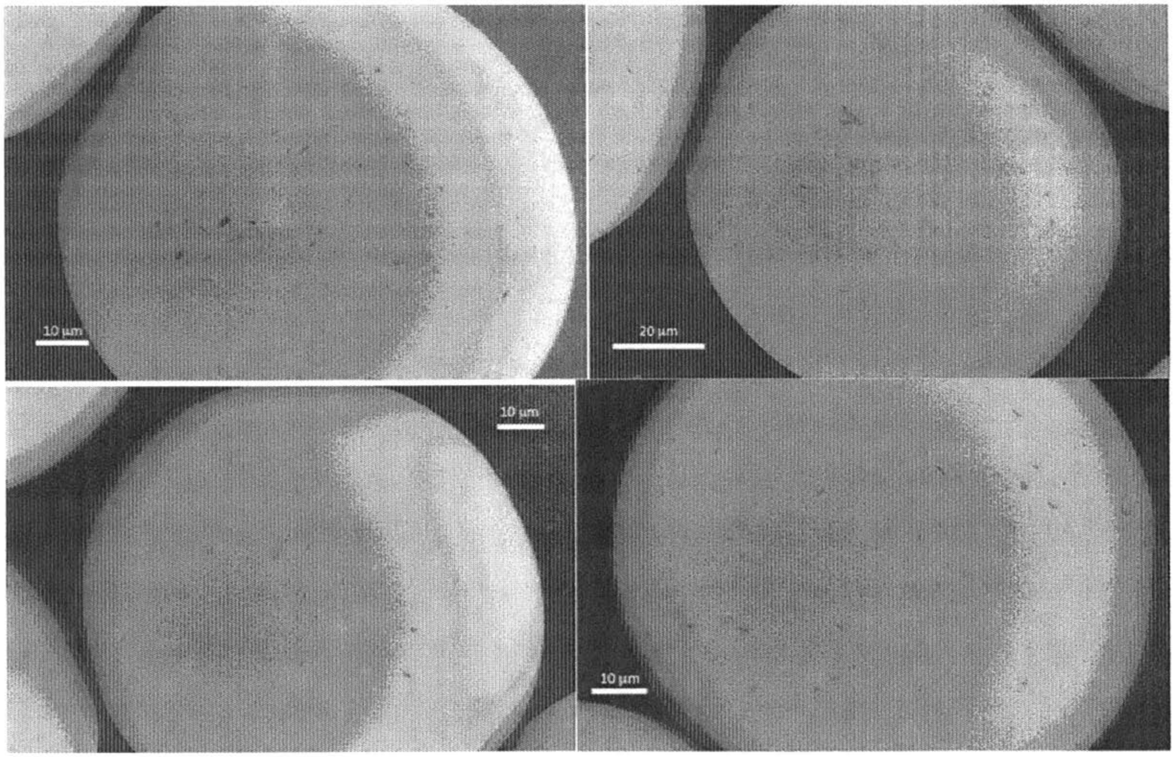

Figure 4.1 SEM images of microspheres obtained from Microsphere-Nanosphere reveals contaminants on the surface.

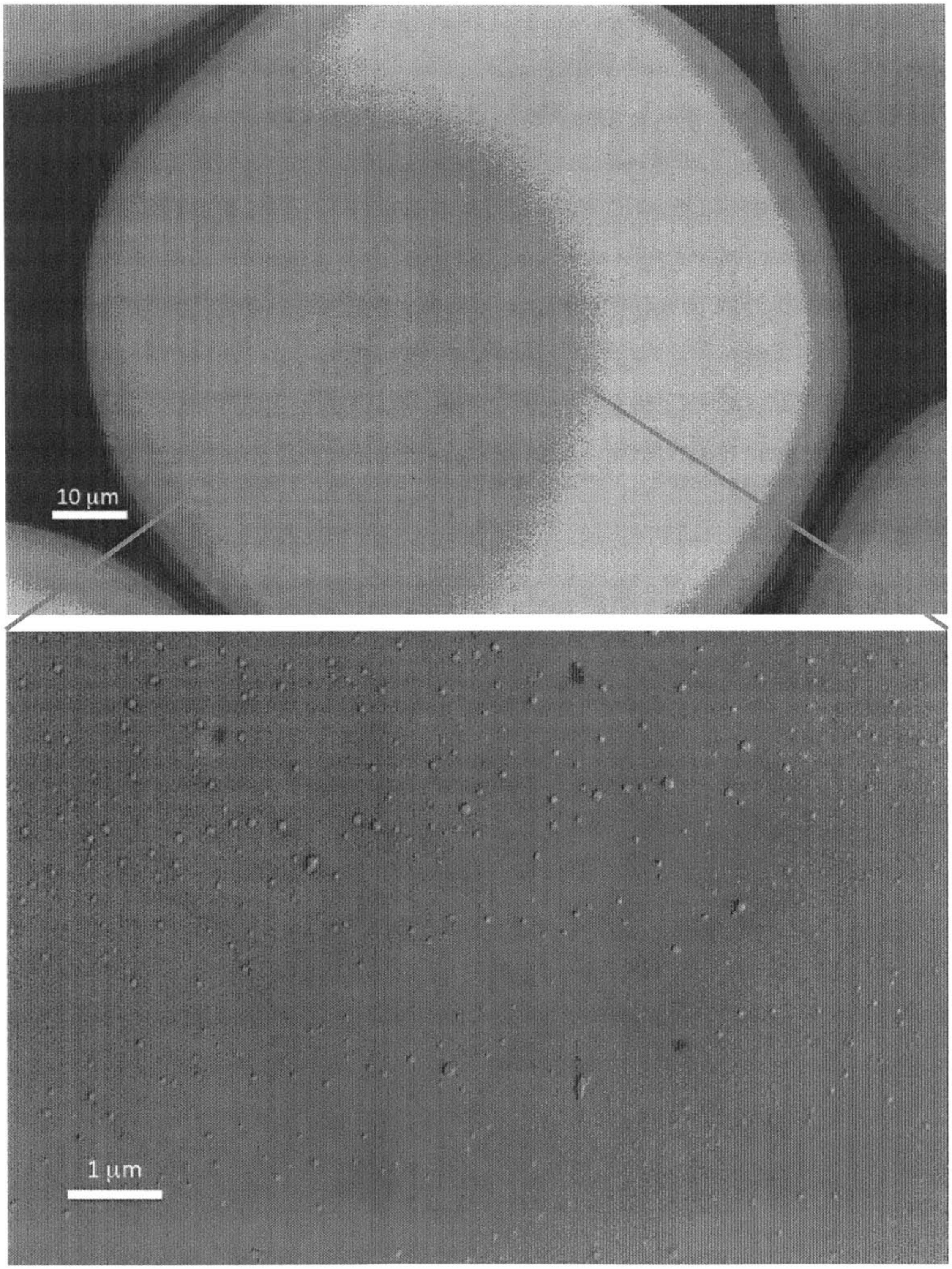

Figure 4.2 (a) The microspheres are cleaned by ultrasonication process in Acetone-Methanol-Isopropanol solution. This process succeeds to clean the majority of the contaminant. (b) High resolution SEM image reveals the existence of particulates.

4.1.2 Near-field thermal radiative conductance between a silica sphere and a glass substrate

This section only presents the measurement results. The experimental setup and procedure can be found in chapter 3. Figure 4.3 shows typical raw data of the measurement. The measurement is started as the separation gap between the sphere and the substrate is 10 μm apart. As the separation distance between the silica sphere and the glass substrate is reduced, the radiative heat transfer increases, indicated by the movement of the laser spot on the position sensing detector (PSD). Contact between the sphere and the substrate is made when the PSD signal changes abruptly. The sharp change in the signal indicates that the cantilever does not bend continuously due to thermal effects, but because of the contact force between the sphere and the substrate.

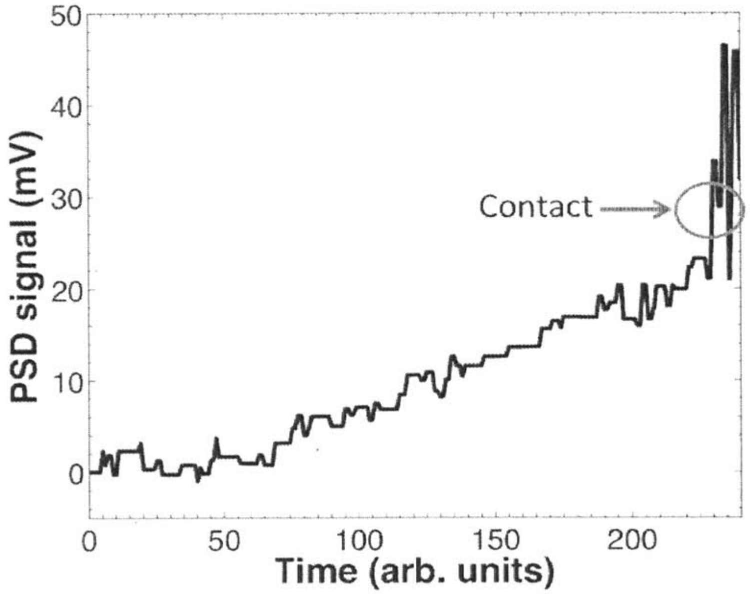

Figure 4.3 The bending of the cantilever is translated into displacement of the laser spot on the PSD and recorded as the separation distance between the sphere and the plate is reduced. Contact is established when the PSD signal changes abruptly. The sharp change in the signal indicates that the cantilever does not bend continuously due to thermal effects, but instead due to the contact force between the sphere and the substrate. This contact

point is the reference point for zero separation distance between the sphere and the substrate.

Contact point is the reference point for zero separation distance between the sphere and the substrate. This contact point has an important implication on interpreting the measurement result as explained later. This raw data is then processed by relating the recorded separation gaps with the zero reference point and converted into near-field radiative heat flux.

To account for the statistical variation due to thermal fluctuation, the experiments are repeated 10 times. The recorded data are averaged and then converted into the near-field radiative heat flux by using power calibration, S_P.

As explained in chapter 3, the measurement is done using red laser. The power calibration obtained from the red laser setup is 32 mV/μW. The temperature calibration is 500 mV/K. From these two calibrations, using Eq. (3.10), the cantilever conductance is found to be 8.2 μW/K. The calibration is then repeated using a blue laser and the conductance is found to be 3.6 μW/K. As we previously explained, we know that the large difference of the thermal conductance of the cantilever obtained from both calibrations is due to the error in the absorbed power measurement. To obtain more accurate power calibration for the red laser, we use the cantilever conductance obtained from blue laser calibration, 3.6 μW/K and the temperature calibration using red laser, 500mV/K. Using Eq. (3.10) we obtain the corrected power calibration of the red laser to be 72 mV/μW. This corrected power calibration is higher than that obtained using red laser by a factor of 2.25.

Figure 4.4 presents the near-field heat flux as a function of separation distance. It compares the uncorrected near-field heat flux obtained using the red laser power calibration (red circles) and the corrected near-field heat flux obtained using the blue laser power calibration (blue squares). The theoretical prediction is also plotted as a comparison. The error bar represents 95% confidence interval of 10 runs . The uncorrected near-field heat flux is higher than corrected data by a factor of 2.25. The large difference between those two sets of data shows the systematic error suffered from the power calibration.

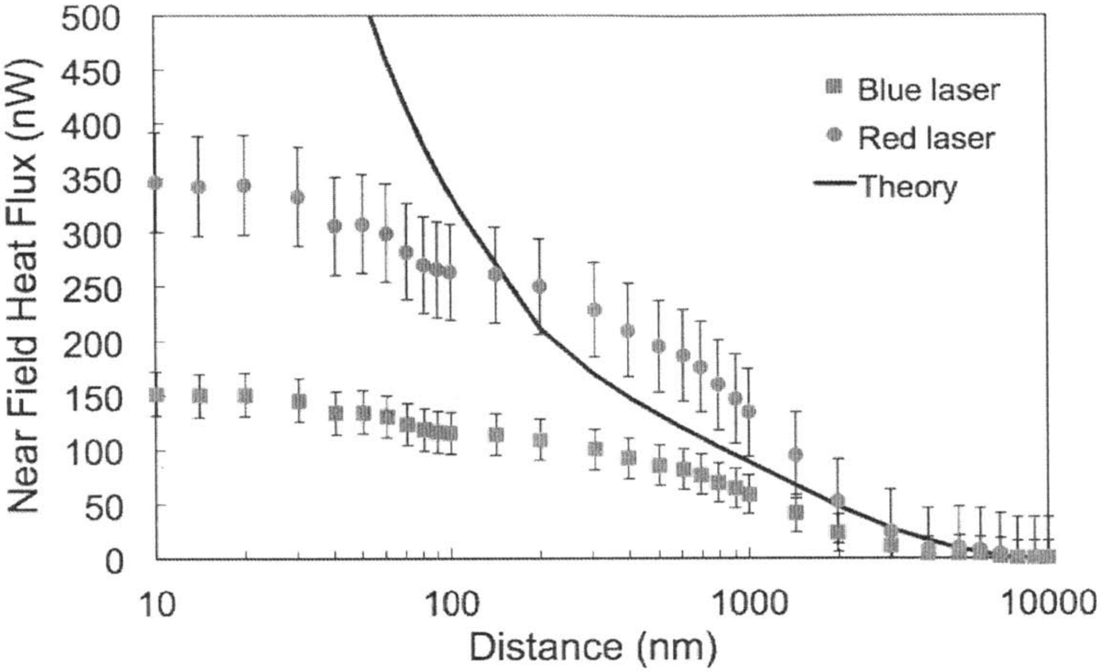

Figure 4.4 The displacement of the laser spot on the PSD is converted into near-field heat flux using the power calibration factor. The near-field heat flux obtained using red laser power calibration (red circles) is higher than that using the blue laser corrected power calibration (blue squares) by a factor of 2.25. The error bar represents 95% confidence interval.

Since the thermal conductance of the cantilever is known, the temperature of the sphere can be determined using Eq. (3.11) by dividing the absorbed power with the cantilever conductance. The temperature of the substrate is measured using a thermocouple. The near-field radiative conductance can then be obtained by dividing the near-field radiative heat transfer by the temperature difference between the sphere and the substrate, which happens to be 24.5 K. Figure 4.5 presents the near-field thermal radiative conductance as a function of separation distance. The uncorrected data (red circles) are compared with the corrected data (blue squares). The theoretical prediction is also plotted as a comparison. The error bar represents 95% confidence interval. The same with the heat flux, the uncorrected data is higher than the corrected data by a factor of 2.25 (Figure 4.5).

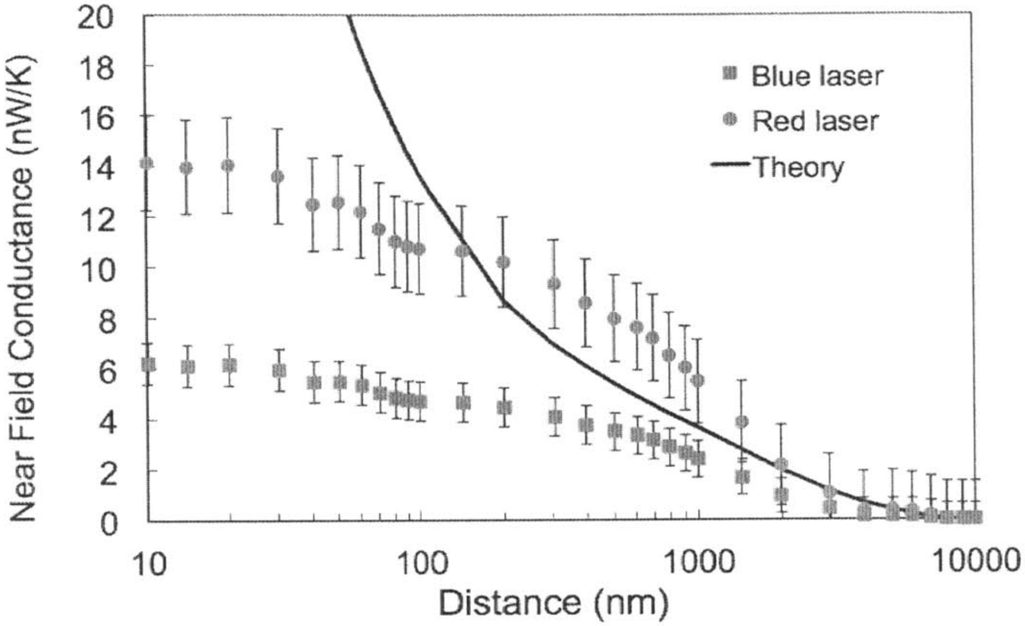

Figure 4.5 The heat flux is then converted into radiative conductance by dividing the heat flux with temperature difference, 24.5K. Both cases are compared with the theoretical prediction. The uncorrected data is higher than the corrected data by a factor of 2.25. The error bar represents 95% confidence interval.

Figure 4.6 presents 9 different measurement results previously taken with the red laser setup. Each set of data is average of 10 runs. The radius of the sphere used in each measurement varies slightly. The average radius is 48.3 μm. Since near-field thermal radiative conductance is proportional to the radius of the sphere (Eq.2.22), to account for this variation, all measurement results have been rescaled with a factor of 48.3/radius. Hence, all the measurement results presented in figure 4.6 are scaled to have a radius of 48.3 μm. The cantilever conductance, *G*, of each measurement is also presented on figure 4.6. Large variation is suspected as a result of the inaccuracy in measuring the absorbed power.

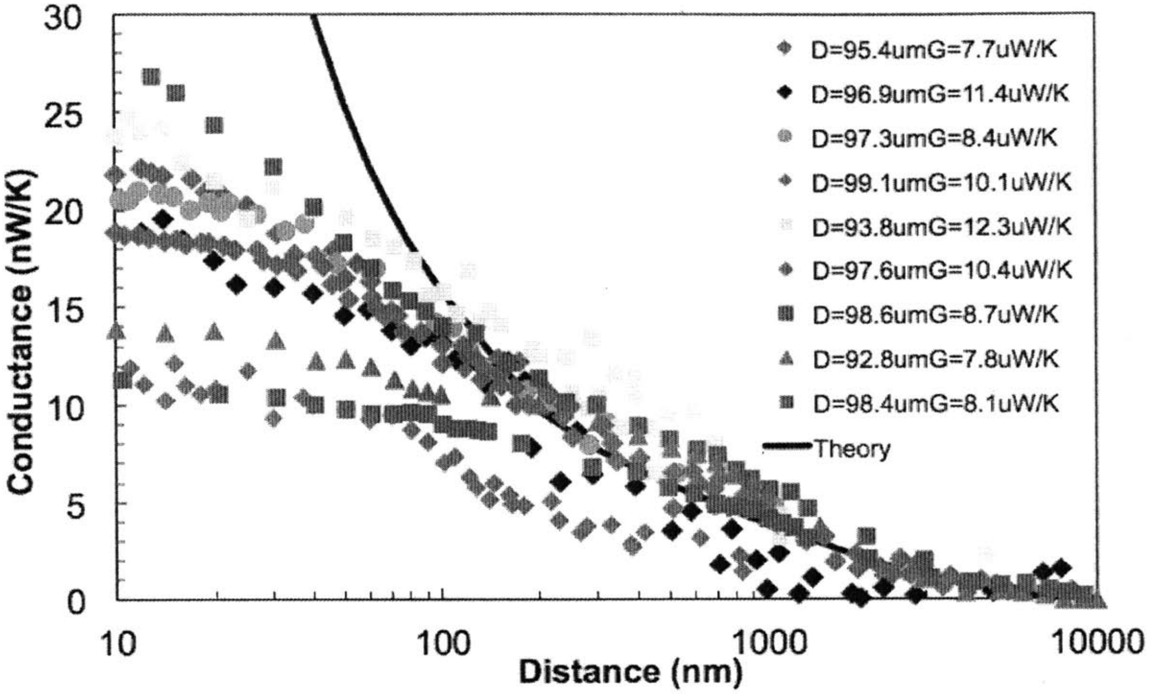

Figure 4.6 Near-field thermal radiative conductance between a silica sphere with different radius and a glass substrate. The thermal conductance of the cantilever varies significantly due to the inaccuracy in measuring the absorbed power.

The same correction procedure, as we explained earlier, was done to all previous measurement results. The correction is done by assuming that the cantilever conductance is 3.6 ± 0.4 μW/K. This value is an average of six different cantilevers calibrated using the blue laser setup. Figure 4.7 presents the corrected near-field thermal radiative conductance. All measurement results have been corrected with a factor of $3.6/G$. The corrected results are consistently lower than the uncorrected results due to the inaccuracy in the absorbed power measurement.

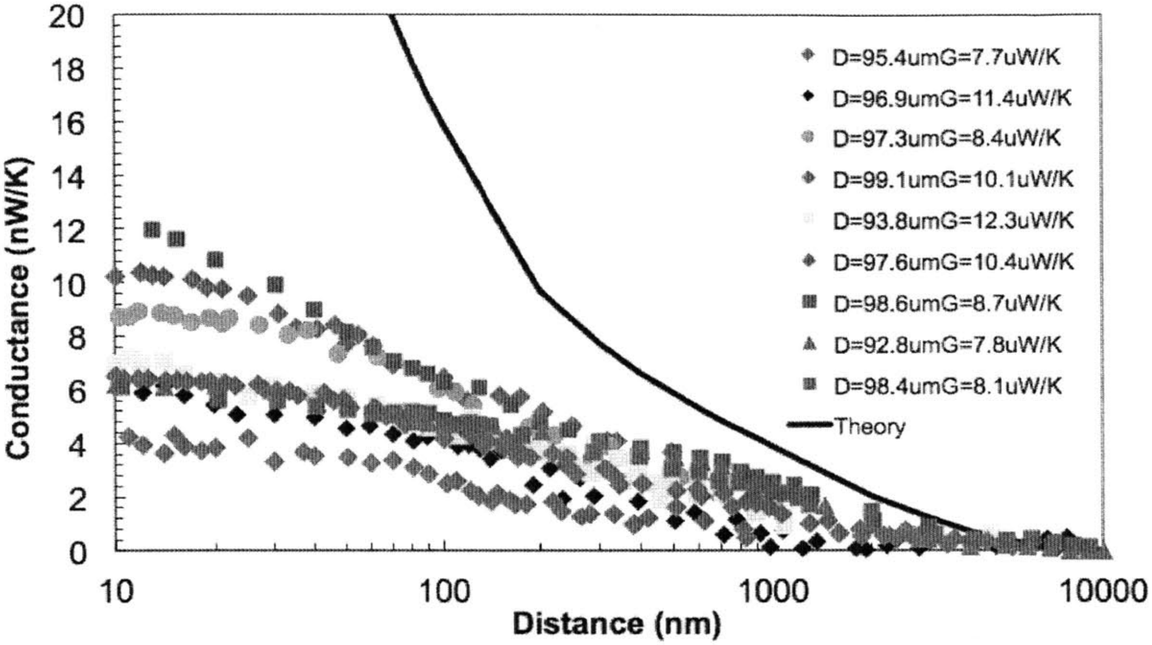

Figure 4.7 Measurement results are corrected by assuming that the cantilever conductance is 3.6 μW/K. All measurement results have been corrected with a factor of $3.6/G$.

Different measurement results in figure 4.7 are then averaged and compared with the existing near-field thermal radiation between silica surfaces measurement results. Shen et al. [2] measured near-field thermal radiation between a silica sphere (radius = 50 μm) a glass substrate. Shen et al. data are presented as black squares. Gu et al. [3] measured near-field thermal radiation between a silica sphere (radius = 25 μm) and a glass substrate. Gu et al. data are presented as green triangles. Song et al. [4] measured near-field thermal radiation between a silica sphere (radius = 26.5 μm) and a 3 um silicon dioxide layer deposited on a 100 nm-thick gold film. Song et al. data are presented as red diamonds. Our measurement data are presented as blue circles. To account for radius variation, all measurement results have been rescaled with a factor of 48.3/radius. Figure 4.8 compares all the measurement results as well as prediction from theory. Our experimental data are closer to that of Song et al. at larger separations, but deviate at smaller separations.

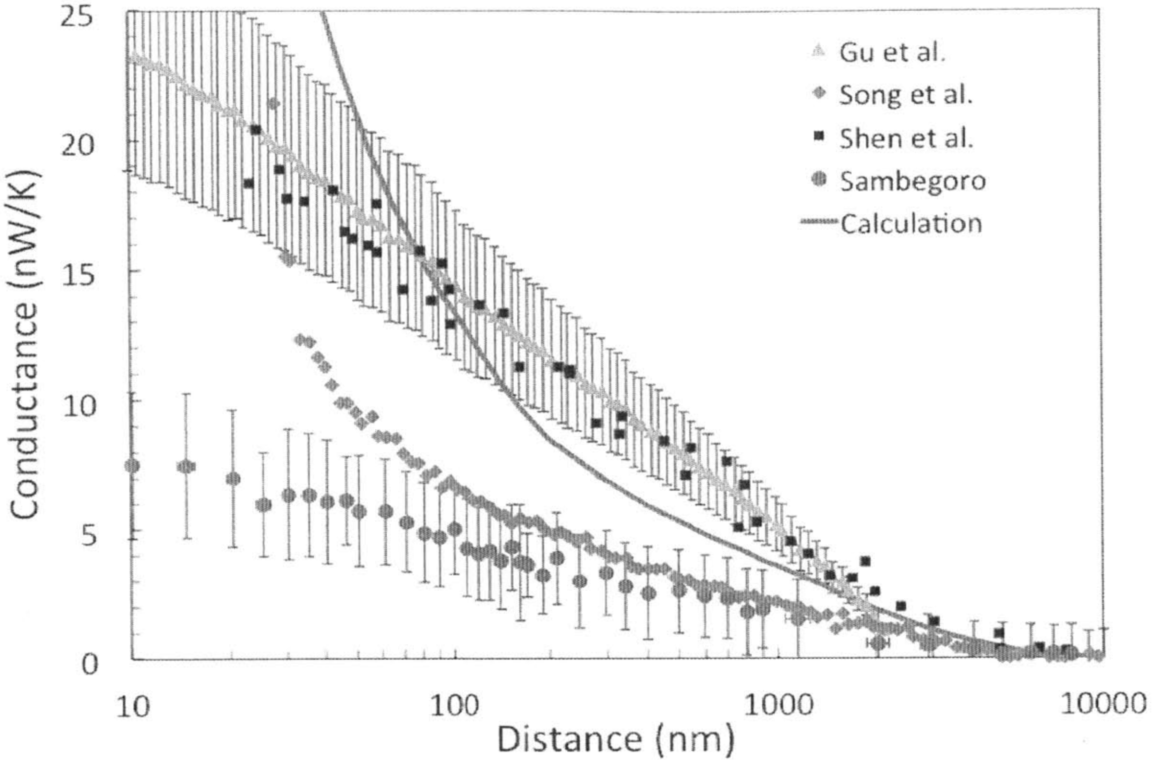

Figure 4.8 Comparison of different measurement results of near-field thermal radiation between a silica sphere and a glass substrate/silica layer. Shen et al. [2] measured near-field thermal radiation between a silica sphere (radius = 50 μm) a glass substrate (black squares). Gu et al. [3] measured near-field thermal radiation between a silica sphere (radius = 25 μm) and a glass substrate (green triangles). Song et al. [4] measured near-field thermal radiation between a silica sphere (radius = 26.5 μm) and a 3 um silicon dioxide layer deposited on a 100 nm-thick gold film (red diamonds). The average of 9 different measurements presented in figure 4.7 is presented as blue circles. To account for radius variation, all measurement results have been rescaled with a factor of 48.3/radius (Eq.2.22).

4.1.3 The influence of particulates on the separation gaps

As can be seen in figure 4.7 and 4.8, our measurement results deviate from the theoretical prediction. This deviation from the theoretical prediction is most likely due to the existence of particulates on the surface of the sphere as can be seen on the SEM image (Figure 4.9). The SEM image reveals the size of particulates in the order of ≈ 100s nm.

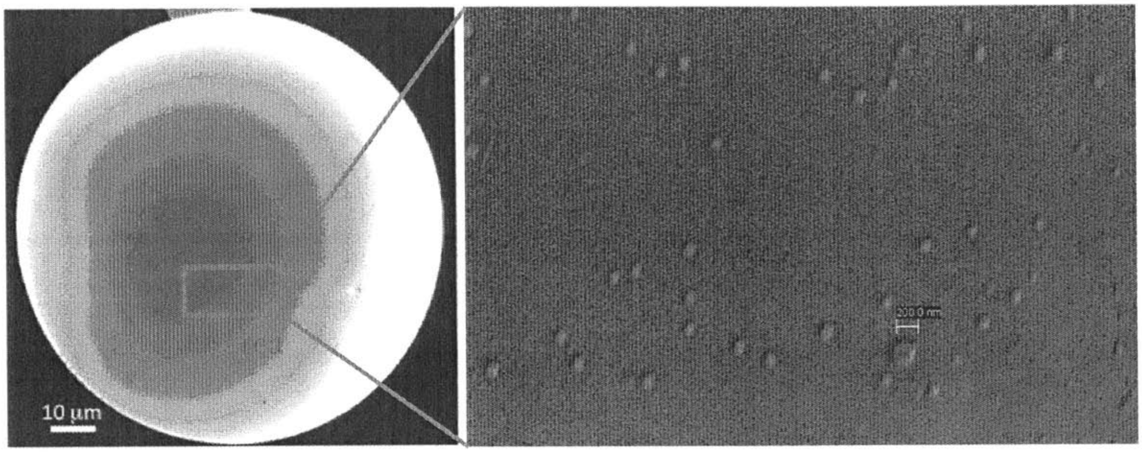

Figure 4.9 The scanning electron micrograph of the contact area shows particulates on the surface of the sphere in the order of 100s nm. These particulates cause an error on the determination of the separation distance between the sphere and the plate.

As we explain earlier, the distance between the sphere and the plate is measured relative to the contact point, which acts as the reference point for zero separation distance between the sphere and the plate. This contact point is between the closest peaks of the two surfaces. The definition of the zero reference point has important implications in the interpretation of the measurement results. If there is a particulate on the surface, instead of having a contact point between the peak of the sphere and the plate, this zero reference point is between these particulates. Figure 4.10 illustrates two conditions comparing the case of clean and dirty surfaces. In the case of the clean surface, the separation distance is the actual distance between the sphere and the plate. In the case of the dirty surface, the separation distance is the distance between these particulates.

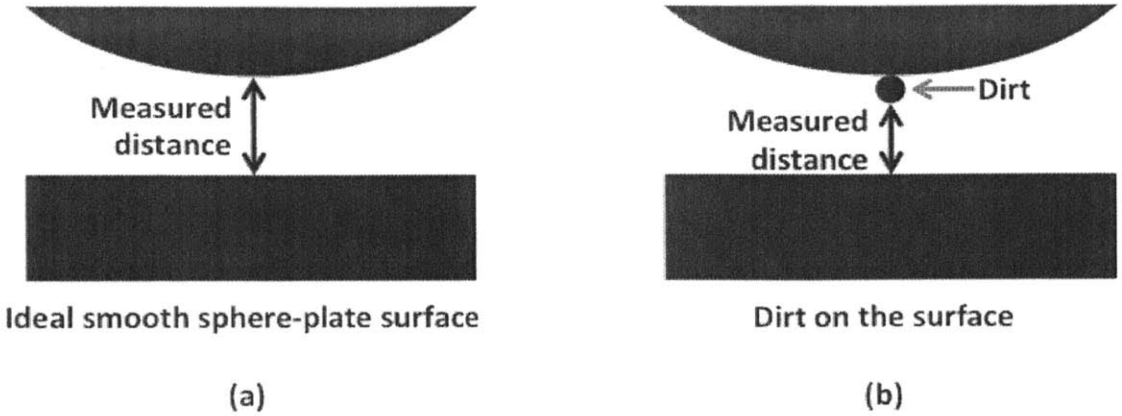

Figure 4.10 The schematic of contact between (a) perfectly clean sphere-plate (b) a particulate on the surface sphere-smooth plate illustrates the definition of contact point. The existence of particulates on the surface cause an error on the determination of the separation distance between the sphere and the plate.

4.1.4 Spatial distribution of near-field heat flux between a sphere and a plate

The existence of particulates on the surface might also screen or alter the electromagnetic field. This inspires us to analyze the contribution of a particular area of the sphere on the total near-field heat transfer between a sphere and a plate. Since it is hard to keep the entire surface of the sphere clean, this analysis helps to determine the size of the surface area of the sphere that needs to be clean.

Using the proximity approximation (PA), as previously explained in chapter 2, the curved surface is approximated by differential flat areas, as shown in figure 4.11.

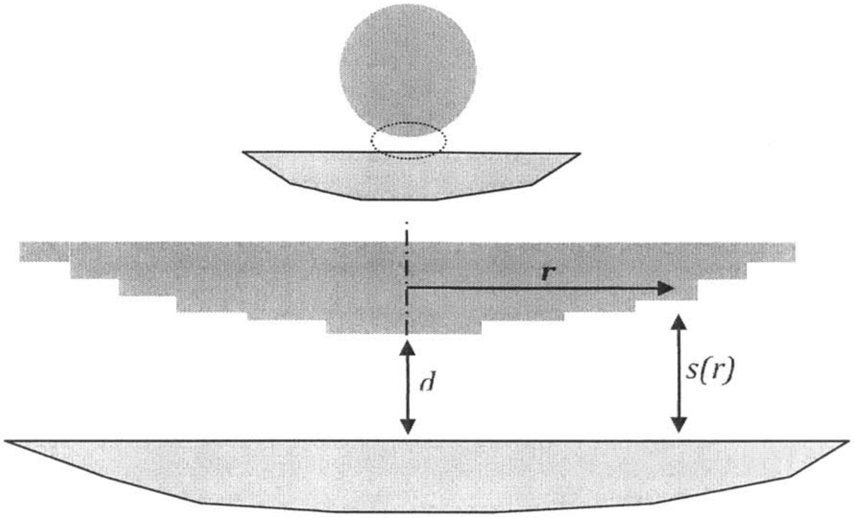

Figure 4.11 Proximity force theorem approximates the curved surface of the microsphere by differential flat surfaces.

Heat flux from individual annulus can be written as

$$q'(r) = h_{near-field}^{plate-plate}\left(s(r)\right)2\pi r \qquad (4.1)$$

q' is the heat flux. $s = d + R - \sqrt{R^2 - r^2}$ is the separation distance of between each differential plate and the substrate. d is the separation distance between the sphere and the substrate, R is the radius of the sphere, h is the near-field radiative heat transfer coefficient between two parallel plates.

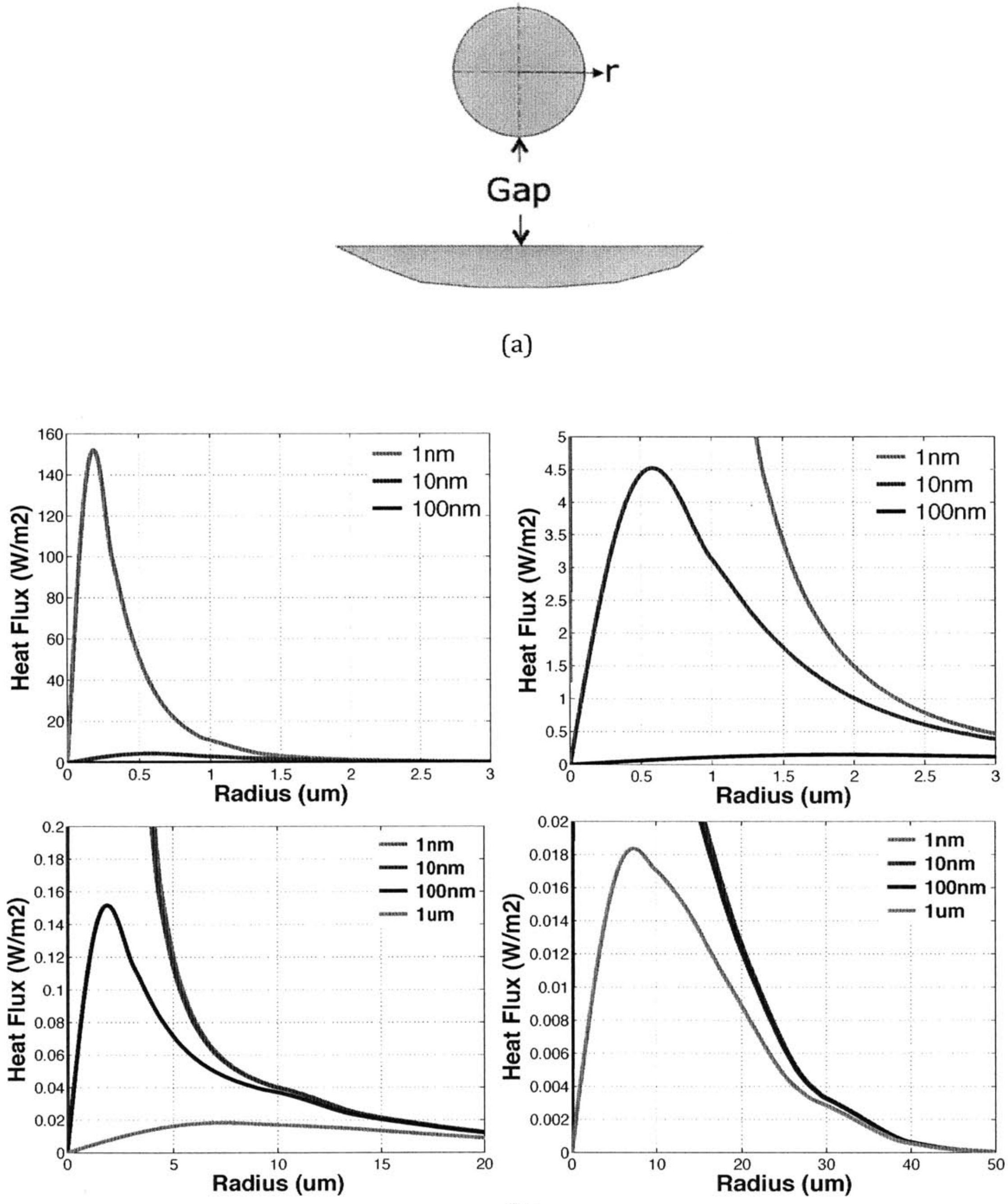

(a)

(b)

Figure 4.12 (a). An illustration of the radius of the projected area of the sphere. (b-e). Near-field heat flux contribution as a function of radius of the projected area for different separation gaps between the sphere and the plate. (b). Gap = 1 nm. (c). Gap = 10 nm. (d). Gap = 100 nm. (e). Gap = 1 μm.

Figure 4.12 (b-e) presents the theoretical calculation of the heat flux as a function of radius of the projected area of the surface of the sphere based on Eq. (4.1). The heat flux shows non-monotonic behavior as a function of the radius of the projected area. This is due to the opposite trend of the radius and the near-field transfers as the radius becomes larger. Although near-field heat transfer per unit area is largest around the center of the sphere, when the separation gap is small, this area is only a small portion of the total area of the sphere. As a consequence, heat transfer from that particular area is small. The maximum transfer happens due to the combination of high enough near-field transfer and large enough area. The radius of the projected area where this maximum transfer occurs also changes as a function of separation distance between the sphere and the substrate as shown in figure 4.12 (b-e).

By integrating Eq (4.1), the normalized accumulated heat flux as a function of the projected radius can be obtained as shown in figure 4.13. This shows the portion of the heat flux transferred from a particular area, where the radius of the projected area is *r*. As an illustration, figure 4.13 shows the area of the sphere, which transfers 90% of the energy. Of experimental relevance, for separation distance is smaller than 1 μm, most of the heat is transferred from the area with 20 μm projected radius. This area needs extra care in the measurement in order to better compare the measurement with the theoretical prediction. These results will guide the preparation process in the future experiments.

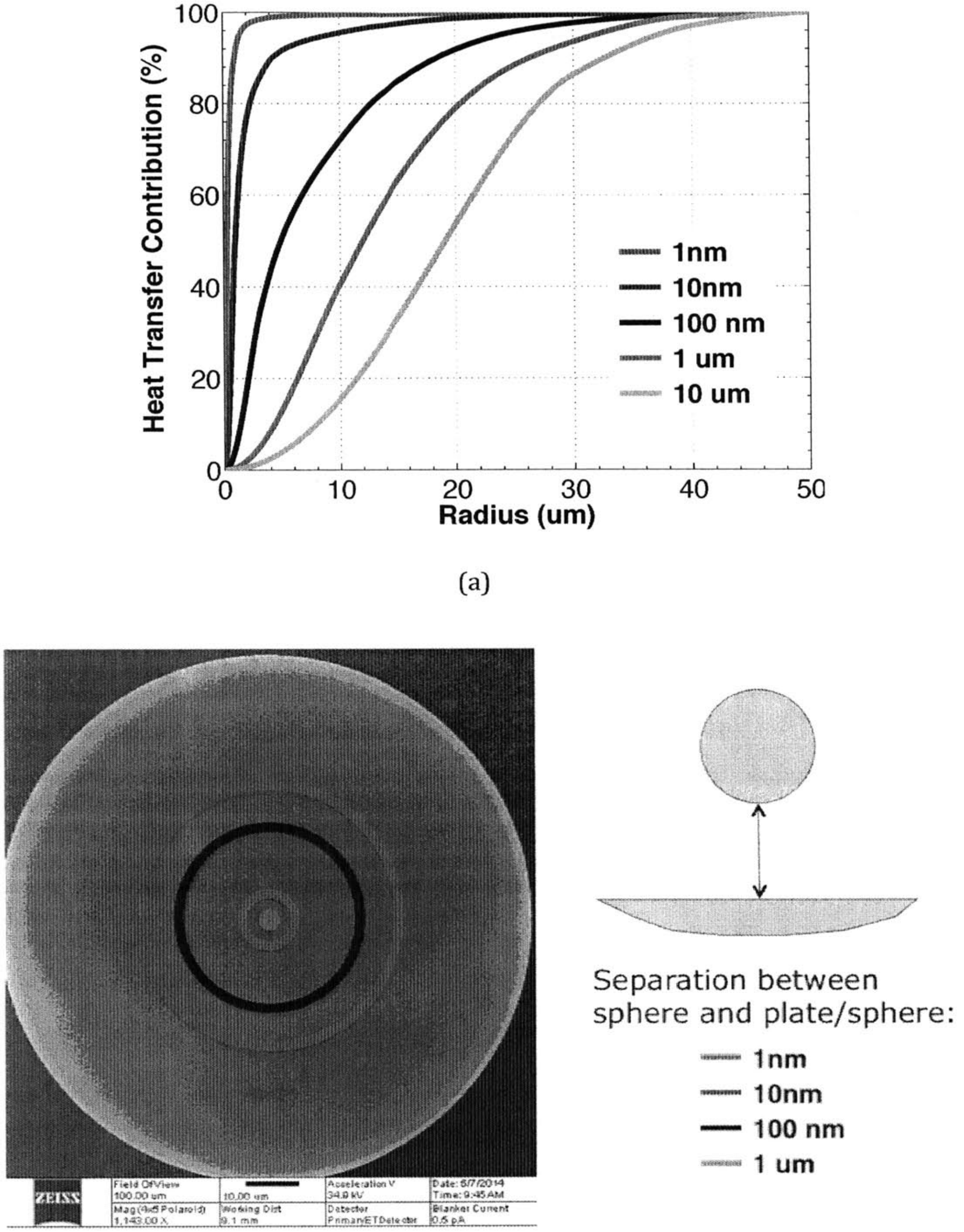

(a)

(b)

Figure 4.13 (a) The normalized accumulated heat flux as a function of the projected radius between a silica sphere with 50 um radius and a silica substrate for different separation distances. (b) Each circle shows an area, which contribute to the 90% of the near-field radiative heat flux for different separation gaps. The heat transfer is concentrated in a smaller area as the separation distance becomes smaller.

4.2 Measurement of near-field thermal radiation between two silica spheres

The geometries of the closely spaced objects, dictated by the device and its application, affect the near-field thermal radiation. Theoretical studies on the effects of different geometries beyond two parallel plates have been investigated, although with little intensity, due to the complexity of the numerical calculation. These geometries include a sphere and a semi-infinite body [37], [38], two spheres [39], and more complicated geometries [40]–[44].

To date, the challenges of alignment of two heat exchanging bodies has limited the existing experimental investigation to plate-plate[57]–[61], sphere-plate[2], [3], [62]–[66], and tip-plate measurement [67]–[69]. However, to enable real applications, the design of the devices should not be limited to these three configurations.

The effects of the curvature on near-field thermal radiation have been investigated theoretically. Narayanaswamy and Chen [39] were the first to analyze near-field thermal radiation between two spheres. Numerical calculation was performed to solve this problem. This work is marked as the first attempt to analyze near-field thermal radiation beyond dipole approximation [45] or proximity approximation. It is found that the near-field thermal radiation between a sphere and a semi-infinite plate and two spheres can be approximated with the proximity approximation (PA) [37], [46]. This work experimentally demonstrates near-field thermal radiation between two spheres. This work extends the existing sphere-plate experiment and demonstrates the effect of the curvature on near-field thermal radiation by comparing near-field thermal radiation between two spheres and that between a sphere and a plate.

4.2.1 Sample preparation

The measurement is done using the bimaterial cantilever based near-field thermal radiation measurement setup. Detailed descriptions on the complete experimental setup and measurement technique are explained in chapter 3.

In this measurement, two silica microspheres need to be prepared and aligned. The first sphere is glued to the edge of a microscope glass slide. The process is as follow. We first prepare a clean microscope glass slide. A thin layer of glue with the size of 100 x 100 μm^2 is applied on the edge of the glass slide using a small tip (One can use a cantilever tip or a tungsten tip). Clusters of microsphere are prepared on another clean glass slide. These spheres are then poured on the area where the glue is prepared. By chance, there will be a sphere, which will fall on the glue (Figure 4.14a). The second sphere is glued to a bimaterial cantilever. The radius of the first sphere is 49.4 ± 0.4 μm and the radius of the second sphere is 49.2 ± 0.4 μm.

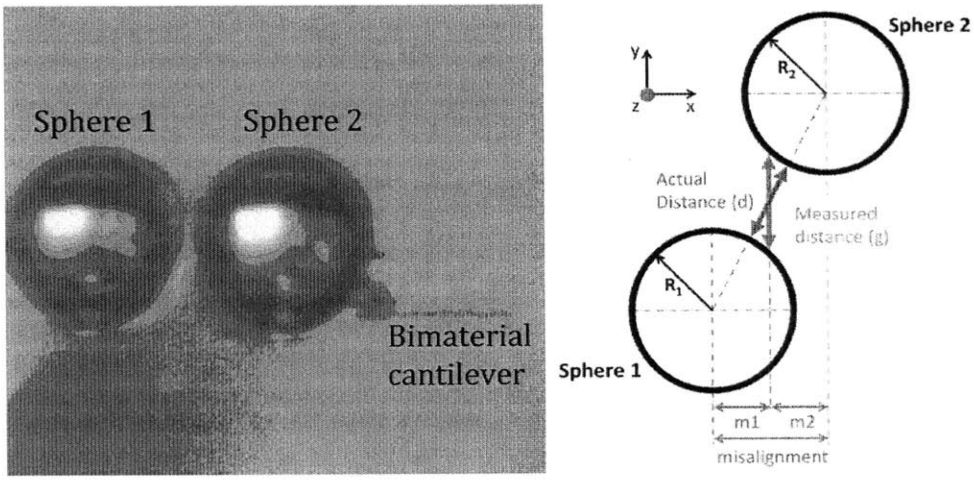

(a) (b)

Figure 4.14 (a) Two spheres are aligned optically in x and z axis. The misalignment of 5 μm between two spheres is estimated due to the resolution of the microscopic image of the spheres. The radius of the first sphere is 49.4 ± 0.4 μm and the radius of the second sphere is 49.2 ± 0.4 μm. Using Eq. 1, the difference between the measured distance and the actual distance is found to be smaller than 0.4 %. (b) Due to the misalignment between the two spheres, the distance measured (g) is not the actual distance (g).

The two spheres are aligned using an optical microscope. The schematic of the two spheres is presented in figure 4.14b. The sphere number 1 is moved relative to the sphere number 2 in the y direction. The distance between two spheres is determined by measuring the distance traveled by the sphere number 1 until it makes contact with the sphere number 2. If both spheres are perfectly aligned, the measured distance is the normal distance, i.e. the actual distance. But, due to the misalignment, the distance measured is not the actual distance. The relation between the measured, the actual, and the misalignment distance can be expressed as

$$d = \sqrt{\left[g + \sqrt{R_1^2 - m_1^2} + \sqrt{R_2^2 - m_2^2}\right]^2 + [m_1 + m_2]^2} - [R_1 + R_2] \qquad (4.2)$$

As shown in figure 4.14b, d is the actual distance, g is the measured distance, R_1 and R_2 are the radii of the spheres, m_1 and m_2 are the misalignment distances. The misalignment of 5 μm between two spheres is estimated due to the resolution of the optical microscope. Using Eq. (4.2), the difference between the measured distance and the actual distance is found to be smaller than 0.4 %.

4.2.2 Results and discussion

Figure 4.16 presents the near-field thermal radiative conductance as a function of normal distance of two measurements. The radius of the silica microspheres used for the first measurement are 49.4 and 49.2 μm. The radius of the silica microspheres used for the second measurement are 45.1 and 46.4 μm. The measurement data of the near-field conductance between two silica spheres is plotted as red squares and green triangles. The error bar represents 95% confidence interval. The theoretical predictions of the near-field thermal radiative conductance between two silica spheres are plotted as a red and green line for comparison. The measurement data of the near field conductance between a silica sphere and a glass slide is also plotted as blue circles and squares for comparison. The proximity approximation (PA) of the near field conductance between a silica sphere and a semi-infinite silica substrate are plotted as black and blue lines.

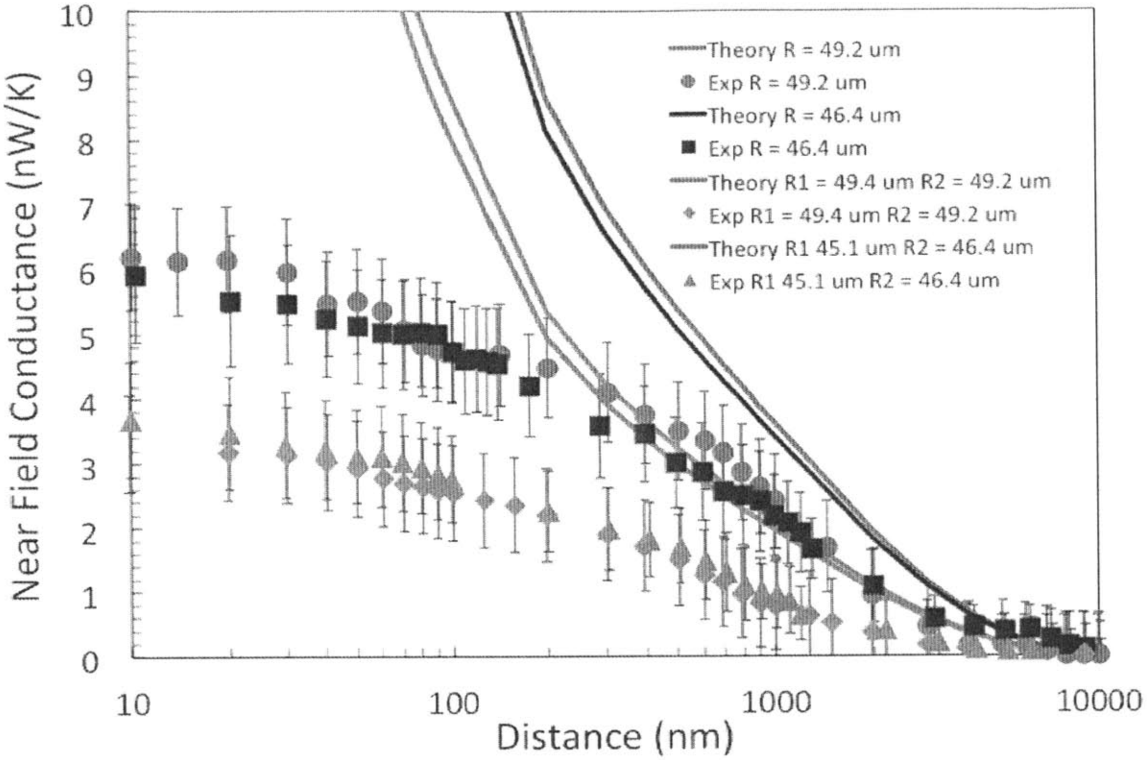

Figure 4.16 The measurement results of the near-field thermal radiative conductance between two silica spheres are plotted as a function of normal distance. The measurement results of the near-field thermal radiative conductance between a silica sphere and a glass substrate are also plotted for comparison. The error bar represents 95% confidence interval. The measurement data deviate from the theoretical calculation based on proximity due to the existence of particulates (Figure 4.4).

The measurement results between a silica sphere and a glass substrate is performed between the sphere and the glass substrate where the other sphere is attached. The near-field conductance between a sphere and a glass substrate are higher than that between two spheres since the surfaces between a sphere and a plate are separated by smaller distances than the surfaces between two spheres due to the curvature of the second sphere. These results clearly show the effect of the curvature on the near-field thermal radiation.

4.3 Summary

The first part of this chapter presents the measurement results of near-field thermal radiation between a silica sphere and a glass substrate. Our experimental data is less than what theory predict and we suspect that particulates on the sphere are responsible for the observation.

The second part of this chapter demonstrates the effects of the curvature of the surface on near-field thermal radiation by measuring near-field thermal radiation between two silica microspheres. We experimentally showed that the curvature of the surface influences the near-field thermal radiation by changing the distances between two surfaces. This results demonstrate the theoretical prediction by Narayanaswamy and Chen [39], [46]. Furthermore, our experimental method to measure near-field thermal radiation between two spheres also extends the existing experimental capabilities, which was limited to plate-plate, sphere-plate and tip-plate. This method can be further used to investigate the effect of different curvatures of the surface, such as two spheres with different radii, and sphere-cylinder as well as for studying the contribution of other types of morphology-dependent optical modes (e.g., whispering gallery modes) to the near-field radiative heat transfer.

Chapter 5

Measurement of near-field thermal radiation of doped silicon surfaces

Recent progress on nanoscale radiative transfer has also generated strong interest in the role of surface plasmon polaritons on near-field thermal radiation. However, surface plamon polaritons on metallic surfaces can only be excited at extremely high temperature since plasma frequency of metals typically lies in the UV-visible spectrum.[64] On the contrary, plasma frequency of semiconductors lies in the infrared spectrum due to lower carrier concentrations and can be thermally excited even at room temperature. Further, since the plasma frequency can be controlled by changing the carrier concentration, surface plasmon polaritons on semiconductor surface can be tuned, enabling control of near-field thermal radiation.[25], [26] Experimental investigation have also been conducted by measuring near-field thermal radiation between a silica sphere and a graphene layer,[79] and between a silica sphere and silicon substrates with different doping levels.[65]

In this work, we report the first measurement of near-field thermal radiation between doped silicon surfaces. We first explain the underlying mechanism to tune the near-field thermal radiation by changing the carrier concentration. Samples preparation procedures are then presented. Finally, the experimental results are discussed and analyzed.

5.1 Theoretical prediction

The dielectric function of doped silicon is described using Drude model [26].

$$\varepsilon(\omega) = \varepsilon_{bl} - \frac{N_e e^2/\varepsilon_0 m_e^*}{(\omega^2+i\omega/\tau_e)} - \frac{N_h e^2/\varepsilon_0 m_h^*}{(\omega^2+i\omega/\tau_h)} \qquad (5.1)$$

ε_{bl} accounts for band gap transition and lattice vibration contributions, represented by dielectric function of intrinsic silicon. The last two terms account for transition in the conduction band (free electrons) and valence band (free holes). N_e and N_h are electrons and holes carrier concentrations. m_e^* and m_h^* are the effective masses. τ_e and τ_h are the scattering times for electrons and holes respectively. The effective masses are taken as $m_e^* = 0.27m_0$ and $m_h^* = = 0.37m_0$. m_0 is the free electron mass.

All the following theoretical predictions presented in this chapter are based on the samples used in the actual measurement. The carrier concentration and mobility are measured by Hall effect system and presented in Table 5.1. The mobility is used to determine the averaged scattering time. Figures 5.1a and b show the real and imaginary parts of the dielectric constant of doped silicon with different carrier concentrations calculated using Eq. (5.1). The plasma frequency shifts to a higher frequency as the carrier concentration increases.

Surface plasmon polaritons are a coupling mode between electron waves and electromagnetic waves which propagate along the interface between two mediums [10]. Although surface plasmon polaritons are excited on doped silicon surfaces, the condition is actually not maximized since the imaginary part of dielectric constant is sufficiently high (Figure 5.1(b)) [48]; hence a dampening of the resonance. A horizontal line marks the value of −1, where the surface plasmon polariton is excited. Surface plasmon polariton resonance shifts to shorter wavelengths as carrier concentration increases.

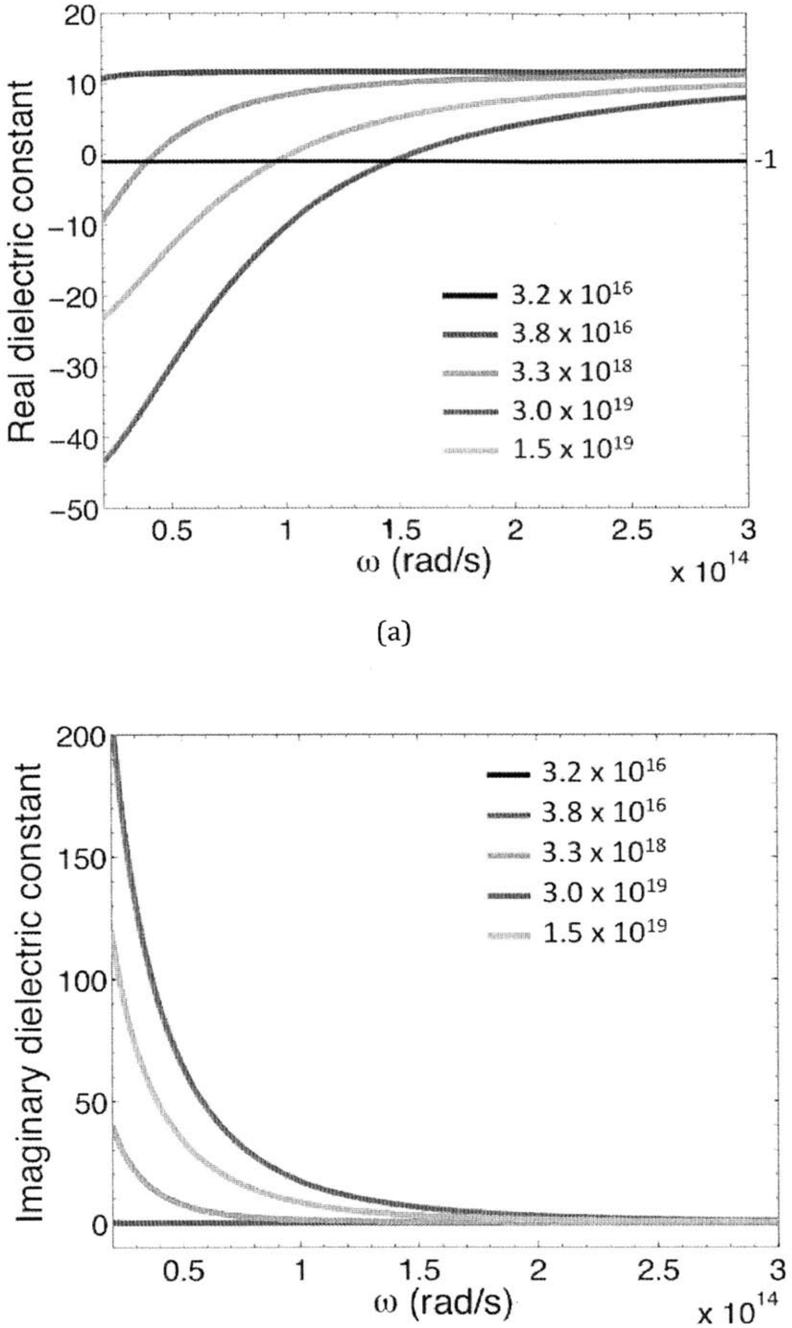

(a)

(b)

Figure 5.1 (a). Real parts of the dielectric constant for different carrier concentrations are plotted as a function of frequency. Plasma frequency shifts to the higher frequency as carrier concentration increases. A horizontal line marks the value of −1, where the surface plasmon polariton is excited. Surface plasmon polaritons resonance shifts to shorter wavelengths as the carrier concentration is increased. (b). The imaginary part of dielectric constant is not sufficiently small; hence damping the surface plasmon polaritons.

Figure 5.2 presents the local density of electromagnetic states (LDOS) of the doped silicon with different carrier concentrations at a distance of 100 nm from the surface.[131] The LDOS of SiO_2 is also plotted for comparison. The surface plasmon polaritons have a wide and short peak, since the imaginary part of dielectric constant is sufficiently high; hence a dampening of the resonance, while the surface phonon polaritons on glass surface have sharper and taller peaks.

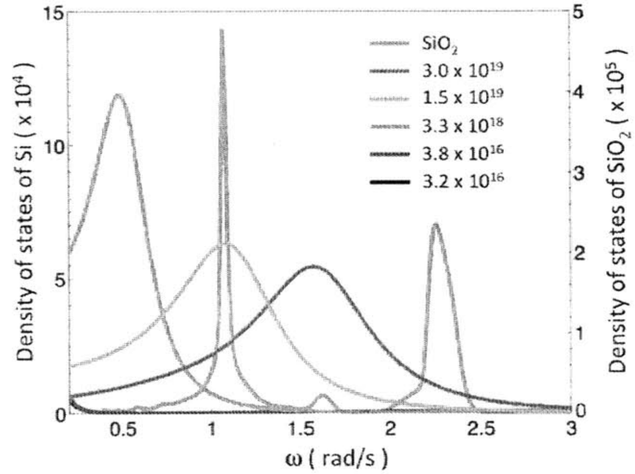

Figure 5.2 The local density of electromagnetic states of doped silicon with different carrier concentrations and glass at a distance of 100 nm from the planar surface. The surface plasmon polaritons shift to the higher frequency as the carrier concentration increases. The ability to shift the spectrum of surface plasmon polaritons offers a possibility to control near-field thermal radiation.

Figures 5.3 and 5.4 present the theoretical prediction of spectral near-field radiative heat flux for 100 nm gap and total radiative heat transfer coefficient between a semi-infinite silicon substrate with carrier concentration of 1.5×10^{19} cm^{-3} and a 500 μm thick silicon wafer with different carrier concentrations (3.2×10^{16}, 3.8×10^{16}, 3.3×10^{18}, and 3.0×10^{19} cm^{-3}). The calculation accounts for the finite thickness of the silicon wafers, which is necessary for the low carrier concentration wafers due to low absorption. Radiative transfer is maximized when the LDOS of both sides are matched as can be seen in figure 5.2. As the carrier concentration of one side decreases the overlap becomes smaller, resulting in smaller transfer. Theoretical prediction of spectral near-field radiative heat flux between a semi-infinite silicon substrate with carrier concentration of 1.5×10^{19} cm^{-3} and a SiO$_2$ substrate is also plotted in figure 5.2 for comparison. Although SiO$_2$ has sharper resonance, the broader band of surface plasmons due to higher damping leads to similar transfer rate as between two silicon surfaces.

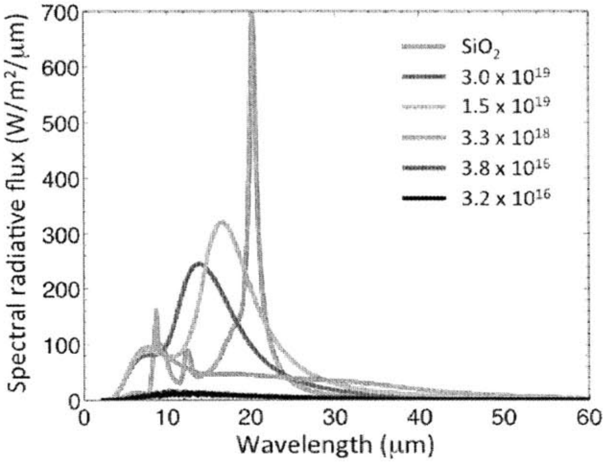

Figure 5.3 The spectral near-field radiative heat flux between a doped silicon (carrier concentration = 1.5×10^{19} cm^{-3}) surface at 320K and 500 μm thick silicon wafer with different carrier concentrations (3.2×10^{16}, 3.8×10^{16}, 3.3×10^{18} cm^{-3}, and 3.0×10^{19}) and glass at 300K separated by 100 nm gap.

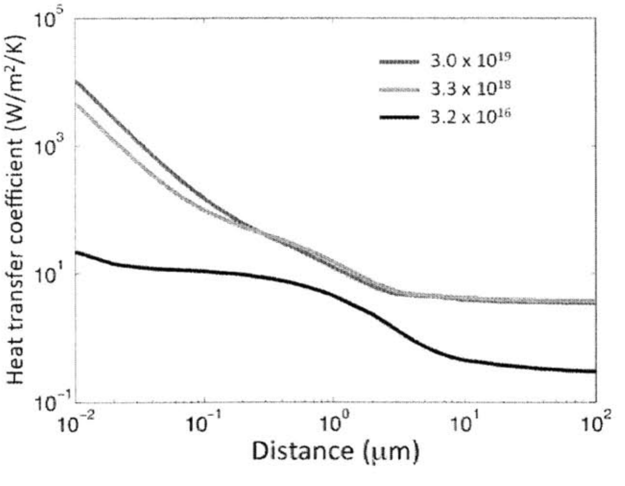

Figure 5.4 The near-field heat transfer coefficient between a doped silicon (carrier concentration = 1.5×10^{19} cm^{-3}) surface at 320K and 500 μm thick silicon wafer with different carrier concentrations (3.2×10^{16}, 3.3×10^{18} cm^{-3}, and 3.0×10^{19}) at 300K separated by 100 nm gap.

5.2 Sample preparation

The bimaterial cantilever based near-field thermal radiation measurement setup is a powerful technique. However, it is limited to measure near-field thermal radiation from a microsphere. As consequences, all of the experimental investigation using bimaterial cantilever used silica spheres as emitters, since they are available commercially. The availability of microspheres made of different materials, such as doped silicon, is crucial on near-field thermal radiation research as we explore different materials and structures experimentally.

The doped silicon microsphere used in this experiment is fabricated using an optical fiber drawing technique and a subsequent axial thermal gradient (ATG) capillary breakup process.[132] A silica-cladded silicon core fiber is continuously fed at a feed speed of 10 μm/sec through a hydrogen/oxygen flame emerging from torch tip with orifice of 0.6 mm in diameter at a distance of 6 mm from the torch outlet. The ratio of the hydrogen/oxygen flow rates forming the flame is 2.5 ± 0.1 while the hydrogen flow rate is 0.4 ± 0.1 l/min. The silicon fiber is doped with Arsenic with carrier concentrations ranging from $1.5 \pm 0.1 \times 10^{19}$ cm^{-3}.

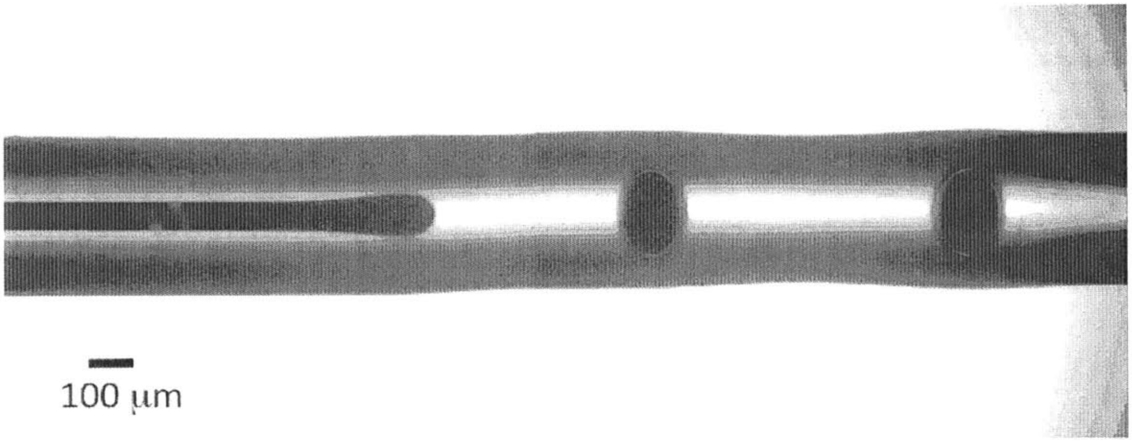

Figure 5.5 Optical micrograph of the fiber sample following the fabrication process of doped silicon spheres. The fiber is heated by the flame to the temperatures at which the silicon is molten and the silica is soft enough. The interface energy then tends to minimize itself forcing the initially cylindrical Si core to breakup into a neckless of regular spheres. (Courtesy of Alex Gumennik)

The fiber is heated by the flame to the temperatures at which the silicon is molten while the silica is soft enough such that the ratio of the core-cladding interface energy to cladding viscosity allows reshaping and pinching of the molten silicon droplets off the core in reasonable time. In the molten phase, the interface energy tends to minimize itself forcing the initially cylindrical Si core to breakup into a neckless of regular spheres, as depicted in figure 5.7. While exiting the flame, the fiber cools down, and the silica solidifies below 1600^0 C while the Si is still liquid. Further cooled Si solidifies against smooth solid silica, which prevents faceted graining of solidifying silicon. This results in a smooth surface of the silicon sphere (RMS = 30 nm). The spheres are then released from the fiber by etching the silica cladding in hydrofluoric acid. Then, the silicon sphere is attached to the cantilever, while the silicon substrates are glued to copper holders and mounted to the piezostage with 1 nm movement resolution. The measurement is done following the procedure presented in Chapter 3.

In this measurement, an As-doped silicon sphere with radius of 75 μm is used as the hot side and a 500 μm thick silicon wafer with different types of dopant and carrier concentrations are used as the cold side (Table 5.1). As-doped silicon wafer was chosen to match the dopant of the sphere, while P-doped silicon wafer was chosen due to the availability of wafers with different carrier concentrations. The carrier concentration and mobility of the silicon wafers are measured using a Hall effect system, while those of the sphere cannot be measured due to its size and are estimated to be 1.5×10^{19} cm^{-3} and 9.5 x 10 cm^2/V s.[133]

Table 5.1 Carrier concentrations and mobility of the samples are measured using Hall effect system.

Sample	Type/Dopant	Carrier concentration (cm^{-3})	Mobility (cm^2/V s)
1	n/Phosphorus	3.2×10^{16}	9.655 x 10^2 cm^2/V s
2	n/Phosphorus	3.8×10^{16}	9.46 x 10^2 cm^2/V s
3	n/Phosphorus	3.0×10^{19}	8.43 x 10 cm^2/V s
4	n/Arsenic	3.3×10^{18}	1.718 x 10^2 cm^2/V s

5.3 Results and discussions

Figure 5.6 presents the measurement results of near-field thermal radiative conductance as a function of separation distance between a doped silicon sphere and silicon wafers with different carrier concentrations. Theoretical predictions of the near-field conductance calculated with the proximity force approximation (PFA) are also presented. The PFA accounts for the finite thickness of the silicon wafers, while considers a semi-infinite body for the sphere side due to short absorption depth of the high carrier concentration (1.5×10^{19} cm^{-3}) silicon. Following the theoretical predictions, the measurement results show the tuning effect of the near-field thermal radiative conductance by the carrier concentration. The near-field conductance can be classified into the high carrier concentrations (3.0×10^{19}, and 3.3×10^{18} cm^{-3}) and low carrier concentrations (3.2×10^{16} and 3.8×10^{16} cm^{-3}). Because the sphere also has high carrier concentration (1.5×10^{19} cm^{-3}), the near-field conductance of the high carrier concentration is higher than that of low carrier concentration due to better overlap between the LDOS of both sides.

The experimental data agree reasonably well with the theoretical prediction for gaps larger than 200 nm, while deviations are clearly observed for smaller gaps, which can be caused due to several reasons. The SEM image (Figure 5.7) reveals numerous particulates with sizes around 200 nm, which is larger than the surface rougness ($\approx$30 nm). These particulates introduce an error in determining the separation distance between the sphere and the wafer. Another cause for deviation from theory comes from surface imperfection resulting from dendrites and cracks, visible on SEM image (Figure 5.7). Solidification of Si droplet is a complex process happening in few stages. It starts in undercooled droplet with protrusion of dendrites accompanied by recalescence and continues with slow gradual solidification of the residual liquid.[134] These defects are not accounted in the theoretical calculation, which assume a smooth and clean surface.

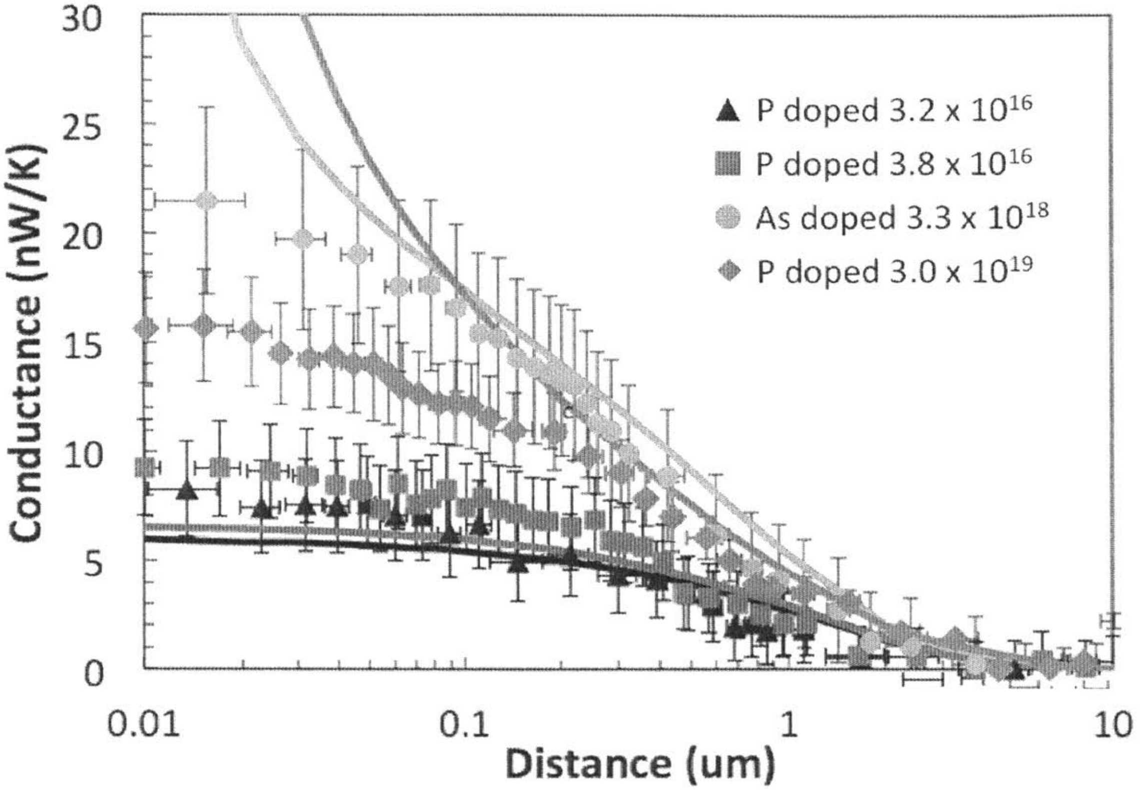

Figure 5.6 The measurement results of the near-field thermal radiative conductance between a doped silicon (carrier concentration = 1.5×10^{19} cm^{-3}) sphere (radius = 75 μm) and a silicon substrate (thickness = 500 μm) with different carrier concentrations (p-doped with different concentrations 3.2×10^{16}, 3.8×10^{16}, and 3.0×10^{19} cm^{-3} and As-doped with carrier concentration of 3.3×10^{18} cm^{-3}) are plotted as a function of distance. Clear change of the conductance is observed as the carrier concentration is varied

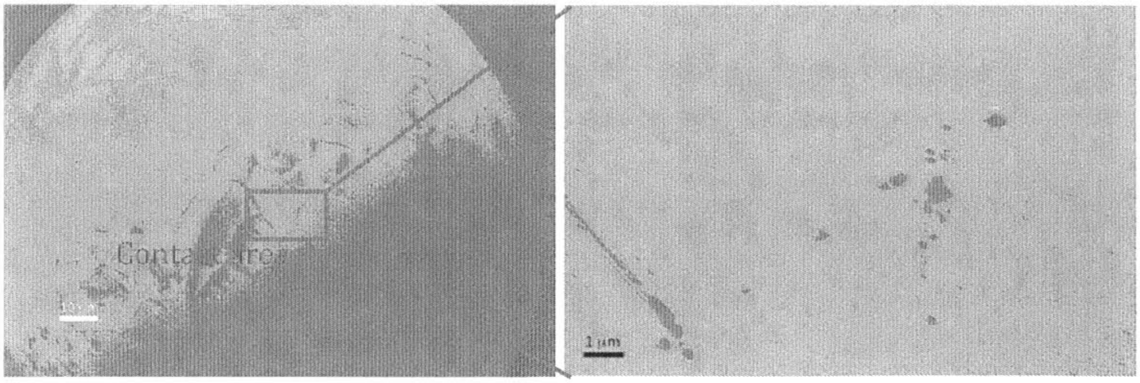

Figure 5.7 SEM image of the doped silicon sphere reveals particulates and cracks on the surface, resulting on the uncertainty on the measurement results.

The other source of uncertainty is the carrier concentration of the silicon microsphere. It is probable that the sphere has non-uniform carrier concentration. Since some of the sphere volume solidifies gradually, due to non-unity segregation constant, dopants are constantly extruded into the residual melt.[135] However, the solidification is expected to happen faster than diffusion time of dopants in liquid, such that the non-uniformity of dopant distribution is not expected to be an order of magnitude, as for quasistatic process.

5.4 Conclusion

In summary, we measure near-field thermal radiation between a doped silicon sphere with radius of 75 μm and a 500 μm thick silicon wafer with different types of dopant and carrier concentrations. The results show the tuning effect of the near-field conductance as the carrier concentration is varied. The results also show reasonable agreement with the theoretical prediction for gaps larger than 200 nm despite measurement uncertainties due to the existence of particulates, dendrites, and cracks on the surface and the carrier concentration of the sphere. This result demonstrates the potential application of doped semiconductors materials to control thermal radiation in nanoscale.

Chapter 6

Conclusion

6.1 Summary

Thermal radiation at near-field can be significant higher than blackbody radiation and this effect can be exploited for thermophovoltaic, thermal microscopy, sensing, and nanoscale thermal management applications. To demonstrate its potential applications, near-field thermal radiation has been investigated both theoretically and experimentally. Experimental investigations of near-field thermal radiation have been conducted, from proof of concept to accurate measurements, to study and characterize this phenomenon. However, to measure near-field thermal radiation is a complicated task, as explained in this thesis. Very careful measurement techniques are required in order minimize errors and thus avoid inaccurate results, both of which can lead to incorrect conclusions.

In Chapter 3, improvements to experimental systems using bimaterial cantilever for near-field thermal radiation measurement setup are presented. The low absorptance of bilayer cantilever to red-laser leads to uncertainties in absorptance measurements. To solve this problem, a blue laser is used to replace a red laser. The higher absorptance of the blue laser and a smaller laser spot result in smaller uncertainty in the measured absorptance and cantilever conductance. The measured cantilever conductance is subsequently used in red-laser based experiment that has higher sensitivity.

In Chapter 4, we repeated the measurement of near-field thermal radiation between a silica microsphere and a glass substrate based on the newly determined bilayer cantilever conductance. The measured near-field radiation conductance is lower than theoretical prediction, which is most likely due to the existence of particulates on the sphere.

We also demonstrated the effects of the curvature of the surface on near-field thermal radiation by measuring near-field thermal radiation between two silica microspheres. We experimentally showed that the curvature of the surface influences the near-field thermal radiation by changing the distances between two surfaces. Furthermore, our experimental method to measure near-field thermal radiation between two spheres also extends the existing experimental capabilities, which was limited to plate-plate, sphere-plate and tip-plate. This method can be further used to investigate the effect of different curvatures of the surface, such as two spheres with different radius, and sphere-cylinder as well as for studying the contribution of other types of morphology-dependent optical modes (e.g., whispering gallery modes) to the near-field radiative heat transfer.

In Chapter 5, we investigated near-field thermal radiation between doped silicon by measuring near-field thermal radiation between a doped silicon microsphere and silicon wafers with different types of dopant and carrier concentrations. The results show the tuning effect of the near-field conductance as the carrier concentration is varied. The results also show reasonable agreement with the theoretical prediction, despite measurement uncertainties due to the existence of particulates, cracks, and vaults on the surface, the validity of the Drude model to predict the optical constant, and the carrier concentration of the sphere.

6.2 Further improvement

The bimaterial cantilever based near-field thermal radiation measurement setup can still be further improved by following steps:

1. Although the use of a smaller-focused laser spot increases the accuracy of the absorptance measurement as explained in Section 3.3.1.3, however it also reduces sensitivity to measure heat flux. A shorter focal length lens and a larger incoming laser beam are used to make a smaller laser spot (Eq. 3.14). As a consequence, the reflected laser beam from the cantilever diverges at faster rate and has a larger size as depicted in figure 6.1. Since the position sensing detector (PSD) has a specific active area size, the PSD has to be placed closer to the cantilever to make sure the reflected laser beam occupies the active area. But since the distance between the cantilever and the detector is proportional with the sensitivity, placing the PSD closer to the cantilever reduces the sensitivity (Eq. 3.7).

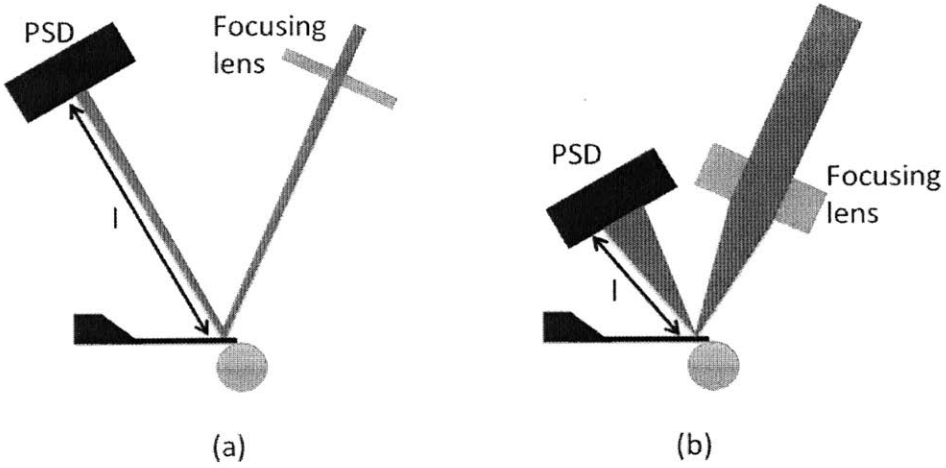

Figure 6.1 (a) A longer focal length lens and a smaller incoming laser beam result in larger laser spot on the cantilever. (b) A shorter focal length lens and a larger incoming laser beam result in smaller laser spot on the cantilever. However, this condition reduces sensitivity.

We believe there is a maximum condition where the laser spot is minimized to reduce the scattered light, while the rate of the divergence of the laser beam is slow enough to further the distance between the cantilever and the position. This of course requires iterative process by trying different lenses with different focal length on the measurement system.

2. As explained in Chapter 3, a blue laser is used due to its higher absorptance. But, it has limitation that it cannot access very low temperature difference needed for the force measurement. A red laser has low absorptance resulting in large error in the power calibration.

   A green laser (λ = 532 μm) might be the solution for this problem since it has an absorptance of 0.3. Following the example above, by utilizing green laser, the temperature difference can be as low as 1 K. This might be the optimized condition, such that the absorptance is high enough so that the absorbed power measurement is accurate, while the setup can still access very low temperature difference required to measure force.

3. Our measurement setup uses a commercial silicon nitride AFM cantilever purchased from BudgetSensors. Although the sensitivity of this cantilever is sufficient to measure near-field heat flux in the order of 100s nW, it can be further improved by replacing this cantilever with a more sensitive bimaterial cantilever. However, fabrication of bimaterial cantilevers involves complicated microfabrication process. To avoid this, a rather simpler strategy is to order customized bimaterial cantilever.

   HYDRA6R-200N probes from App nano can fabricate a customized bimaterial with the following specifications:

   1. Material: Gold/Silicon Nitride
   2. Shape: Rectangular

3. Width: 35 um
4. Length: 200 um
5. Gold thickness: 48 nm
6. Silicon nitride thickness: 400 nm

It is predicted that this customized cantilever will double the sensitivity of the current bimaterial cantilever.

4. The laser diode module used in the measurement setup is not designed to operate in vacuum condition. Problem with outgassing and heating have been noticed. As a consequence, it takes hours to stabilize the laser power and prolong the measurement time. The fluctuation of the laser power has also been noticed resulting on thermal drift, which in the end causes the spread of the measurement data. To fix this, the laser needs to be put outside of the vacuum chamber, and connected through fiber optics to measurement setup inside the vacuum chamber.

5. The cleanliness of the sample is very important as explained in chapter 4. Any particulates on the surface will result in large uncertainty on the measurement result. Particulates on the surface can probably be removed by blowing nitrogen gas to the surface of the sphere, while holding the sphere with a tweezers.

   The experimental measurement setup is located in the Rohsenow and Kendall Heat Transfer Lab, which is a general purpose lab space shared by a large number of researchers. As such, maintaining strict control over environmental conditions is challenging, and we recommend subsequent nanoscale gap measurements be conducted in a cleanroom facility. Possibilities for improved environmental control include utilizing the cleanroom fabrication facility at MIT; or building a special localized clean room in the Rohsenow and Kendall Heat Transfer Lab – such as a softwall portable cleanroom to increase environmental cleanliness of the in the measurement setup.

6.3 Further direction

Bimaterial based near-field thermal radiation measurement setup is a powerful tool to measure near-field thermal radiation. However, this setup is limited in a way that it can only measure near-field thermal radiation from a microsphere. This is a crucial disadvantage since many interesting near-field thermal radiation phenomenon have been predicted for different materials and surface structures, which is usually fabricated in planar configuration and difficult to fabricate in spherical form. That is why most of the experimental investigations involve silica spheres due to their commercial availability. In the future, more effort should be focused on the development of material and nanostructure fabrication in a spherical form. The availability of different materials and/or structures in a spherical form, such as silicon, which is used on Chapter 5, will certainly open new avenues for near-field thermal radiation investigation and applications.

Appendix A

COMSOL simulation of Bimaterial Cantilever

As explained in the section 3.2.3, the temperature of the tip is used to approximate the temperature of the sphere. COMSOL simulation is performed to estimate the error due to this approximation. Following the specification of the bimaterial cantilever, the dimensions of the cantilever are:

Length: 200 μm
Width: 30 μm
Thickness:
    Si_3N_4 = 450 nm
    Au = 65 nm

The physical properties of the materials:

Thermal conductivity:

Si_3N_4 = 3.2 W/m/K [136]

Au = 230 W/m/K [137]

Emittance:

Si_3N_4 = 0.3 [138]

Au = 0.03 [5]

Silica = 0.9 [5]

Young's modulus:

Si_3N_4 = 220 GPA [139]

Au = 55 GPA [140]

Thermal expansion coefficient:

Si_3N_4 = $0.8 \times 10^{-6}\ K^{-1}$ [141]

Au = $14.2 \times 10^{-6}\ K^{-1}$ [141]

Poisson's ratio:

Si_3N_4 = 0.28 [139]

Au = 0.42 [142]

The simulation includes the effect of thermal radiation from the cantilever and the sphere. Figure A.1 presents the simulation results showing that the temperature difference between the sphere and the surrounding is estimated to be 2 % lower than the temperature difference between the tip and the surrounding.

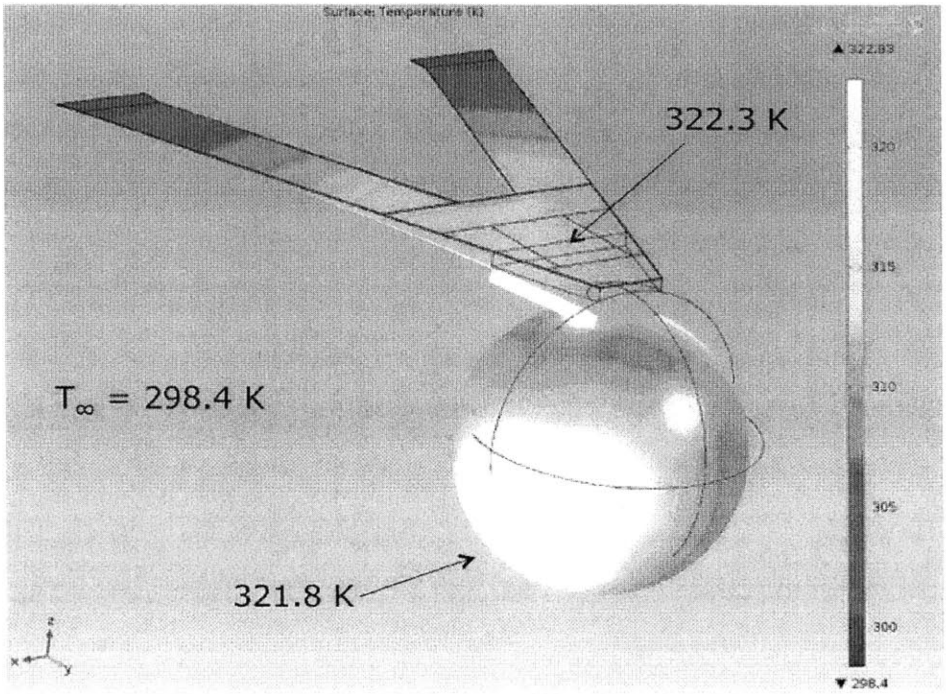

Figure A.1 The simulation results shows that the temperature difference between the sphere and the surrounding is estimated to be 2 % lower than the temperature difference between the tip and the surrounding.

Bibliography

[1] E. D. Palik, "Handbook of Optical Constants," *Proc. Natl. Acad. Sci. USA*, vol. 2, p. 1096, 1991.

[2] S. Shen, A. Narayanaswamy, and G. Chen, "Surface phonon polaritons mediated energy transfer between nanoscale gaps.," *Nano Lett.*, vol. 9, no. 8, pp. 2909–13, Aug. 2009.

[3] N. Gu, K. Sasihithlu, and A. Narayanaswamy, "Measurement of Near Field Radiation Between a Microsphere and an Infinite Plane With Improved Optical Beam," *Proceeding ASME 2012 3rd Micro/Nanoscale Heat Mass Transf. Int. Conf.*, pp. 1–7, 2012.

[4] B. Song, Y. Ganjeh, S. Sadat, D. Thompson, A. Fiorino, V. Fernández-Hurtado, J. Feist, F. J. Garcia-Vidal, J. C. Cuevas, P. Reddy, and E. Meyhofer, "Enhancement of near-field radiative heat transfer using polar dielectric thin films," *Nat. Nanotechnol.*, vol. 10, no. February, pp. 253–258, 2015.

[5] M. F. Modest, *Radiative Heat Transfer*, vol. 18. 2003.

[6] R. Siegel, J. R. Howell, and M. P. Mengüç, *Thermal radiation heat transfer*. 2011.

[7] M. Planck, "Planck1.pdf," *Verhandlungen der Dtsch. Phys. Gesellschaft*, vol. 2, pp. 202–204, 1900.

[8] M. Planck, "Planck2.pd," *Verhandlungen der Dtsch. Phys. Gesellschaft*, vol. 2, pp. 237–245, 1900.

[9] M. Planck, *The Theory of Heat Radiation*, vol. 30, no. 2. 1914.

[10] H. Raether, *Surface Plasmons on Smooth and Rough Surfaces and on Gratings*, vol. 111. 1988.

[11] E. G. Cravalho, C. L. Tien, and R. P. Caren, "Effect of Small Spacings on Radiative Transfer Between Two Dielectrics," *Journal of Heat Transfer*, vol. 89. p. 351, 1967.

[12] A. Olivei, "Transfert d'énergie thermique rayonnante entre deux diélectriques aux très basses températures," *Rev. Phys. Appl.*, vol. 3, no. 3, pp. 225–330, 1968.

[13] R. F. Boehm and C. L. Tien, "Small spacing analysis of radiative parallel metallic surfaces," pp. 405–411, 1970.

[14] D. Polder and M. Van Hove, "Theory of radiative heat transfer between closely spaced bodies," *Phys. Rev. B*, vol. 4, pp. 3303–3314, 1971.

[15] and T. V. I. Rytov S. M. , Kravtsov Y. A., *Principles of statistical radiophysics*. Springer-Verlag, Berlin Heidelberg, 1989.

[16] S. M. Rytov, *Theory of electric fluctuations and thermal radiation*. Air Force Cambrige Research Center, Bedford, MA, 1953.

[17] J. Loomis and H. Maris, "Theory of heat transfer by evanescent electromagnetic waves," *Physical Review B*, vol. 50. pp. 18517–18524, 1994.

[18] W. Eckhardt, "Macroscopic theory of electromagnetic fluctuations and stationary radiative heat transfer," *Phys. Rev. A*, vol. 29, no. 4, pp. 1991–2003, 1984.

[19] R. P. Caren, "Radiation Energy Density and Radiation Heat Flux in Small Rectangular Cavities," *J. Heat Transfer*, vol. 94, no. 3, p. 289, 1972.

[20] R. P. Caren, "Radiation Heat Transfer between Closely Spaced Metal Surfaces at Low Temperature: The Impact of Discrete Modes of the Radiation Field," *J. Heat Transfer*, vol. 94, no. 3, p. 295, 1972.

[21] R. P. Caren, "Thermal Radiation between Closely Spaced Metal Surfaces at Low Temperature due to Traveling and Quasi-stationary Components of the Radiation Field," *Int. J. Heat Mass Transf.*, vol. 3, pp. 755–765, 1974.

[22] A. V. Shchegrov, K. Joulain, R. Carminati, and J. J. Greffet, "Near-field spectral effects due to electromagnetic surface excitations," *Phys. Rev. Lett.*, vol. 85, no. 7, pp. 1548–1551, 2000.

[23] R. Carminati and J.-J. Greffet, "Near-Field Effects in Spatial Coherence of Thermal Sources," *Phys. Rev. Lett.*, vol. 82, no. 8, pp. 1660–1663, Feb. 1999.

[24] J.-J. Greffet, R. Carminati, K. Joulain, J.-P. Mulet, S. Mainguy, and Y. Chen, "Coherent emission of light by thermal sources," *Nature*, vol. 416, no. 6876, pp. 61–64, 2002.

[25] F. Marquier, K. Joulain, J. P. Mulet, R. Carminati, and J. J. Greffet, "Engineering infrared emission properties of silicon in the near field and the far field," *Opt. Commun.*, vol. 237, pp. 379–388, 2004.

[26] C. J. Fu and Z. M. Zhang, "Nanoscale radiation heat transfer for silicon at different doping levels," *Int. J. Heat Mass Transf.*, vol. 49, pp. 1703–1718, 2006.

[27] O. Ilic, M. Jablan, J. D. Joannopoulos, I. Celanovic, H. Buljan, and M. Soljačić, "Near-field thermal radiation transfer controlled by plasmons in graphene," *Phys. Rev. B*, vol. 85, no. 15, p. 155422, Apr. 2012.

[28] V. B. Svetovoy, P. J. van Zwol, and J. Chevrier, "Plasmon enhanced near-field radiative heat transfer for graphene covered dielectrics," *Phys. Rev. B*, vol. 85, no. 15, p. 155418, Apr. 2012.

[29] S. A. Biehs, M. Tschikin, and P. Ben-Abdallah, "Hyperbolic metamaterials as an analog of a blackbody in the near field," *Phys. Rev. Lett.*, vol. 109, 2012.

[30] X. Liu, R. Z. Zhang, and Z. Zhang, "Near-Perfect Photon Tunneling by Hybridizing Graphene Plasmons and Hyperbolic Modes," 2014.

[31] P. J. Van Zwol, K. Joulain, P. Ben-Abdallah, and J. Chevrier, "Phonon polaritons enhance near-field thermal transfer across the phase transition of VO 2," *Phys. Rev. B - Condens. Matter Mater. Phys.*, vol. 84, 2011.

[32] S. Basu and M. Francoeur, "Maximum near-field radiative heat transfer between thin films," *Appl. Phys. Lett.*, vol. 98, no. 24, 2011.

[33] S. A. Biehs, D. Reddig, and M. Holthaus, "Thermal radiation and near-field energy density of thin metallic films," *Eur. Phys. J. B*, vol. 55, no. 3, pp. 237–251, 2007.

[34] M. Francoeur, M. P. Mengüç, and R. Vaillon, "Near-field radiative heat transfer enhancement via surface phonon polaritons coupling in thin films," *Appl. Phys. Lett.*, vol. 93, no. 4, 2008.

[35] M. Francoeur, M. P. Mengüç, and R. Vaillon, "Local density of electromagnetic states within a nanometric gap formed between two thin films supporting surface phonon polaritons," *J. Appl. Phys.*, vol. 107, no. 3, 2010.

[36] P. Ben-Abdallah, K. Joulain, J. Drevillon, and G. Domingues, "Near-field heat transfer mediated by surface wave hybridization between two films," *J. Appl. Phys.*, vol. 106, no. 4, pp. 1–11, 2009.

[37] M. Krüger, T. Emig, and M. Kardar, "Nonequilibrium electromagnetic fluctuations: heat transfer and interactions.," *Phys. Rev. Lett.*, vol. 106, no. 21, p. 210404, May 2011.

[38] C. Otey and S. Fan, "Numerically exact calculation of electromagnetic heat transfer between a dielectric sphere and plate," *Phys. Rev. B - Condens. Matter Mater. Phys.*, vol. 84, 2011.

[39] A. Narayanaswamy and G. Chen, "Thermal near-field radiative transfer between two spheres," *Phys. Rev. B - Condens. Matter Mater. Phys.*, vol. 77, 2008.

[40] A. W. Rodriguez, O. Ilic, P. Bermel, I. Celanovic, J. D. Joannopoulos, M. Soljačić, and S. G. Johnson, "Frequency-selective near-field radiative heat transfer between photonic crystal slabs: A computational approach for arbitrary geometries and materials," *Phys. Rev. Lett.*, vol. 107, 2011.

[41] A. W. Rodriguez, M. T. H. Reid, and S. G. Johnson, "Fluctuating-surface-current formulation of radiative heat transfer for arbitrary geometries," *Phys. Rev. B*, vol. 86, no. 22, p. 220302, Dec. 2012.

[42] A. P. McCauley, M. T. H. Reid, M. Krüger, and S. G. Johnson, "Modeling near-field radiative heat transfer from sharp objects using a general three-dimensional numerical scattering technique," *Phys. Rev. B*, vol. 85, no. 16, p. 165104, Apr. 2012.

[43] A. W. Rodriguez, M. T. H. Reid, J. Varela, J. D. Joannopoulos, F. Capasso, and S. G. Johnson, "Anomalous Near-Field Heat Transfer between a Cylinder and a Perforated Surface," *Phys. Rev. Lett.*, vol. 110, no. 1, p. 014301, Jan. 2013.

[44] D. H. Hirashima, "Spectral Control of Near-Field Radiation through Surface Plasmon Polariton Interference," *Proceeding ASME 2013 Heat Transf. Summer Conf.*, pp. 1–7, 2013.

[45] J.-P. Mulet, K. Joulain, R. Carminati, and J.-J. Greffet, "Nanoscale radiative heat transfer between a small particle and a plane surface," *Appl. Phys. Lett.*, vol. 78, no. 19, p. 2931, 2001.

[46] K. Sasihithlu and A. Narayanaswamy, "Proximity Effects in Radiative Transfer," *Phys. Rev. B*, vol. 83, pp. 1–4, 2010.

[47] J. B. Pendry, "Radiative exchange of heat between nanostructures," *Journal of Physics: Condensed Matter*, vol. 11, no. 35. pp. 6621–6633, 1999.

[48] S. Basu and Z. M. Zhang, "Maximum energy transfer in near-field thermal radiation at nanometer distances," *J. Appl. Phys.*, vol. 105, no. 9, 2009.

[49] X. J. Wang, S. Basu, and Z. M. Zhang, "Parametric optimization of dielectric functions for maximizing nanoscale radiative transfer," *Journal of Physics D: Applied Physics*, vol. 42, no. 24. p. 245403, 2009.

[50] P. Ben-Abdallah and K. Joulain, "Fundamental limits for noncontact transfers between two bodies," *Phys. Rev. B - Condens. Matter Mater. Phys.*, vol. 82, no. 12, 2010.

[51] J. L. Pan, "Radiative transfer over small distances from a heated metal.," *Opt. Lett.*, vol. 25, no. 6, pp. 369–371, 2000.

[52] A. Volokitin and B. Persson, "Radiative heat transfer between nanostructures," *Physical Review B*, vol. 63, no. 20. 2001.

[53] a I. Volokitin and B. N. J. Persson, "Resonant photon tunneling enhancement of the van der Waals friction.," *Phys. Rev. Lett.*, vol. 91, no. 10, p. 106101, 2003.

[54] P.-O. Chapuis, S. Volz, C. Henkel, K. Joulain, and J.-J. Greffet, "Effects of spatial dispersion in near-field radiative heat transfer between two parallel metallic surfaces," *Physical Review B*, vol. 77. 2008.

[55] K. Joulain, "Near-field heat transfer: A radiative interpretation of thermal conduction," *J. Quant. Spectrosc. Radiat. Transf.*, vol. 109, no. 2, pp. 294–304, 2008.

[56] V. Chiloyan, J. Garg, K. Esfarjani, and G. Chen, "Phonon Heat Conduction At Sub-Nanometre Gaps," *Nat. Commun.*, vol. 6, pp. 1–7, 2015.

[57] C. . Hargreaves, "Anomalous radiative transfer between closely-spaced bodies," *Physics Letters A*, vol. 30. pp. 491–492, 1969.

[58] G. A. Domoto, R. F. Boehm, and C. L. Tien, "Experimental Investigation of Radiative Transfer Between Metallic Surfaces at Cryogenic Temperatures," *Journal of Heat Transfer*, vol. 92. p. 412, 1970.

[59] J. B. Xu, K. Läuger, R. Möller, K. Dransfeld, and I. H. Wilson, "Heat transfer between two metallic surfaces at small distances," *J. Appl. Phys.*, vol. 76, pp. 7209–7216, 1994.

[60] R. S. Ottens, V. Quetschke, S. Wise, A. A. Alemi, R. Lundock, G. Mueller, D. H. Reitze, D. B. Tanner, and B. F. Whiting, "Near-field radiative heat transfer between macroscopic planar surfaces," *Phys. Rev. Lett.*, vol. 107, 2011.

[61] T. Kralik, P. Hanzelka, M. Zobac, V. Musilova, T. Fort, and M. Horak, "Strong near-field enhancement of radiative heat transfer between metallic surfaces," *Phys. Rev. Lett.*, vol. 109, 2012.

[62] A. Narayanaswamy, S. Shen, and G. Chen, "Near-field radiative heat transfer between a sphere and a substrate," *Phys. Rev. B - Condens. Matter Mater. Phys.*, vol. 78, 2008.

[63] E. Rousseau, A. Siria, G. Jourdan, S. Volz, F. Comin, J. Chevrier, and J.-J. Greffet, "Radiative heat transfer at the nanoscale," *Nature Photonics*, vol. 3. pp. 514–517, 2009.

[64] S. Shen, A. Mavrokefalos, P. Sambegoro, and G. Chen, "Nanoscale thermal radiation between two gold surfaces," *Appl. Phys. Lett.*, vol. 100, 2012.

[65] J. Shi, P. Li, B. Liu, and S. Shen, "Tuning near field radiation by doped silicon," *Appl. Phys. Lett.*, vol. 102, no. 18, p. 183114, 2013.

[66] N. Gu, K. Sasihithlu, and A. Narayanaswamy, "Near Field Radiative Heat Transfer Measurement," *Renew. Energy Environ.*, p. JWE13, 2011.

[67] A. Kittel, W. Müller-Hirsch, J. Parisi, S. A. Biehs, D. Reddig, and M. Holthaus, "Near-field heat transfer in a scanning thermal microscope," *Phys. Rev. Lett.*, vol. 95, 2005.

[68] A. Kittel, "Nanophotonics: Probing near-field thermal radiation," *Nature Photonics*, vol. 3. pp. 492–494, 2009.

[69] L. Worbes, D. Hellmann, and A. Kittel, "Enhanced near-field heat flow of a monolayer dielectric island," *Phys. Rev. Lett.*, vol. 110, 2013.

[70] S. S. Kutateladze, N. A. Rubtsov, and Y. A. Baltsevich, "kutaladze.pdf," *Sov. Phys. Dokl.*, vol. 92, no. 3, pp. 412–416, 1978.

[71] C. M. Hargreaves, "Radiative transfer between closely spaced bodies," *Philips Res. Rep. Suppl.*, vol. 5, pp. 1–80, 1973.

[72] T. Kralik, P. Hanzelka, V. Musilova, a Srnka, and M. Zobac, "Cryogenic apparatus for study of near-field heat transfer.," *Rev. Sci. Instrum.*, vol. 82, no. 5, p. 055106, May 2011.

[73] R. St-Gelais, B. Guha, L. Zhu, S. Fan, and M. Lipson, "Demonstration of Strong Near-Field Radiative Heat Transfer between Integrated Nanostructures.," *Nano Lett.*, vol. 14, no. 12, pp. 6971–5, 2014.

[74] J. B. Xu, K. Lkger, K. Dransfeld, and I. H. Wilson, "Thermal sensors for investigation of heat transfer in scanning probe microscopy," *Rev. Sci. Instrum.*, vol. 65, no. 7, p. 2262, 1994.

[75] W. Müller-Hirsch, A. Kraft, M. T. Hirsch, J. Parisi, and A. Kittel, "Heat transfer in ultrahigh vacuum scanning thermal microscopy," *Journal of Vacuum Science & Technology A: Vacuum, Surfaces, and Films*, vol. 17, no. 4. p. 1205, 1999.

[76] B. Guha, C. Otey, C. B. Poitras, S. Fan, and M. Lipson, "Near-field radiative cooling of nanostructures.," *Nano Lett.*, vol. 12, no. 9, pp. 4546–50, Sep. 2012.

[77] S. Shen, A. Narayanaswamy, S. Goh, and G. Chen, "Thermal conductance of bimaterial microcantilevers," *Appl. Phys. Lett.*, vol. 92, no. 6, p. 063509, 2008.

[78] P. J. Van Zwol, L. Ranno, and J. Chevrier, "Tuning near field radiative heat flux through surface excitations with a metal insulator transition," *Phys. Rev. Lett.*, vol. 108, no. 23, 2012.

[79] P. J. Van Zwol, S. Thiele, C. Berger, W. A. De Heer, and J. Chevrier, "Nanoscale radiative heat flow due to surface plasmons in graphene and doped silicon," *Phys. Rev. Lett.*, vol. 109, no. 26, 2012.

[80] S. Sadat, Y. J. Chua, W. Lee, Y. Ganjeh, K. Kurabayashi, E. Meyhofer, and P. Reddy, "Room temperature picowatt-resolution calorimetry," *Appl. Phys. Lett.*, vol. 99, p. 043106, 2011.

[81] S. Sadat, E. Meyhofer, and P. Reddy, "High resolution resistive thermometry for micronanoscale measurements," *Review of Scientific Instruments*, vol. 83, no. 8. 2012.

[82] S. Sadat, E. Meyhofer, and P. Reddy, "Resistance thermometry-based picowatt-resolution heat-flow calorimeter," *Appl. Phys. Lett.*, vol. 102, no. 16, 2013.

[83] A. C. Jones and M. B. Raschke, "Thermal infrared near-field spectroscopy," *Nano Lett.*, vol. 12, no. 3, pp. 1475–1481, 2012.

[84] B. T. O'Callahan, W. E. Lewis, A. C. Jones, and M. B. Raschke, "Spectral frustration and spatial coherence in thermal near-field spectroscopy," *Phys. Rev. B - Condens. Matter Mater. Phys.*, vol. 89, no. 24, pp. 1–5, 2014.

[85] A. Babuty, K. Joulain, P. O. Chapuis, J. J. Greffet, and Y. De Wilde, "Blackbody spectrum revisited in the near field," *Phys. Rev. Lett.*, vol. 110, no. 14, 2013.

[86] Y. De Wilde, F. Formanek, R. Carminati, B. Gralak, P.-A. Lemoine, K. Joulain, J.-P. Mulet, Y. Chen, and J.-J. Greffet, "Thermal radiation scanning tunnelling microscopy.," *Nature*, vol. 444, pp. 740–743, 2006.

[87] L. M. Zhang, G. O. Andreev, Z. Fei, A. S. McLeod, G. Dominguez, M. Thiemens, A. H. Castro-Neto, D. N. Basov, and M. M. Fogler, "Near-field spectroscopy of silicon dioxide thin films," *Phys. Rev. B - Condens. Matter Mater. Phys.*, vol. 85, no. 7, 2012.

[88] M. M. Qazilbash, M. Brehm, G. O. Andreev, a. Frenzel, P. C. Ho, B. G. Chae, B. J. Kim, S. J. Yun, H. T. Kim, a. V. Balatsky, O. G. Shpyrko, M. B. Maple, F. Keilmann, and D. N. Basov, "Infrared spectroscopy and nano-imaging of the insulator-to-metal transition in vanadium dioxide," *Phys. Rev. B - Condens. Matter Mater. Phys.*, vol. 79, no. 7, pp. 1–10, 2009.

[89] R. S. DiMatteo, "Enhanced Semiconductor Carrier Generation Via Microscale Radiative Transfer; MPC - An Electric Power Finance Instrument Policy; Interrelated Innovations in Emerging Energy Technologies," Massachusetts Institute of Technology, 1996.

[90] J. E. Raynolds, "Enhanced electro-magnetic energy transfer between a hot and cold body at close spacing due to evanescent fields," in *Thermophotovoltaic Generation of Electricity: 4th NREL Conference*, 1999, pp. 49–57.

[91] M. Laroche, R. Carminati, and J.-J. Greffet, "Near-field thermophotovoltaic energy conversion," *J. Appl. Phys.*, vol. 100, no. 6, p. 063704, 2006.

[92] R. S. DiMatteo, P. Greiff, S. L. Finberg, K. a. Young-Waithe, H. K. H. Choy, M. M. Masaki, and C. G. Fonstad, "Enhanced photogeneration of carriers in a semiconductor via coupling across a nonisothermal nanoscale vacuum gap," *Appl. Phys. Lett.*, vol. 79, no. 12, p. 1894, 2001.

[93] M. D. Whale and E. G. Cravalho, "Modeling and performance of microscale thermophotovoltaic energy conversion devices," *IEEE Trans. Energy Convers.*, vol. 17, no. 1, pp. 130–142, 2002.

[94] A. Narayanaswamy and G. Chen, "Surface modes for near field thermophotovoltaics," *Appl. Phys. Lett.*, vol. 82, pp. 3544–3546, 2003.

[95] K. Park, S. Basu, W. P. King, and Z. M. Zhang, "Performance analysis of near-field thermophotovoltaic devices considering absorption distribution," *J. Quant. Spectrosc. Radiat. Transf.*, vol. 109, no. 2, pp. 305–316, 2008.

[96] M. Francoeur, R. Vaillon, and M. P. Meng, "Thermal impacts on the performance of nanoscale-gap thermophotovoltaic power generators," *IEEE Trans. Energy Convers.*, vol. 26, no. 2, pp. 686–698, 2011.

[97] R. Messina and P. Ben-Abdallah, "Graphene-based photovoltaic cells for near-field thermal energy conversion.," *Sci. Rep.*, vol. 3, p. 1383, Jan. 2013.

[98] V. B. Svetovoy and G. Palasantzas, "Graphene-on-Silicon Near-Field Thermophotovoltaic Cell," *Phys. Rev. Appl.*, vol. 2, no. 3, p. 034006, 2014.

[99] B. Zhao, L. Wang, Y. Shuai, and Z. M. Zhang, "Thermophotovoltaic emitters based on a two-dimensional grating/thin-film nanostructure," *Int. J. Heat Mass Transf.*, vol. 67, pp. 637–645, 2013.

[100] Y. Guo, S. Molesky, H. Hu, C. L. Cortes, and Z. Jacob, "Thermal excitation of plasmons for near-field thermophotovoltaics," *Appl. Phys. Lett.*, vol. 105, no. 7, p. 073903, 2014.

[101] S. A. Biehs, F. S. S. Rosa, and P. Ben-Abdallah, "Modulation of near-field heat transfer between two gratings," *Appl. Phys. Lett.*, vol. 98, no. 24, 2011.

[102] A. W. Rodriguez, M. T. H. Reid, and S. G. Johnson, "Fluctuating-surface-current formulation of radiative heat transfer: Theory and applications," *Phys. Rev. B - Condens. Matter Mater. Phys.*, vol. 88, no. 22, pp. 1–20, 2013.

[103] M. Nikbakht, "Radiative heat transfer in anisotropic many-body systems: Tuning and enhancement," *J. Appl. Phys.*, vol. 116, no. 9, p. 094307, 2014.

[104] P. J. Van Zwol, K. Joulain, P. Ben Abdallah, J. J. Greffet, and J. Chevrier, "Fast nanoscale heat-flux modulation with phase-change materials," *Phys. Rev. B - Condens. Matter Mater. Phys.*, vol. 83, no. 20, 2011.

[105] Y. Huang, S. V. Boriskina, and G. Chen, "Electrically tunable near-field radiative heat transfer via ferroelectric materials," *Appl. Phys. Lett.*, vol. 105, no. 24, p. 244102, 2014.

[106] C. R. Otey, W. T. Lau, and S. Fan, "Thermal rectification through vacuum," *Phys. Rev. Lett.*, vol. 104, no. 15, 2010.

[107] S. Basu and M. Francoeur, "Near-field radiative transfer based thermal rectification using doped silicon," *Appl. Phys. Lett.*, vol. 98, no. 11, 2011.

[108] H. Iizuka and S. Fan, "Rectification of evanescent heat transfer between dielectric-coated and uncoated silicon carbide plates," *J. Appl. Phys.*, vol. 112, no. 2, 2012.

[109] J. Huang, Q. Li, Z. Zheng, and Y. Xuan, "Thermal rectification based on thermochromic materials," *Int. J. Heat Mass Transf.*, vol. 67, pp. 575–580, 2013.

[110] L. Zhu, C. R. Otey, and S. Fan, "Ultrahigh-contrast and large-bandwidth thermal rectification in near-field electromagnetic thermal transfer between nanoparticles," *Phys. Rev. B - Condens. Matter Mater. Phys.*, vol. 88, no. 18, pp. 1–8, 2013.

[111] R. Messina, M. Antezza, and P. Ben-Abdallah, "Three-body amplification of photon heat tunneling," *Phys. Rev. Lett.*, vol. 109, no. 24, 2012.

[112] P. Ben-Abdallah and S. A. Biehs, "Near-field thermal transistor," *Phys. Rev. Lett.*, vol. 112, 2014.

[113] V. Kubytskyi, S.-A. Biehs, and P. Ben-Abdallah, "Radiative Bistability and Thermal Memory," *Phys. Rev. Lett.*, vol. 113, no. 7, p. 074301, 2014.

[114] M. Elzouka and S. Ndao, "Near-field NanoThermoMechanical memory," *Appl. Phys. Lett.*, vol. 105, no. 24, p. 243510, 2014.

[115] W. A. Challener, C. Peng, A. V. Itagi, D. Karns, W. Peng, Y. Peng, X. Yang, X. Zhu, N. J. Gokemeijer, Y.-T. Hsia, G. Ju, R. E. Rottmayer, M. A. Seigler, and E. C. Gage, "Heat-assisted magnetic recording by a near-field transducer with efficient optical energy transfer," *Nature Photonics*, vol. 3, no. 5. pp. 303–303, 2009.

[116] C. C. Williams and H. K. Wickramasinghe, "Scanning thermal profiler," *Appl. Phys. Lett.*, vol. 49, no. 23, pp. 1587–1589, 1986.

[117] A. Kittel, U. F. Wischnath, J. Welker, O. Huth, F. Rüting, and S. A. Biehs, "Near-field thermal imaging of nanostructured surfaces," *Appl. Phys. Lett.*, vol. 93, no. 19, 2008.

[118] U. F. Wischnath, J. Welker, M. Munzel, and A. Kittel, "The near-field scanning thermal microscope.," *Rev. Sci. Instrum.*, vol. 79, no. 7, p. 073708, 2008.

[119] Y. De Wilde, F. Formanek, and L. Aigouy, "Apertureless near-field scanning optical microscope based on a quartz tuning fork," *Rev. Sci. Instrum.*, vol. 74, no. 8, pp. 3889–3891, 2003.

[120] L. Tsang, J. Kong, and K. Ding, *Scattering of Electromagnetic Waves*. 2000.

[121] J. A. Kong, *Electromagnetic Wave Theory*. Cambridge, MA, USA: EMW Publishing, 2007.

[122] G. Chen, *Nanoscale Energy Transport and Conversion*. 2005.

[123] H. B. Callen and T. A. Welton, "Irreversibility and generalized noise," *Phys. Rev.*, vol. 83, no. 1, pp. 34–40, 1951.

[124] A. Narayanaswamy and G. Chen, "Direct computation of thermal emission from nanostructures," *Annu. Rev. heat Transf.*, vol. 14, pp. 169–195, 2005.

[125] L. D. Landau and E. M. Lifshitz, *Statistical Physics*, vol. 5, no. 3. 1980.

[126] J. Weber, "Fluctuation dissipation theorem," *Phys. Rev.*, vol. 101, no. 6, pp. 1620–1626, 1956.

[127] J.-P. Mulet, K. Joulain, R. Carminati, and J.-J. Greffet, "ENHANCED RADIATIVE HEAT TRANSFER AT NANOMETRIC DISTANCES," *Microscale Thermophysical Engineering*, vol. 6, no. 3. pp. 209–222, 2002.

[128] S. Timoshenko, "ANALYSIS OF BI-METAL THERMOSTATS," *J. Opt. Soc. Am*, no. l, pp. 233–255, 1925.

[129] A. Narayanaswamy and N. Gu, "Heat Transfer From Freely Suspended Bimaterial Microcantilevers," *J. Heat Transfer*, vol. 133, no. 4, p. 042401, 2011.

[130] R. J. Asaro and V. A. Lubarda, *Mechanics of Solids and Materials*. 2006.

[131] K. Joulain, R. Carminati, J.-P. Mulet, and J.-J. Greffet, "Definition and measurement of the local density of electromagnetic states close to an interface," *Int. Electron. Conf. 2004. (IQEC).*, 2004.

[132] A. Gumennik, L. Wei, G. Lestoquoy, A. M. Stolyarov, X. Jia, P. H. Rekemeyer, M. J. Smith, X. Liang, B. J.-B. Grena, S. G. Johnson, S. Gradečak, A. F. Abouraddy, J. D. Joannopoulos, and Y. Fink, "Silicon-in-silica spheres via axial thermal gradient in-fibre capillary instabilities.," *Nat. Commun.*, vol. 4, p. 2216, 2013.

[133] G. Masetti, M. Severi, and S. Solmi, "Modeling of carrier mobility against carrier concentration in arsenic-, phosphorus-, and boron-doped silicon," *IEEE Trans. Electron Devices*, vol. 30, no. 7, pp. 764–769, 1983.

[134] K. Nagashio, K. Kuribayashi, H. Okamoto, and I. Jimbo, "Fragmentation of faceted dendrite in solidification of undercooled B-doped Si melts," *Metall. Mater. Trans. A*, vol. 36, no. December, pp. 3407–3413, 2005.

[135] R. N. Hall, "Segregation of Impurities During the Growth of Germanium and Silicon," *J. Phys. Chem.*, vol. 57, no. 8, pp. 836–839, 1953.

[136] D. Song, "Phonon Heat Conduction in Nano and Micro-Porous Thin Films," University of California Los Angeles, 2003.

[137] A. J. Schmidt, R. Cheaito, and M. Chiesa, "Characterization of thin metal films via frequency-domain thermoreflectance," *J. Appl. Phys.*, vol. 107, no. 2, 2010.

[138] W. R. Knolle and D. L. Allara, "Infrared Spectroscopic Characterization of Silicon Nitride Films--Optical Dispersion Induced Frequency Shifts," *Appl. Spectrosc.*, vol. 40, no. 7, pp. 1046–1049, 1986.

[139] J. J. Vlassak and W. D. Nix, "A new bulge test technique for the determination of Young's modulus and Poisson's ratio of thin films," *J. Mater. Res.*, vol. 7, no. 12, pp. 3242–3249, 1992.

[140] H. D. Espinosa and B. C. Prorok, "Size effects on the mechanical behavior of gold," *J. Mater. Sci.*, vol. 8, no. 2, pp. 4125–4128, 2003.

[141] J. Lai, T. Perazzo, Z. Shi, and a. Majumdar, "Optimization and performance of high-resolution micro-optomechanical thermal sensors," *Sensors Actuators A Phys.*, vol. 58, no. 2, pp. 113–119, Feb. 1997.

[142] D. Kauzlarick, "Fundamentals of microfabrication, the science of miniaturization, 2nd edition [Book Review]," *IEEE Eng. Med. Biol. Mag.*, vol. 22, no. 2, 2003.